Experiments on Powder Metals

by

Michael Kim

S.B., Mechanical Engineering,
Massachusetts Institute of Technology, 1996

Submitted to the Department of Mechanical Engineering
in partial fulfillment of the requirements for the degree of

MASTER OF SCIENCE

at the

MASSACHUSETTS INSTITUTE OF TECHNOLOGY

September 1998

Author .....
Department of Mechanical Engineering
August 07, 1998

Certified by .....
Professor Lallit Anand
Professor of Mechanical Engineering
Thesis Supervisor

Accepted by .....
Professor Ain Ants Sonin
Chairman, Departmental Committee on Graduate Students

Experiments on Powder Metals

by

Michael Kim

Submitted to the Department of Mechanical Engineering
on August 07, 1998, in partial fulfillment of the
requirements for the degree of
MASTER OF SCIENCE

Abstract

This thesis describes an experimental program aimed at the development of elastic-plastic constitutive relations for cold compaction of ANCOR MH-100 iron powder. A systematic experimental program consisting of triaxial compression, torsion ring shear, uniaxial strain compression, and simple compression test systems has been conducted to investigate the room temperature deformation response of powders ranging from a relative density of $\eta = 0.4 - 0.9$. A torsion ring shear apparatus has been designed and fabricated to investigate the frictional behavior of iron powder. The torsion ring shear apparatus is also used to examine the important interface frictional behavior between the powder compact and confinement dies.

Thesis Supervisor: Professor Lallit Anand
Title: Professor of Mechanical Engineering

Acknowledgments

My greatest appreciation goes to my thesis advisor and mentor, Professor Lallit Anand, who has motivated, empowered, and enabled me to accomplish what I have achieved. Discussions with him have always been enlightening.

I also give special thanks to Professor Durali and my research partner, Chunguang Gu, for their terrific support and unerring advice.

I would also like to thank the National Science Foundation for providing funds for my graduate studies, and Dr. John T. Germaine and Gregory Da Re, who also provided much needed assistance at the commencement of this project.

Next I must acknowledge the help of my officemates: Srihari Balasubramanian, Brian Gearing, Manish Kothari, Hyung-Soo Moon, and Prakash Thamburaja who taught me the importance of keeping a sense of humor and humility. It is a pleasure to have worked with such a diverse group of intelligent individuals.

Finally, I am eternally grateful to my immigrant parents whose sacrifice, affection, and constant encouragement have given me tremendous impetus and taught me the important lesson of putting in extra effort to get more out of life.

Contents

List of Figures

List of Tables

Chapter 1

Introduction

Powder metallurgy (P/M) processing is an industrial manufacturing process in which metallic components are fabricated from powders via consolidation. Conventionally, two sequential processes are employed to manufacture a finished component to specified tolerances and exhibiting specific performance characteristics. The metallic powder is initially pre-consolidated in an appropriately shaped die or mold, from an initial relative density $\eta_0 \cong 0.5$ to a final relative density of $\eta \cong 0.9$; the relative density η is defined as $\eta = \rho/\rho_s$, where ρ is the apparent density and ρ_s is the density of the fully dense solid. The resulting green compact is then sintered at high temperature in an inert atmosphere to prevent oxidation. Modern P/M processing of components is widely used in the automotive industry. Engineers, who began with manufacturing of self-lubricating bearings, have long since graduated to the manufacture of components for structural load-bearing applications. Porous self-lubricating bearings could only be made by P/M processing. Structural parts gained acceptance because the near net-shape manufacturing by P/M processing offered cost effectiveness—a competitive, economic advantage over less convenient, classical metal-forming techniques. Powder metallurgy usage in automobiles is dominated by ferrous powder alloys. Primary usage has been in automatic transmissions, engines, steering gears, and chassis components. Figure 1-1 identifies a wide range of P/M applications in modern automobiles [1].

This thesis presents the results of a program aimed at developing a set of plas-

ticity based constitutive equations for the simulation of net-shape powder processing operations. The focus of the experimental program is on Hoeganaes ANCOR MH-100 irregular, reduced sponge iron powder. The set of experiments conducted are triaxial compression, ring shear friction, uniaxial strain compression, and simple compression tests.

Chapter 2 will review some of the published literature on the constitutive behavior and experimental observations of powdered metals at high pressures.

In Chapter 3 an array of experimental testing systems for evaluating the inelastic behavior of ANCOR MH-100 iron powder for relative densities $\eta = 0.40 - 0.90$ is presented. Results are presented and discussed. The important interface frictional behavior between the powder compact and confinement dies is also examined.

Finally, the conclusions and some suggestions for future research are summarized in Chapter 4.

Appendix A provides the calibration curves employed in the experiments. Appendix B presents the detailed procedures used for the different test systems. Appendix C provides the technical drawings for the ring shear apparatus. Appendix D explains some of the codes and conventions used in archiving the data files and Appendix E lists some of the Matlab scripts used in the data reduction.

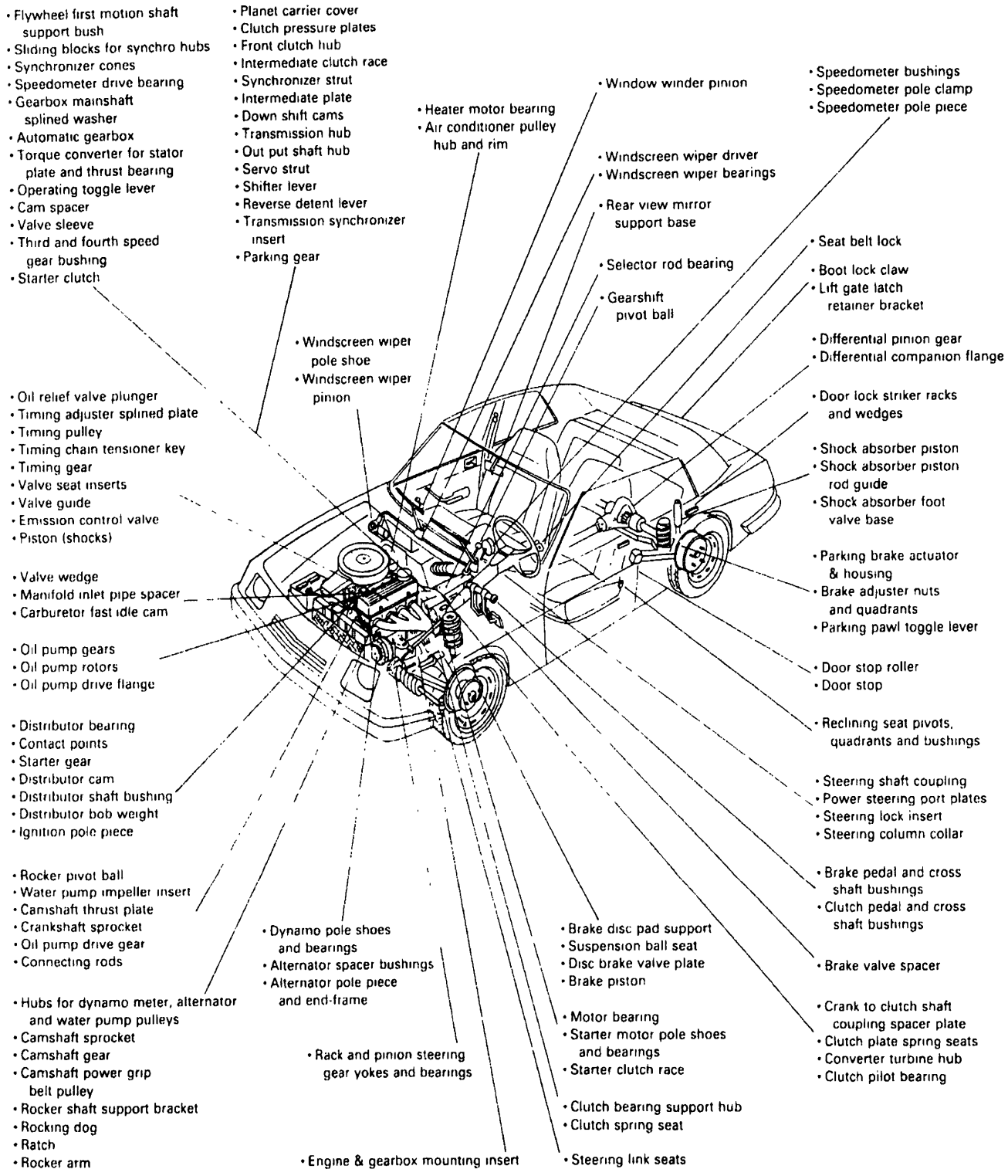

Figure 1-1: Typical P/M parts used in automobiles. After [1]

Chapter 2

Background

Many granular materials such as metal powders and ceramics conventionally require powder compaction in a suitably shaped die as part of their forming process. The resulting compacted powder is referred to as a green compact. The existence of non-uniform densification results in many problems for subsequent processing such as inhomogeneous sintering and infiltration and shape distortion during sintering. The undesirable variation of densification also reduces green strength and causes failure during ejection of components from dies.

Although a myriad of rate independent models for metal powder compaction exist virtually all are based on a very limited set of experimental data. With the exception of works by Gurson and McCabe [6], Brown and Abou-Chedid [7], and Akisanya, Cocks, and Fleck [10] , yield functions have been calibrated using data collected along one loading vector in stress space: uniaxial compression. There is generally more experimental data available for sintered powder systems, but very little experimental work has been done in evaluating the deformation response of loose powders and unsintered compacts. Most constitutive models (e.g., Kuhn and Downey [11], Shima and Oyane [13], Gurson [14], Doraivelu et al. [15], Haghi and Anand [16], and Zavaliangos and Anand [17]) for the compaction of metal powders are based on porous plasticity theory developed for sintered porous bodies, not loose powders. Constitutive models for porous metals also assume that the densification arises solely as a consequence of the plastic flow of the matrix. Other mechanisms which are present in loose powders

such as sliding and friction at inter-particle boundaries are neglected.

Constitutive models for the shearing mechanism based on the Drucker-Prager [18] and Mohr-Coulomb yield conditions exist in the soil mechanics literature. These models are insufficient to capture the deformation behavior of metal powders because the yield envelopes are unbounded for large hydrostatic pressures. Consequently, the shear yield surface is often enclosed at the open end with a "cap." (DiMaggio et al. [19]) Since metal powders could plausibly be expected to behave similar to soils during the early stages of consolidation, it seems natural to apply the multi-mechanism yield surface concepts developed for soil plasticity to metal powder aggregates. However, due to a lack of good experimental data for the plastic deformation of metal powders, it is difficult to either develop new models or validate existing models.

Previous experimental investigations (e.g., Heckel [20] [21], Kostelnick et al. [22], Hewitt et al. [23], James [24]) of consolidation of metal powders have focused primarily on determining the relationship between applied stress and relative density for consolidation in uniaxial compression. These results have provided valuable insights into the effects of powder particle and material characteristics on consolidation at axial pressures ranging from $0.1 - 1000$ MPa. Akisanya, Cocks, and Fleck probed the yield surface of copper powders using a confined triaxial test at confining pressures up to a maximum capacity of 100 MPa. The yield surface proposed by Fleck et al. [25], however, has sharp vertices where it contacts the hydrostatic stress axis, a characteristic which allows deviatoric plastic strains in a state of purely hydrostatic stresses. Brown and Abou-Chedid [7] [8] [9] performed experiments on sponge iron powder within a wide range of triaxialities. However, they did not investigate the important shear dominated response of MH-100 sponge iron powder. Gurson and McCabe performed experiments on a tungsten-nickel-iron powder blend within a limited range of triaxialities. They defined isodensity contours as yield functions and fit some elliptical forms to their data. However, few results have been reported for plastic deformation of metal powders subjected to a wider range of stress states. For example, experimental observations of yielding behavior in shear and compression of partially consolidated particulate aggregates would be invaluable for testing models

of metal powder plasticity, but few such results have been reported.

In this thesis the deformation response of ANCOR MH-100 sponge iron powder is determined by conducting experiments in triaxial compression, torsion ring shear, uniaxial strain compression, and simple compression. The following chapter describes the experimental systems, procedures, and results. Ultimately, the experimental yield data for the iron powder are presented and the practical implications of the results are discussed.

Chapter 3

Experimentally Derived Specific Constitutive Functions for MH-100 Iron Powder

An extensive experimental program was undertaken to attempt to gain insight into the deformation response of Hoeganaes[1] ANCOR MH-100 sponge iron powder. MH-100 sponge iron powder originates as magnetite iron ore which is directly reduced via hydrogen at elevated temperatures. The material is then disintegrated into powder and annealed to obtain the desired properties. As can be seen in Figure 3-1, sponge iron possesses a very irregular morphology and consequently has a very high surface area.

Sponge particles contain internal porosity and high inter-particle friction and this leads to more unfilled space and a lower apparent density than in atomized powders. The apparent density of a metal powder is the mass of a unit volume of loose powder. This fundamental property of the powder directly affects processing parameters such as the design of compaction tooling and the magnitude of press motions required to compact and densify loose powders. The most common method for determining apparent density of metal powders uses the Hall flowmeter as described in ASTM B

[1]Hoeganaes Corporation; River Road and Taylors Lane; Riverton, New Jersey 08077; Tel: 609.829.2220 http://www.hoeganaes.com

212. The flow rate of a powder is the time required for a powder sample of standard weight (50 g) to flow under atmospheric conditions through a funnel into the cavity of a container or mold. Determination of the flow rate is important in high-volume manufacturing, which depends on rapid, uniform, and consistent filling of the die cavity. Flow rate is also determined via the Hall flowmeter as described in ASTM B 213. The apparent density and flow rate for ANCOR MH-100 are listed in Table 3.1. Typical chemical analysis and the size distribution of MH-100 are listed in Table 3.2 and Table 3.3, respectively.

Physical Property	Minimum	Maximum	Typical
Apparent Density (Mg/m^3)	2.48	2.63	2.55
Flow rate (sec/50 g)	–	35	28

Table 3.1: ANCOR MH-100 Physical Properties. (Courtesy of Hoeganaes Corporation)

Fe	C	SiO_2	H_2Loss	S	P
98.2	0.02	0.15	0.45	0.01	0.01

Table 3.2: ANCOR MH-100 Chemical Analysis (wt %). After [26].

	−80	−100	−200	−325
+80	+100	+200	+325	
trace	1%	45%	32%	22%

Table 3.3: ANCOR MH-100 Sieve Analysis (% U.S. Std). After [26].

ANCOR MH-100 iron powder is industrially useful because it exhibits high green strength, and the irregular particles tend to interlock during cold compaction for low and medium density (5.4 Mg/m^3 to 6.7 Mg/m^3) ferrous P/M parts; the density for solid iron is 7.87 Mg/m^3.

The maximum index density represents the densest state of compactness of a granular material that can be attained by a standard laboratory compaction procedure that minimizes particle segregation and breakdown:

$$\rho_{dmax} = M/V \tag{3.1}$$

where M is the mass of the dry specimen in Mg and V is the volume of the specimen in m^3. The maximum index density (ASTM D 4253) of a given free-draining granular material is determined by placing the powder in a special cylindrical metal mold, applying a surcharge weight over the cross-sectional area of the mold being used equivalent to a surcharge pressure of 14 kPa, and then vertically vibrating the mold, powder, and surcharge on a vibrating table at a double amplitude of vertical vibration (peak-to-peak) of about 0.33 mm for 8 min at 60 Hz. The relative density corresponding to the maximum index density for ANCOR MH-100 iron powder is $\eta = 50\%$.

The minimum index density represents the loosest condition of a granular material that can be attained by a standard laboratory compaction procedure, which prevents bulking and minimizes particle segregation:

$$\rho_{dmin} = M/V \tag{3.2}$$

where M is the mass of the dry specimen in Mg and V is the volume of the specimen in m^3. The ASTM D 4254 procedure consists of determining the density of powder placed into a cylindrical metal mold[2] of known volume using a funnel fitted with a tube in such a manner that minimizes compaction of the powder. The relative density corresponding to the minimum index density for ANCOR MH-100 iron powder is $\eta = 30\%$. Generally, the irregularly shaped MH-100 iron powder packs randomly to about $\eta = 38\%$, however, depending on the homogeneity of the packing, distribution of both the size and shape of the powder, the drop height, and pluviation technique employed, the initial relative densities of the sponge iron powder can vary. Note that this constrasts with the random packing of spherical powders for which $\eta = 64\%$. The effect of initial density for our high pressure experiments was not rigorously investigated, because many researchers (e.g., Yamamuro and Lade [27], Pestana-Nascimento

[2]The ASTM cylindrical metal molds, surcharge, and funnel were obtained from the Geotechnical Measurements and Instrumentation Laboratory (MIT Department of Civil and Environmental Engineering, Room 1-345). The vibrating table is located in the Concrete Mixing Facility (MIT Department of Civil and Environmental Engineering, Room 1-071).

[28]) have reported that the effect of initial relative density is clearly eliminated after at high stress levels.

The initial state of our inherited, five year old MH-100 iron powder is also characterized by the presence of an oxide film. It is well known that the friction coefficient of metal is usually higher than that of the oxide of the respective metal [29]. Metal powders are frequently surface oxidized, and are reduced to obtain a clean metallic surface. Loose metal powders with an oxide film have lower inter-particle friction and therefore a higher apparent density than reduced powders with a clean metallic surface, which have higher friction and therefore lower apparent density.

3.1 Elastic Parameters

Following Anand (1982) [30], we determine the maximum and minimum bounds of the elastic parameters by presuming the ANCOR MH-100 sponge iron powder to be a composite of two constituents: (1)voids uniformly interspersed in an (2)iron matrix. Furthermore, we assume that the voids are filled by a highly compressible, low viscosity air, which is assumed to offer negligible resistance to granular rearrangement, and can be regarded as homogeneous and isotropic. Consequently, the voided granular assembly may reasonably be idealized as an isotropic, continuous medium in its overall macroscopic response.

As a matter of notation, let subscripts 1 and 2 denote the moduli for the iron matrix and voids, respectively, while the absence of a subscript refer to macroscopic moduli of the granular assembly. Denote the fractional concentrations by volume of the voids and the solid iron matrix by f and s, respectively, with $f + s = 1$.

Following Ashby and Jones [31], we assume that for solid iron the elastic moduli for the iron phase are

$$G_1 = 0.33 \times 10^4 MPa \ \ and \ \ K_1 = 0.67 \times 10^4 MPa. \tag{3.3}$$

For these values of the phase moduli, the bulk modulus K, and the shear modulus

G, of the composite can be numerically calculated for different values of the void volume fraction, f. The increase in K and G with increasing relative density, $\eta = 1 - f$ as predicted by the renowned Hashin-Shtrikman upper and lower bounds on G and K, identified by subscripts U and L, respectively, are shown in Figure 3-2 and Figure 3-3.

These bounds, which are valid as long as each phase is homogeneous and isotropic, and for any phase geometry which gives isotropic properties to the composite as a whole, are based on equations

$$G_U = G_2 + \frac{f(G_1 - G_2)(G_2 + {G_u}^*)}{(G_1 + {G_u}^*) - f(G_1 - G_2)}, \quad {G_u}^* \equiv \frac{G_2(9K_2 + 8G_2)}{6(K_2 + 2G_2)} \tag{3.4}$$

$$G_L = G_2 + \frac{f(G_1 - G_2)(G_2 + {G_l}^*)}{(G_1 + {G_l}^*) - f(G_1 - G_2)}, \quad {G_l}^* \equiv \frac{G_1(9K_1 + 8G_1)}{6(K_1 + 2G_1)} \tag{3.5}$$

$$K_U = K_2 + \frac{f(K_1 - K_2)(K_2 + {K_u}^*)}{(K_1 + {K_u}^*) - f(K_1 - K_2)}, \quad {K_u}^* \equiv \frac{4}{3}G_2 \tag{3.6}$$

$$K_L = K_2 + \frac{f(K_1 - K_2)(K_2 + {K_l}^*)}{(K_1 + {K_l}^*) - f(K_1 - K_2)}, \quad {K_l}^* \equiv \frac{4}{3}G_1 \tag{3.7}$$

whenever $K_1 > K_2$, $G_1 > G_2$.

Brown and Weber [32] experimentally determined the Young's modulus of unsintered and sintered compacts as a function of relative density via simple compression tests using strain gauges mounted on opposing sides of the specimen as the strain measurement device. The values of the curve-fitted values of Young's modulus for MH-100 sponge iron powder are taken as

$$E = E_1 \exp(E_2 \cdot \eta); \quad E_1 = 700MPa, \quad E_2 = 5.62 \tag{3.8}$$

where the Young's modulus for simplicity is assumed to depend on the current state only through the relative density η, though it might also depend on the deviatoric strain and load path. This equation also determines the total elastic response when the material is fully compacted, i.e. $\eta = 1$ and no further void collapse takes place.

Figure 3-4 shows how well the experimental data for the compacted powder before and after sintering, and curve-fitted function compare to the upper and lower Hashin-

Shtrikman bounds. The variation of the upper and lower bounds of Young's modulus E with relative density η, can be obtained by using the standard relation, $E = \frac{9KG}{(3K+G)}$ and equations (3.4), (3.5), (3.6), and (3.7).

Poisson's ratio was assumed to be constant by Brown and Weber

$$\nu \equiv constant = 0.3. \tag{3.9}$$

3.1.1 Conclusion

The upper and lower Hashin-Shtrikman predictions reasonably bound the experimental data. The curve-fitted function to the experimental data clearly show that the Young's modulus of ANCOR MH-100 iron powder increases with increasing density. As expected, this equation also determines the total elastic response when the material is fully compacted (i.e. $E = 210$ GPa at $\eta = 1$) and no further void collapse takes place.

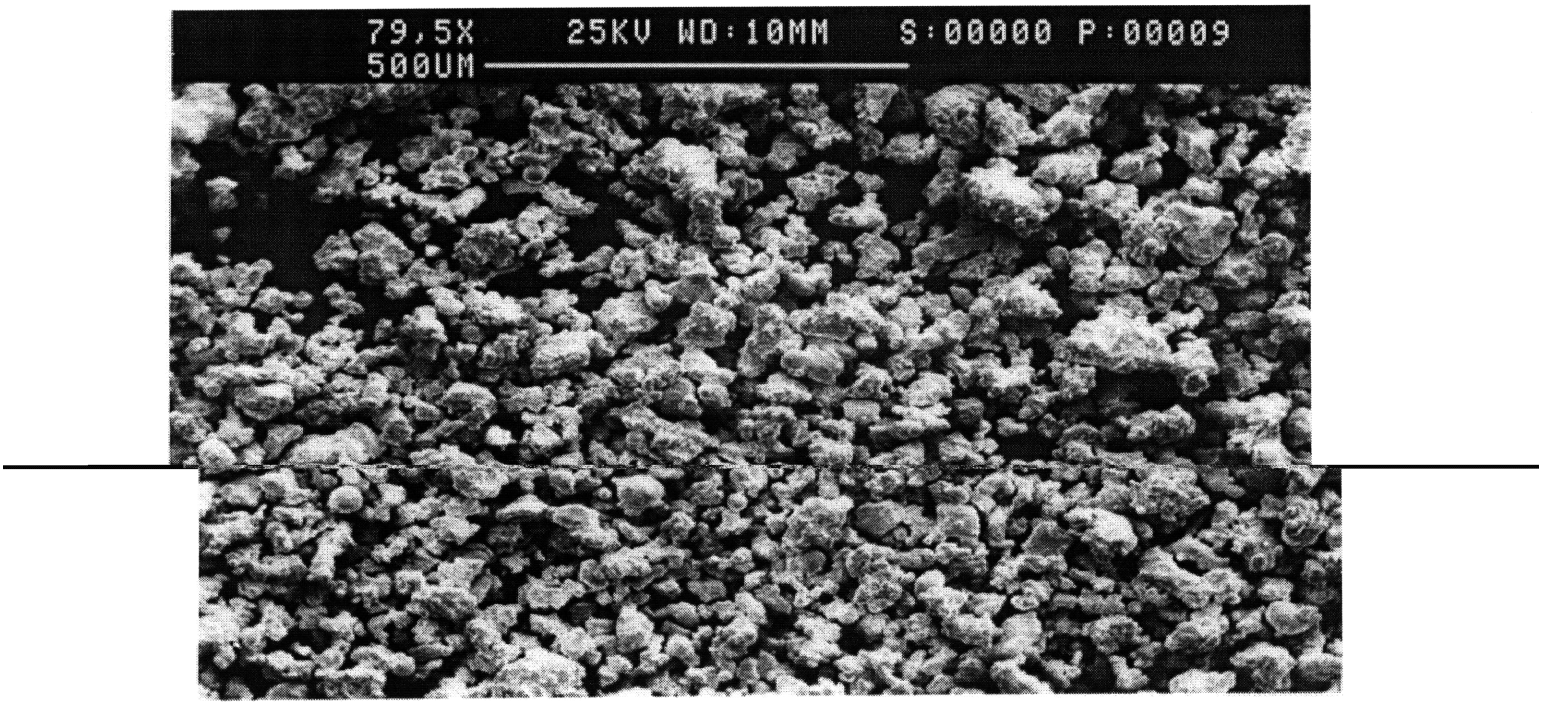

Figure 3-1: Micrograph of representative MH-100 powder particles.

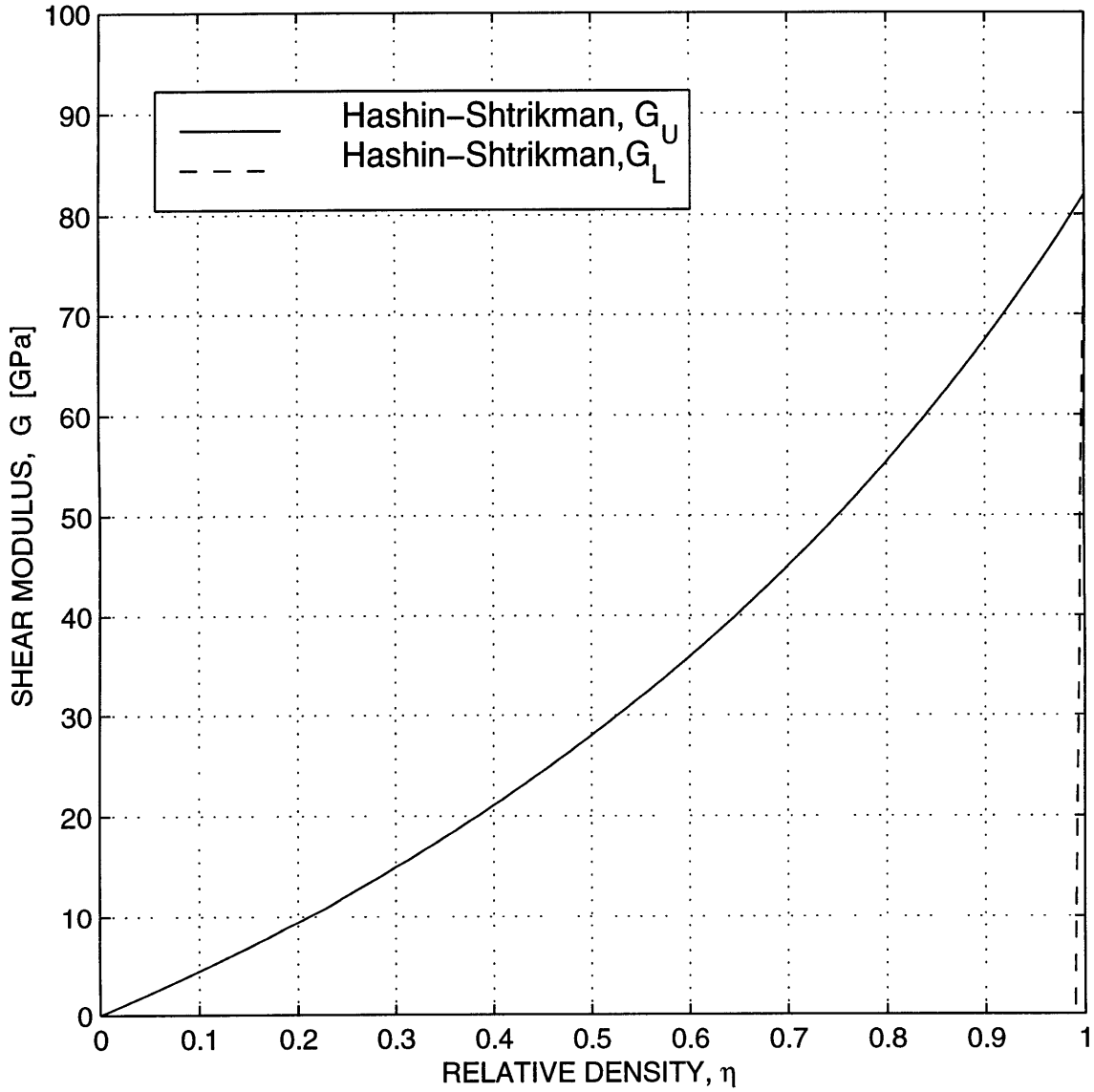

Figure 3-2: Theoretical predictions of the Hashin-Shtrikman upper bound G_U and lower bound G_L for the overall shear modulus, G of ANCOR MH-100 iron powder.

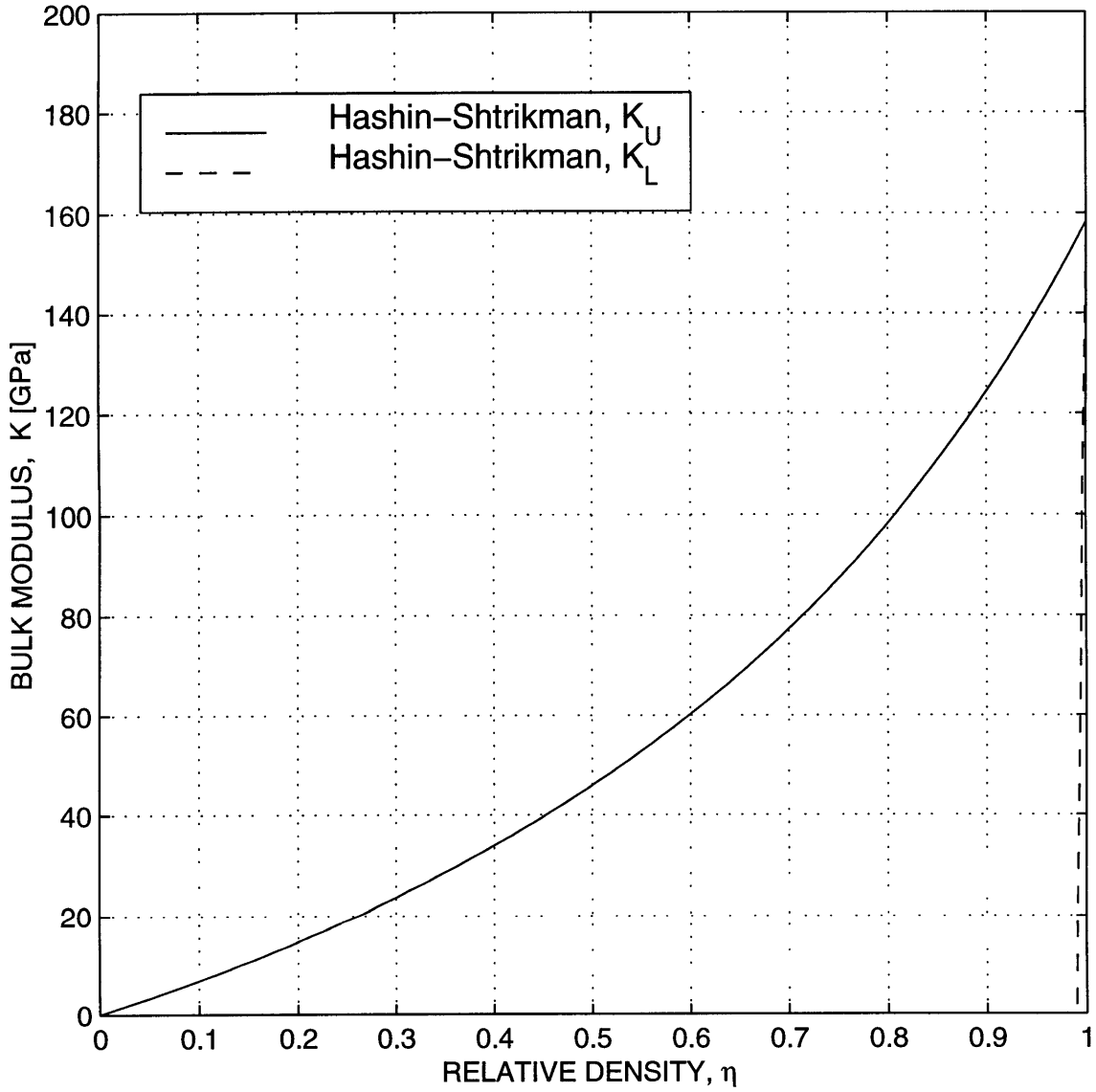

Figure 3-3: Theoretical predictions of the Hashin-Shtrikman upper bound K_U and lower bound K_L for the overall bulk modulus, K of ANCOR MH-100 iron powder.

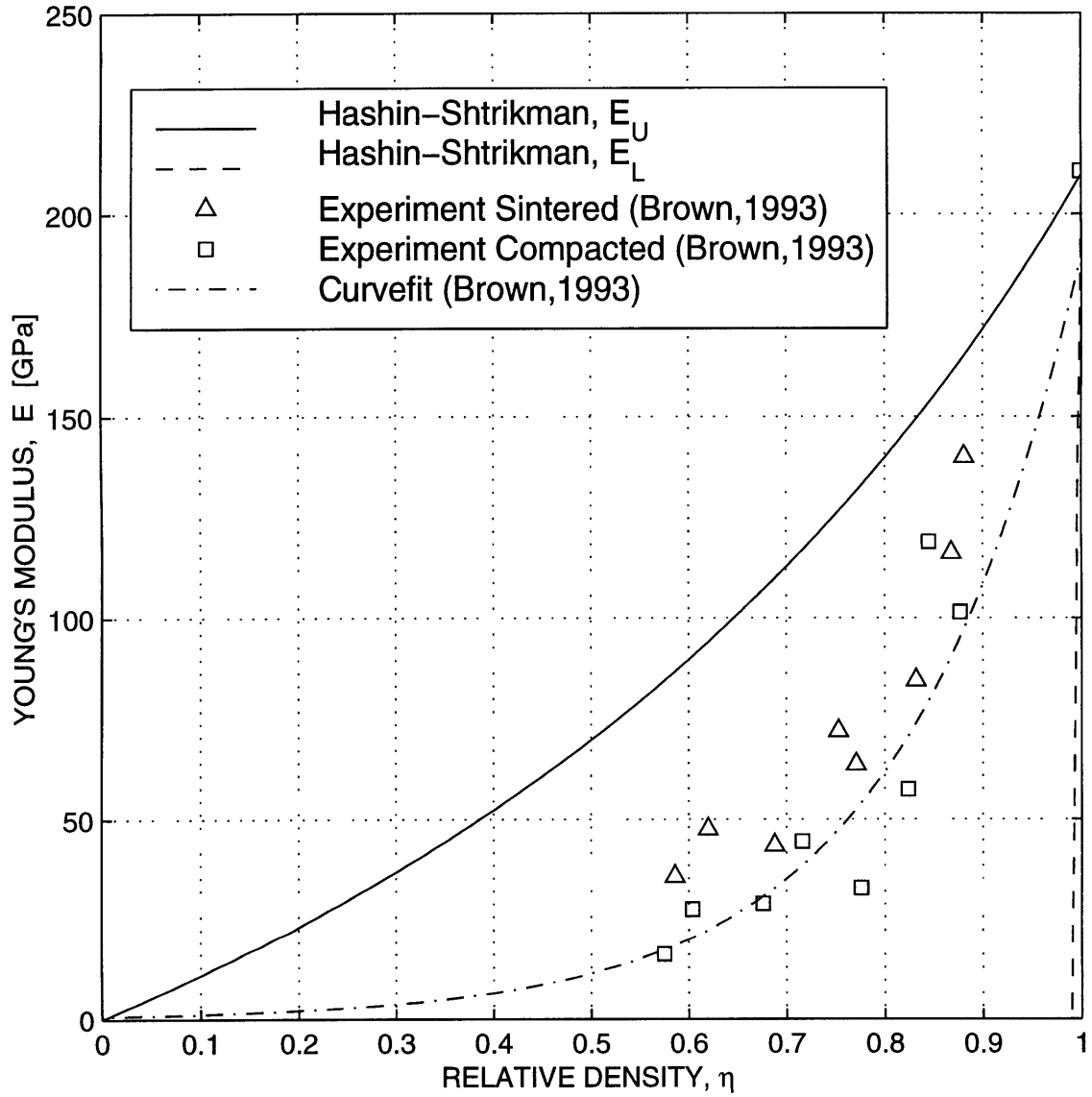

Figure 3-4: Comparison between experimental results (Brown and Weber, 1993 [32]) and theoretical predictions of the Hashin-Shtrikman upper bound E_U and lower bound E_L for the overall Young's modulus E of ANCOR MH-100 iron powder.

3.2 Triaxial Compression Tests

3.2.1 Experimental Setup

The high-pressure triaxial testing equipment used in this investigation was designed, assembled, and documented in detail by Abou Chedid [34]. The triaxial cell is based on the three-dimensional compaction apparatus developed by Shima and Mimura [35]. Figure 3-5 shows a plan view schematic of the triaxial cell displaying the components of the cell, which were manufactured from A2 tool steel (RC 61), as well as the coordinate system adopted. Iron powder is poured into the die cavity created by two angled loading blocks (Dir 2 and Dir 3), base pressure sensor block (Dir 1), pressures sensor block (Dir 2), pressure sensor block (Dir 3), and the top loading block (not depicted) used to cap the cavity. The top loading block was redesigned with a wider tab, to prevent rotation of the die cavity at higher pressures. The initial length of the edges of the cavity created by the blocks was 25-30 mm depending on the specific block configuration employed. Because of the angled surfaces, angled loading block (Dir 2) moves in the 1 and 2 directions, while angled loading block (Dir 3) moves in the 1, 2, and 3 directions. Liberal application of Teflon[3] powder spray on the angled surfaces helps to reduce the friction on these planes of motion. Pressure sensor block (Dir 1) at the bottom of the die cavity moves in the 2 and 3 directions. In order to apply axial loading on the specimen, the triaxial compaction system was set on a Baldwin hydraulic compression testing machine with a capacity of 1260 kN located in the Structures, Materials, and Rock Mechanics Laboratory[4]. When the top loading block is pushed in the 1 direction, the angled loading blocks condense the die cavity volume, and the iron powder is thus compressed from three orthogonal directions.

Since each block is free to move, it is important to prevent the powder from leaking out of potential gaps. The friction forces at the block-guide interfaces were primarily relied upon for this purpose. As another precaution, the die cavity was also coated

[3]Plastic Process Equipment, Inc. 7950 Empire Parkway. Macedonia(Cleveland), Ohio 44556. Tel: 216.468.1511

[4]MIT, Department of Civil and Environmental Engineering Room 1-034

with a thin layer of vinyl spray to prevent egress of powder. Teflon powder was applied between the powder and the vinyl coated loading block interface to minimize the presence of stress gradients associated with sidewall friction. If friction at the loading block-powder interfaces is neglected, the stress may be uniform throughout the green compact, and the normal stresses σ_1, σ_2, σ_3 are principal stresses. When the two angled blocks (Dir 2 and Dir 3) have the same angle, a stress state, commonly called a "triaxial stress state" in the field of soil mechanics, is achieved. In the present study, a more general three-dimensional stress state was produced when the two angled blocks (Dir 2 and Dir 3) had different angles. The die cavity was filled with a measured mass of powder particles (roughly 50 g). Parallelepiped specimens were formed, with initial and final dimensions depending on the particular block configuration used and the load applied.

Axial loading was applied to the specimen via a top loading block, and the axial displacement was measured using a short stroke (25.4 mm) linear potentiometer attached to the top loading block. Displacement of angled loading block (Dir 3) in the 2 direction, and displacement of pressure sensor block (Dir 2) in the 3 direction were also measured via displacement sensors. Figure 3-6 shows a sketch of a displacement sensor. The displacement sensors are linear potentiometers which were manufactured by ETI Systems.[5] A linear potentiometer interface box was also designed and instrumented to provide a voltage source, measure, and monitor the output voltage of the displacement sensors. Figures 3-7, 3-8, and 3-9 show the schematic, bridge arrangement, and wiring diagram, respectively of the linear potentiometer interface box. During a compaction process with one set of blocks, the ratio between the block displacements normal to the faces of the rectangular compact is constant and consequently, the strain ratio in the compact is almost constant. Changing the blocks and guides with various angles provided various strain ratios.

Pressure applied to each face of the rectangular compact was measured by a strain gauged pressure measuring pin. Each Wheatstone bridge arrangement, depicted in

[5]ETI Systems/Polaris Industrial Enterprises. 2251 Las Palmas Dr. Carlsbad, CA 92009. Tel: 760.929.0749

Figure 3-10, consisted of two active strain gauges installed perpendicular to the loading surface of the pressure pin, and two compensation gauges installed on a reference block of metal where no strains were expected. The pressure sensors were calibrated by performing load tests on the pressure measuring pin and calibrating the strain gauge output voltage with the corresponding pressure calculated from the Instron load cell and the cross-sectional area of the pressure measuring pin. The calibration curves for the lower and lateral pressure sensors have been included in Figures A-1, A-2, and A-3 in Appendix A.

A Keithley[6] Series 500 AMM2 analog-to-digital converter, Keithley AIM8 Strain Gage/DC Amplifier Module, strain gauge interface box, linear potentiometer interface box, and LABTECH[7] Notebook data acquisition software were used to measure and record the principal stresses and displacements at a set frequency of 20 Hz. The strain gauge interface box, used to connect the strain gauges to the Keithley Strain Gage Amplifier Module, was manufactured in-house with all components acquired from the Department of Physics Stock Room[8]. A schematic of the strain gauge interface box is depicted in Figure 3-11.

A summary of the detailed experimental procedures used in the testing are included in Appendix B.

3.2.2 Results and Discussion

The triaxial compaction test is a displacement controlled experiment. The experimental data based on the triaxial compaction system present five strain paths. Figure 3-12 shows typical stress versus strain curves for the first loading path which is near hydrostatic using the 45^o block arrangement in directions 2 and 3 ($45^o_2/45^o_3$). The remaining loading paths include some shearing. Figures 3-13 and 3-14 demonstrate the stress versus strain curves for the $70^o_2/70^o_3$ and $30^o_2/30^o_3$ block arrangements, respectively. Figures 3-15 and 3-16 show the stress versus strain curves for the asymmetric block

[6]Keithley Instruments, Inc. 28775-T Aurora Road. Cleveland, OH 44139-1891. Tel: 800.552.1115
[7]LABTECH. 400-T Research Drive. Wilmington, MA 01887. Tel: 978.657.5400
[8]MIT Department of Physics, Room 4-335

configurations $45^o_2/70^o_3$ and $45^o_2/30^o_3$, respectively.

The results from these paths cover much of the high stress triaxiality region. The stress triaxiality is the ratio of the first invariant of the stress tensor to the second invariant of the stress deviator, in short the ratio of the pressure to the shear. Certain block configurations such as the $45^o_2/70^o_3$ stress strain curve in Figure 3-15 indicate divergence at higher pressures due to rotation of the base block at higher pressures. This is a limitation of the apparatus. The presence of initial distortion in Figure 3-14 is due to the cubical imperfection in the die cavity resulting from initial misfit. The amount of deviation is also a function of the granular material tested.

3.2.3 Triaxial Compression Loading Paths

Let the mean normal stress and the effective shear stress be defined by

$$p \equiv -\frac{1}{3} tr\mathbf{T}, \tag{3.10}$$

and

$$\tau \equiv \sqrt{\frac{1}{2}\mathbf{T}' \cdot \mathbf{T}'}, \tag{3.11}$$

respectively, where

$$\mathbf{T}' = \mathbf{T} + p\mathbf{1} \tag{3.12}$$

is the stress deviator. The measured stresses for the various pressure sensors were used to calculate the mean normal stress $p = -(\sigma_1 + \sigma_2 + \sigma_3)/3$ and the effective shear stress $\tau = \frac{1}{6}[(\sigma_1 - \sigma_2)^2 + (\sigma_2 - \sigma_3)^2 + (\sigma_3 - \sigma_1)^2]^{\frac{1}{2}}$.

The main feature of the cell is its ability to load proportionally along different strain paths. Let the volumetric strain and deviatoric strain be defined by

$$\epsilon_v \equiv -tr\mathbf{D}, \tag{3.13}$$

and

$$\gamma \equiv \sqrt{2\mathbf{D}' \cdot \mathbf{D}'}, \tag{3.14}$$

respectively. A plot of theoretical triaxial compaction system strain paths is shown in Figure 3-17, in a deviatoric strain versus volumetric strain coordinate system. The paths are dependent on the inclination of the angled loading blocks. The corresponding experimentally measured stress paths are depicted in Figure 3-18. The stress paths vary from the one with pure compaction, when both angled blocks are 45^o, to those with shearing, when different angled block configurations are used.

3.2.4 Isotropic Compaction

The triaxial compression experiment is a fully confined test in which displacements of the boundaries are completely known via the three orthogonal displacement sensors and can be used to calculate the current volume at every sampled interval of time. Since the mass of the specimen is constant and can be determined at the conclusion of the test, the current volume can be used to determine the relative density. The principal stresses are measured at a sampling frequency of 20 samples per second, and the corresponding relative density can be calculated for every interval of time. Using this procedure, Figure 3-19 shows the result of plotting the resistance to hydrostatic compaction p_c versus relative density η during hydrostatic compaction via $45^o_2/45^o_3$ block arrangement. The relative density increases with increasing hydrostatic pressure; the maximum relative density attained is $\eta = 0.82$ at a pressure of 180 MPa. Because of the morphology of the powder used in this study (c.f. Figure 3-1), the initial relative density $\eta_0 = 0.44$ is lower than the random close-packed value of spherical powders $\eta_0 = 0.64$. The experimental results are compared to equation (3.15) motivated by Ashby [36], assuming a uniaxial yield stress of $s_* = 80$ MPa for pure iron powder [31] and an initial relative density of $\eta_0 = 0.44$

$$p_c = A \cdot \eta^n \frac{\eta - \eta_0}{1 - \eta_0} s_* \tag{3.15}$$

where η_0 is the initial relative density for dense random packing, η is the relative density, and s_* is the uniaxial yield strength for the solid composing the powder particles. Equation (3.15) differs from Ashby's model in two respects: (1) the leading

relative density term is raised to the power n and (2) p_c approaches $A \cdot s_*$ as $\eta \to 1$, unlike Ashby's model where the pressure approaches $3 \cdot s_*$ as $\eta \to 1$. As can be seen in Figure 3-19, the predictions of equation (3.15) compare favorably with the observed experimental pressure versus density response of ANCOR MH-100 iron powder.

3.2.5 Compaction Mechanism

Analogous to the procedure used to determine the $p_c - \eta$ relationship, the relative density corresponding to each mean normal pressure and effective shear stress can be calculated given the displacements of the boundaries and the final mass and dimensions of the specimen. Neglecting the slight scatter in the experimental data, points of identical relative density collapse onto a single curve which resemble a portion of the yield surfaces in the Cam-clay soil mechanics model developed by Schofield and Wroth [37].

$$\Phi_c = \hat{\Phi}_c(p, \tau, p_c, M) = p^2 - p \cdot p_c + \frac{\tau^2}{M^2} \leq 0. \tag{3.16}$$

The internal variables of this yield function are $\{p_c, M\}$. The internal state variable p_c is the compaction resistance to hydrostatic pressure and M is the shape parameter of the cap. In general, both of them evolve with the relative density, i.e. $p_c = \hat{p}_c(\eta)$ and $M = \hat{M}(\eta)$. For simplicity, a constant value of $M = 1.8$ was used. The triaxial compression data for ANCOR MH-100 are plotted with predictions of the Cam-clay type yield surfaces in Figure 3-20: there is good agreement between the Cam-clay model and the experimentally determined yield data. The dotted portion of the Cam-clay type yield surfaces are not expected to be operative because of the shearing mechanism.

3.2.6 Conclusion

The triaxial compression test provides a versatile method for studying stress-strain properties. A great variety of actual loading conditions can be obtained with this test. The triaxial compaction system designed, fabricated, and documented by Abou-Chedid is capable of accurately measuring both stresses and displacements for each

loading path. Sidewall friction was minimized via Teflon spray, and the orthogonal stresses measured were assumed to be principal. Three strain gauged pressure sensors were used to measure the principal stresses. Linear potentiometers were used to determine the corresponding principal strains.

The densification behavior of ANCOR MH-100 sponge iron powder was investigated using this triaxial compaction system, and the experimental data was used to obtain the empirical constants of the Cam-clay model. The effect of initial relative density was not investigated because many prior investigators have concluded that the effect of initial relative density clearly disappears at higher stresses. Stress versus strain curves were obtained for five different strain paths for pressures up to 200 MPa. The prediction of the Cam-clay model compares favorably with the actual iron powder yield behavior during the compaction mechanism for the triaxial compression data.

The evolution equation of the resistance to hydrostatic compaction p_c with relative density was experimentally established via hydrostatic triaxial compression using the $45_2^o/45_3^o$ block arrangement. The curve-fitted prediction of equation (3.15) motivated by Ashby is in excellent agreement with the experimental data, and the cap yield surface of equation (3.16) should be useful for modeling the compaction of iron powders.

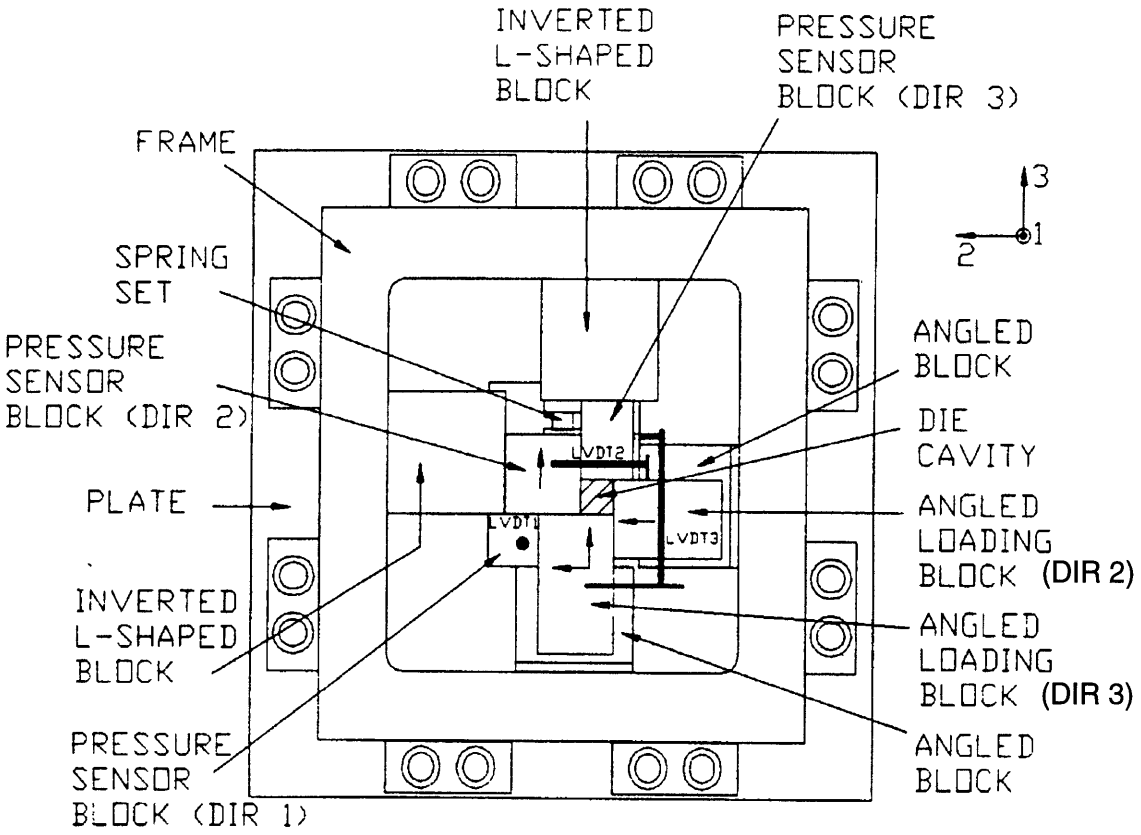

Figure 3-5: Plan schematic of triaxial compression test system assembled apparatus, strain gauged pressure sensors, and die cavity. After [34].

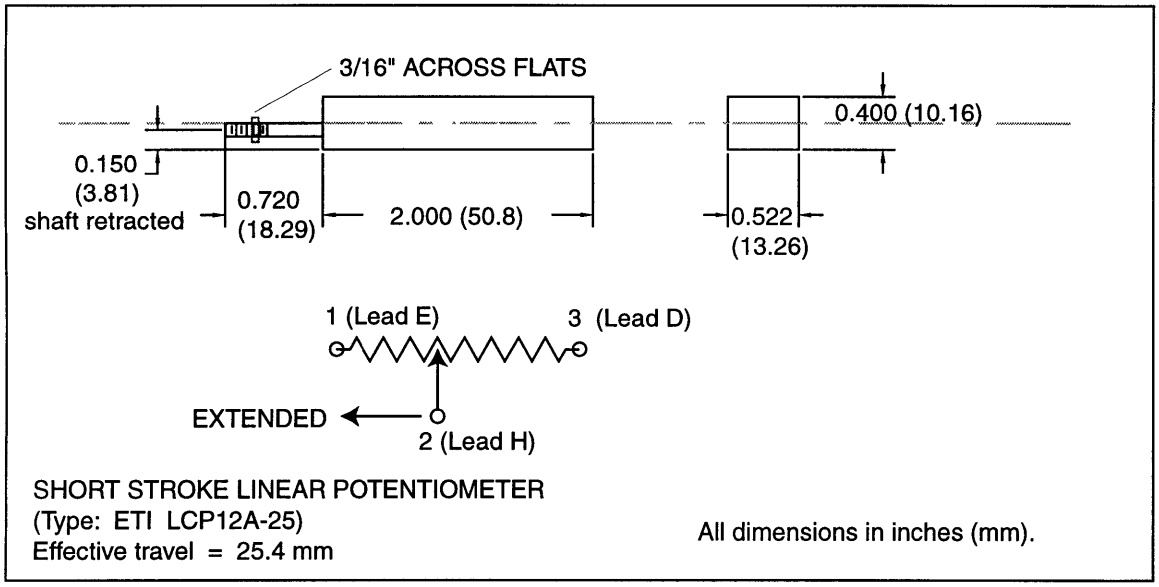

Figure 3-6: Schematic and wiring diagram of triaxial compression system displacement sensor.

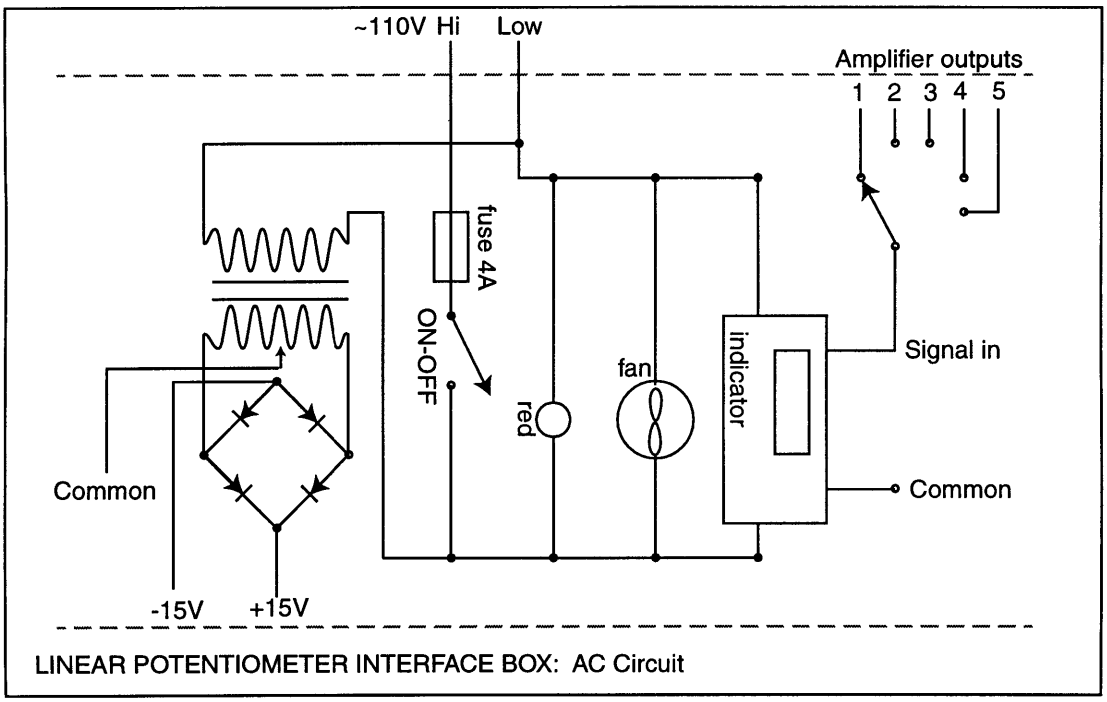

Figure 3-7: Schematic of triaxial compression system linear potentiometer interface box.

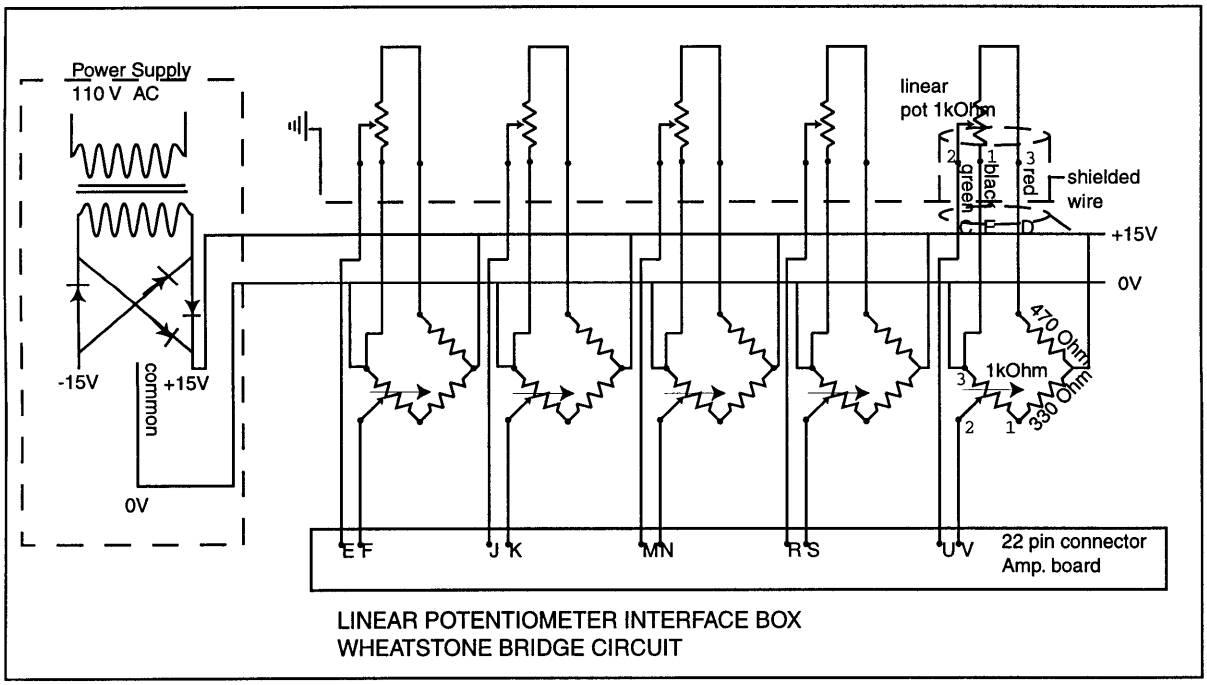

Figure 3-8: Bridge arrangement of triaxial compression system linear potentiometer interface box.

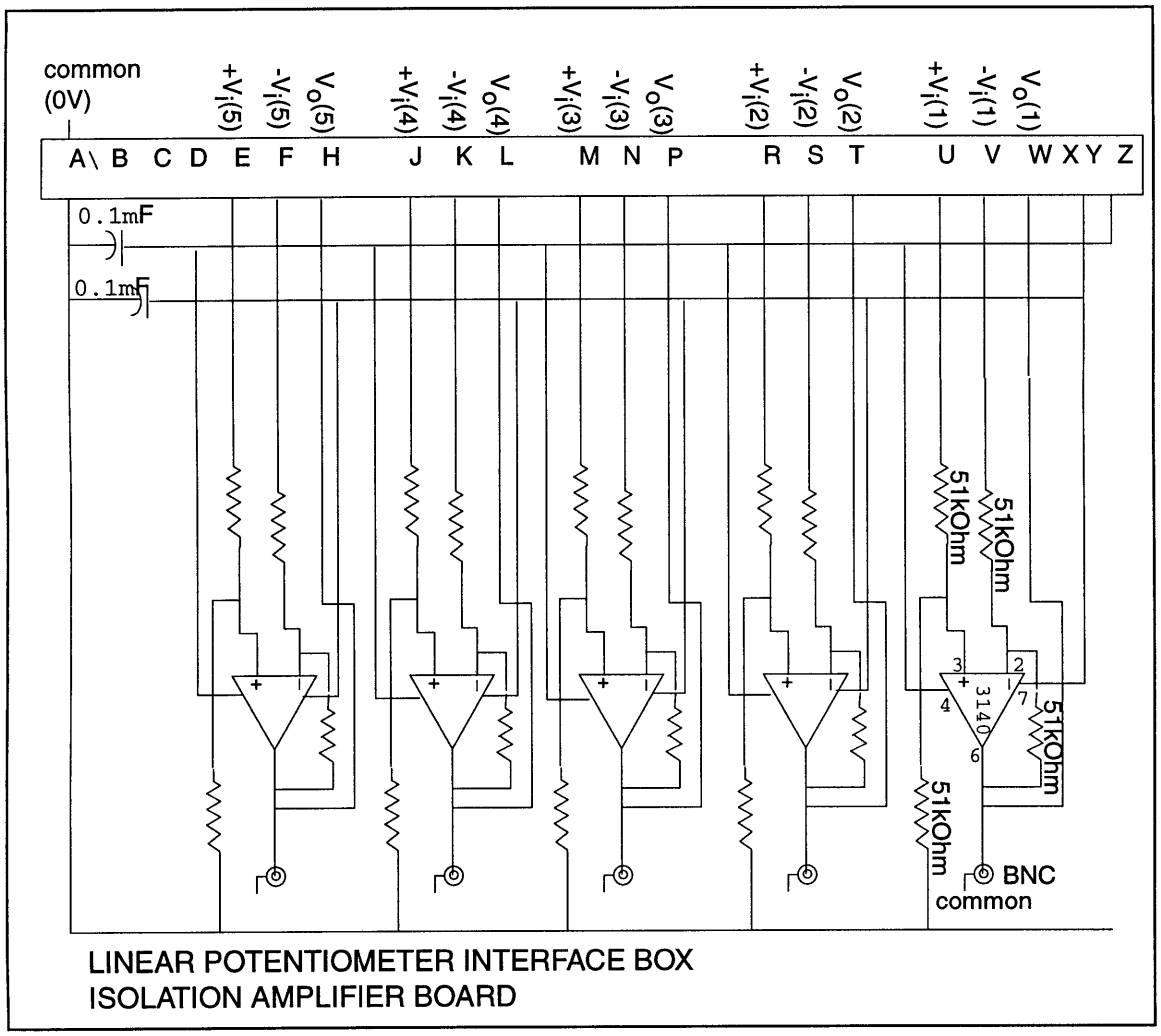

Figure 3-9: Wiring Diagram of triaxial compression system linear potentiometer interface box.

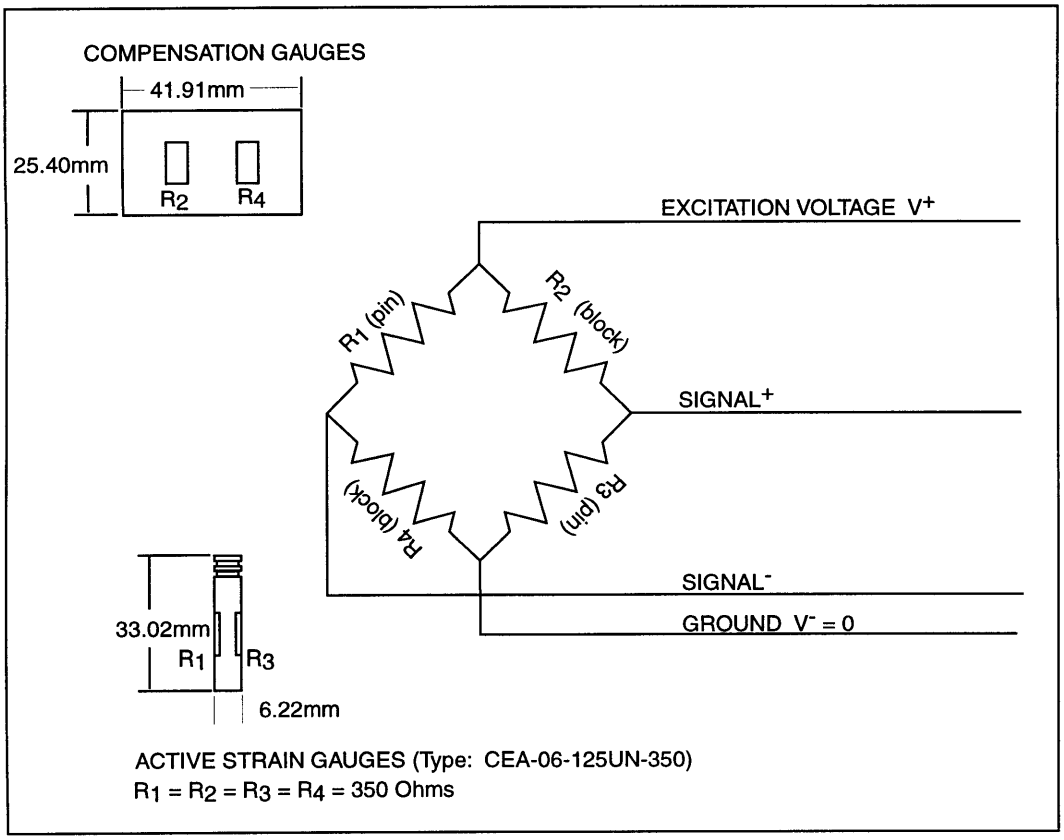

Figure 3-10: Wheatstone bridge arrangement of pressure sensors.

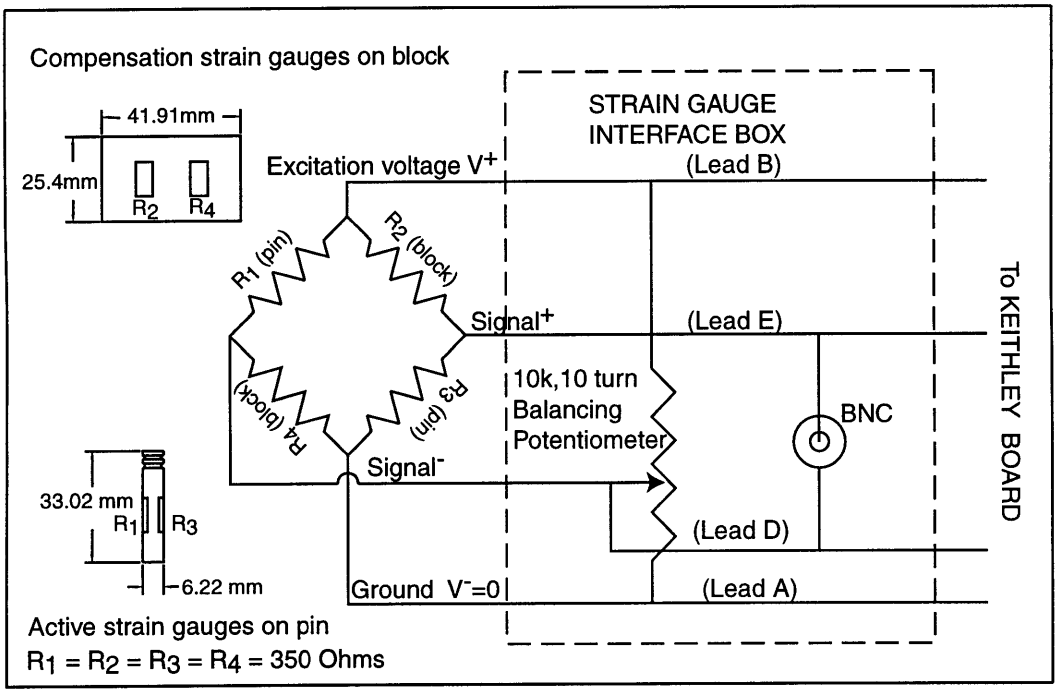

Figure 3-11: Circuit diagram of the strain gauge interface box.

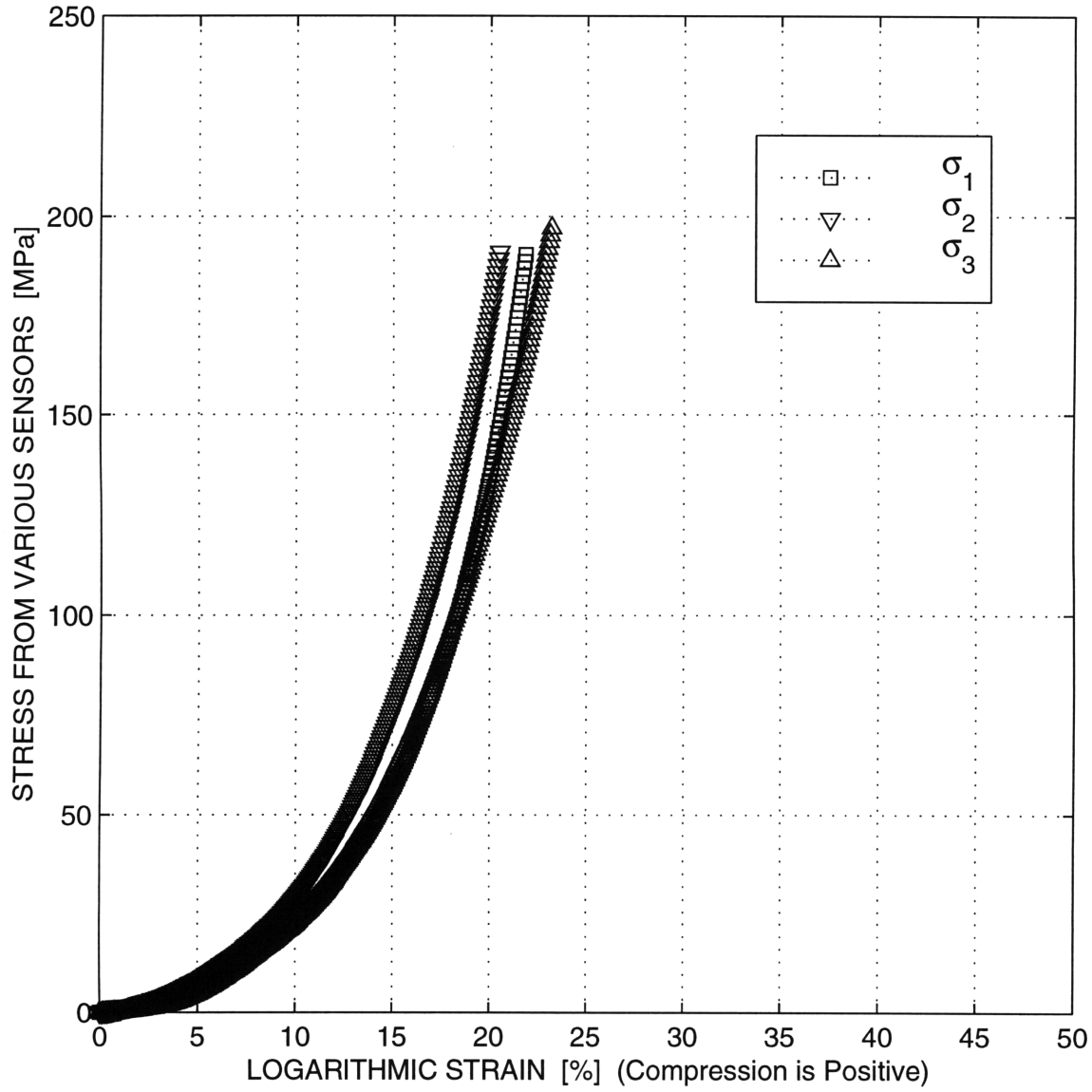

Figure 3-12: Typical stress versus strain measurement using the $45^o_2/45^o_3$ block arrangement for the triaxial compression of ANCOR MH-100 iron powder: test T0221A.

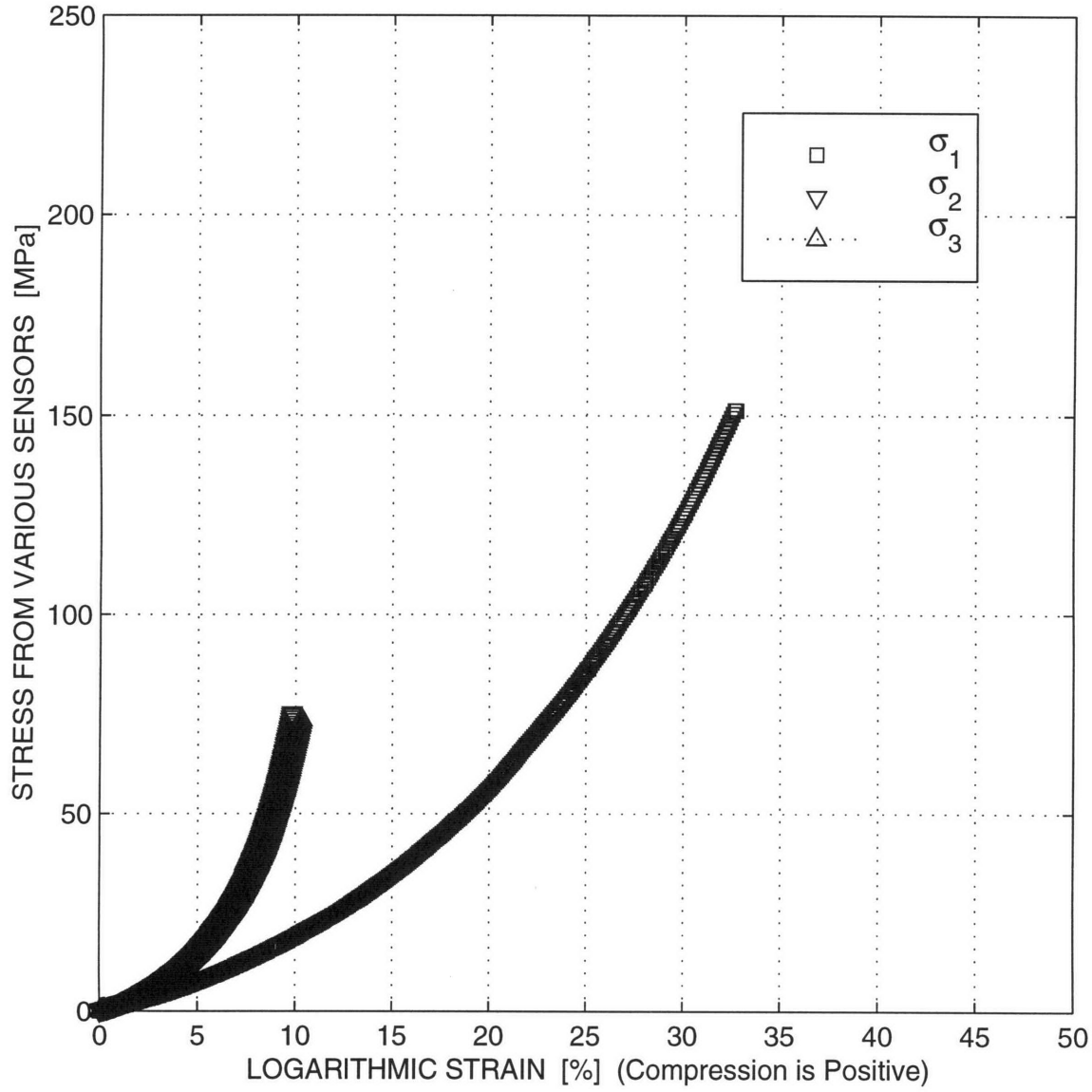

Figure 3-13: Typical stress versus strain measurement using the $70^o_2/70^o_3$ block arrangement for the triaxial compression of ANCOR MH-100 iron powder: test T0614A.

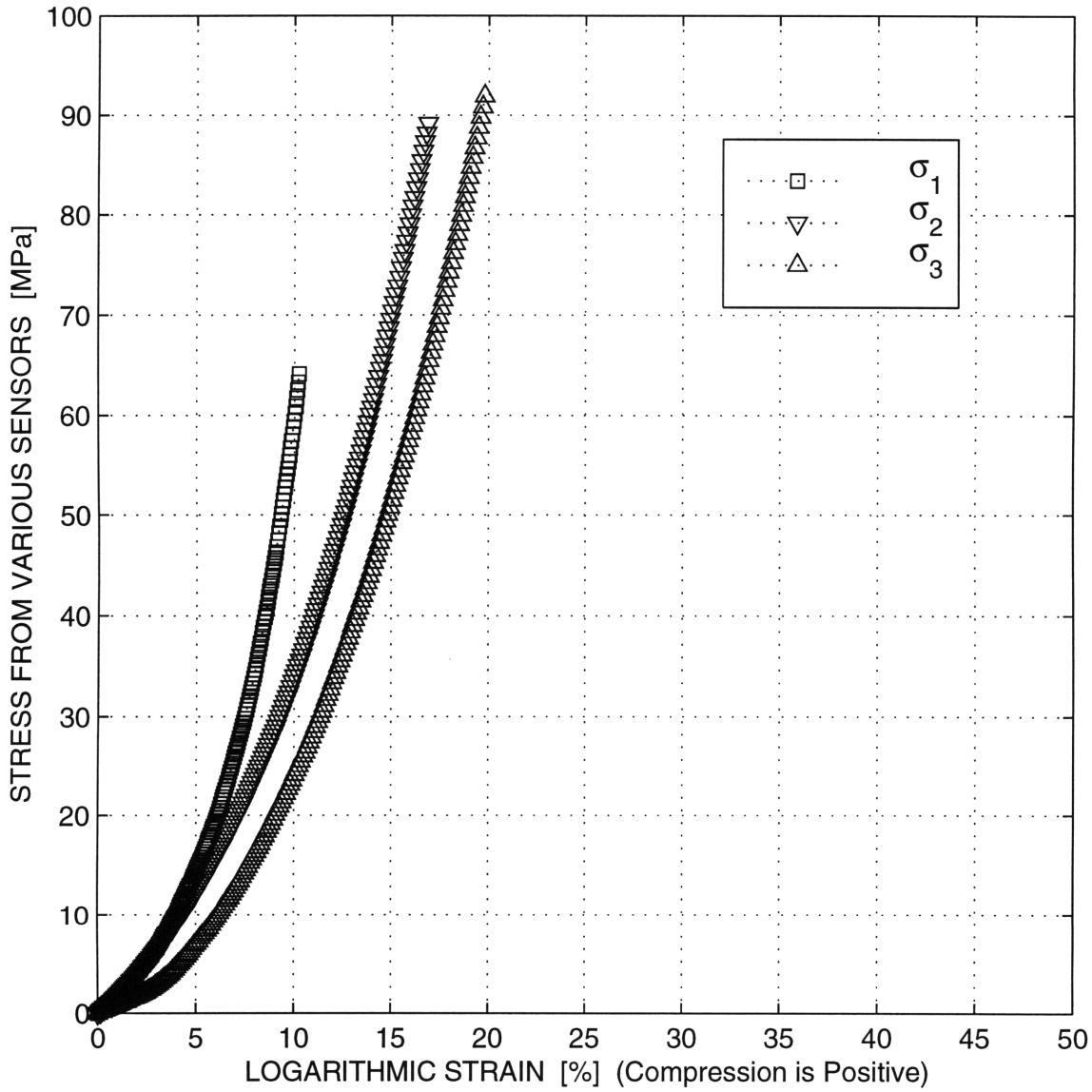

Figure 3-14: Typical stress versus strain measurement using the $30_2^o/30_3^o$ block arrangement for the triaxial compression of ANCOR MH-100 iron powder: test T0222B.

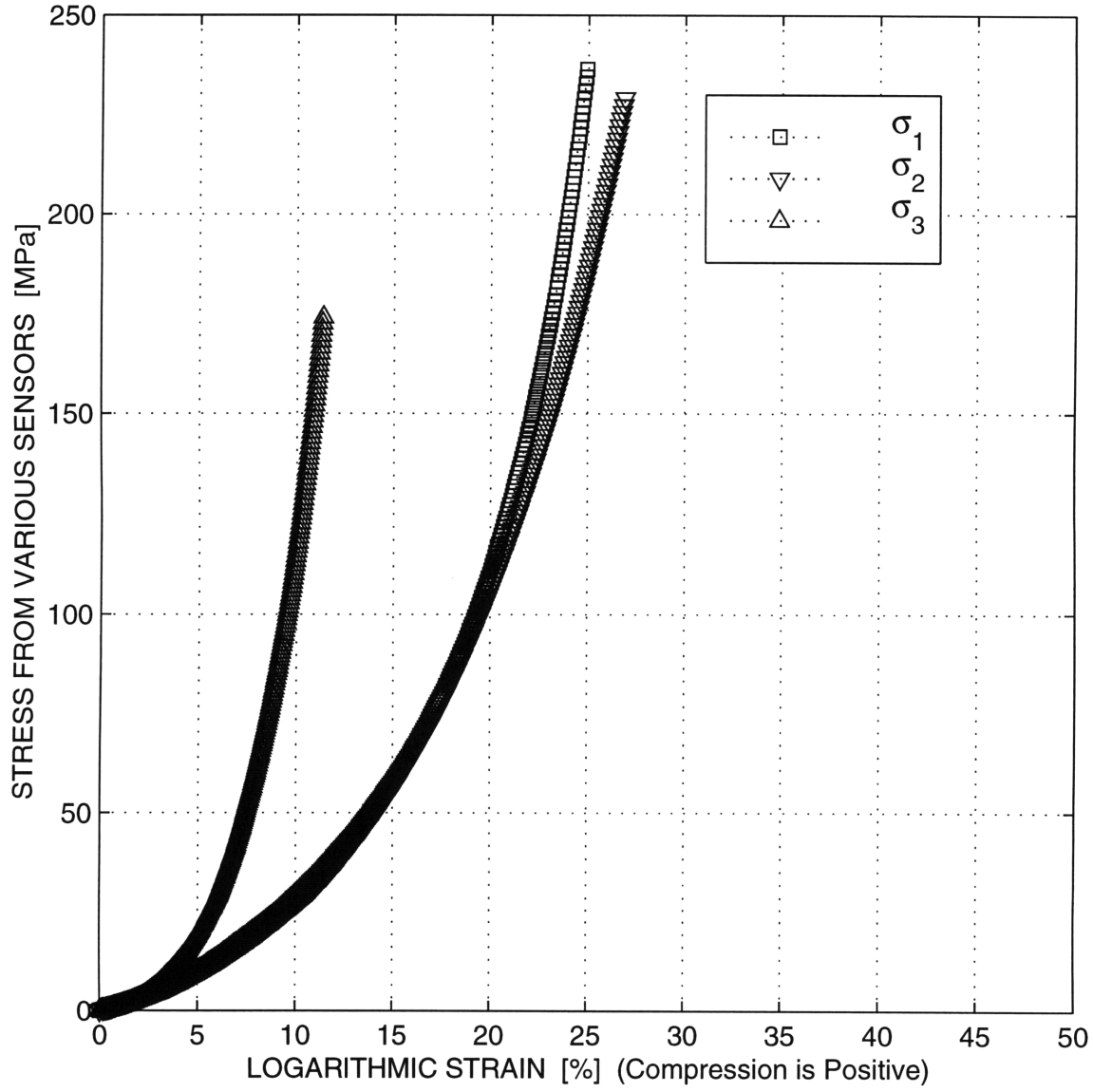

Figure 3-15: Typical stress versus strain measurement using the $45^o_2/70^o_3$ block arrangement for the triaxial compression of ANCOR MH-100 iron powder: test T0222D.

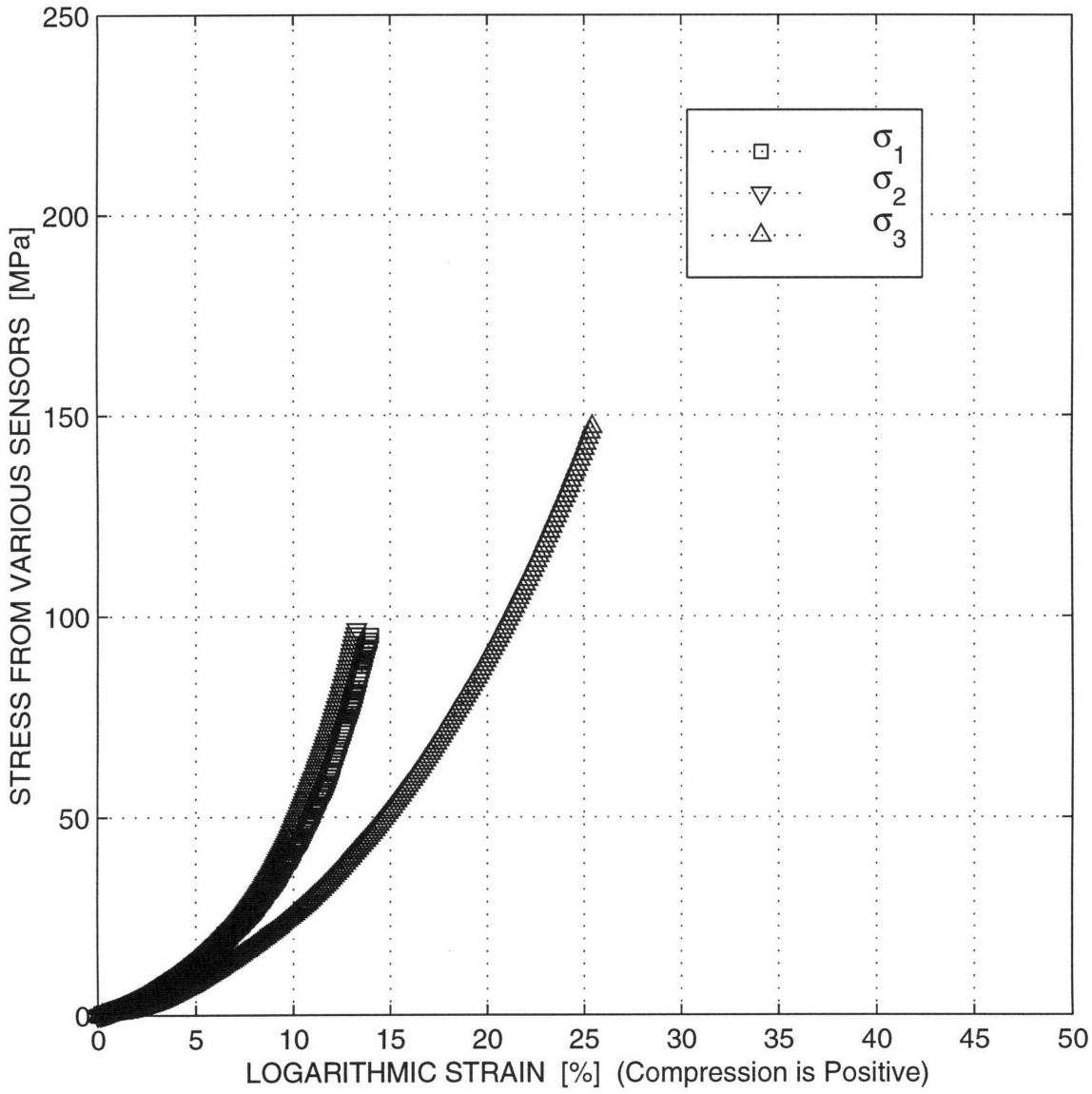

Figure 3-16: Typical stress versus strain measurement using the $45^o_2/30^o_3$ block arrangement for the triaxial compression of ANCOR MH-100 iron powder: test T0222E.

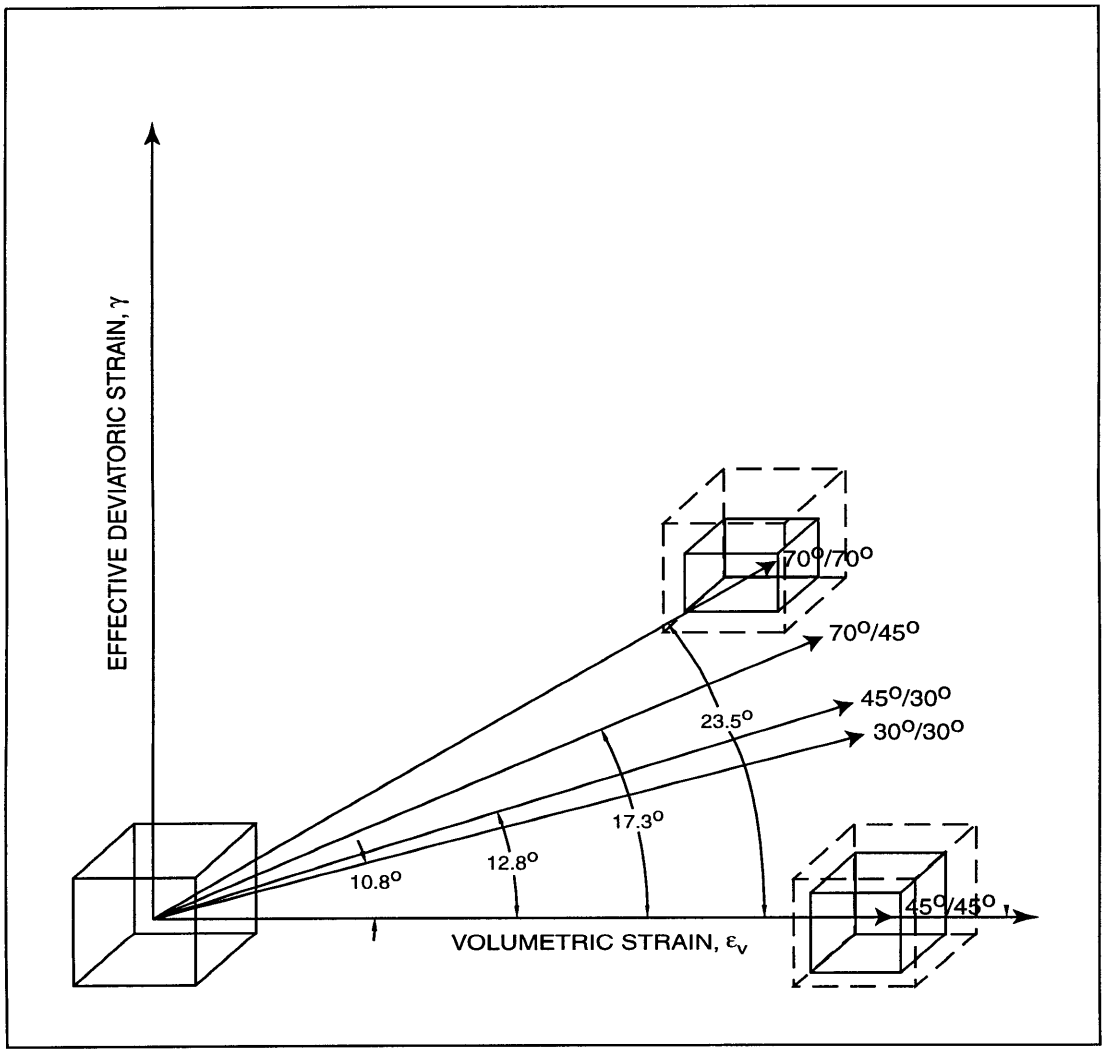

Figure 3-17: Theoretical strain paths traversed during triaxial compression experiments.

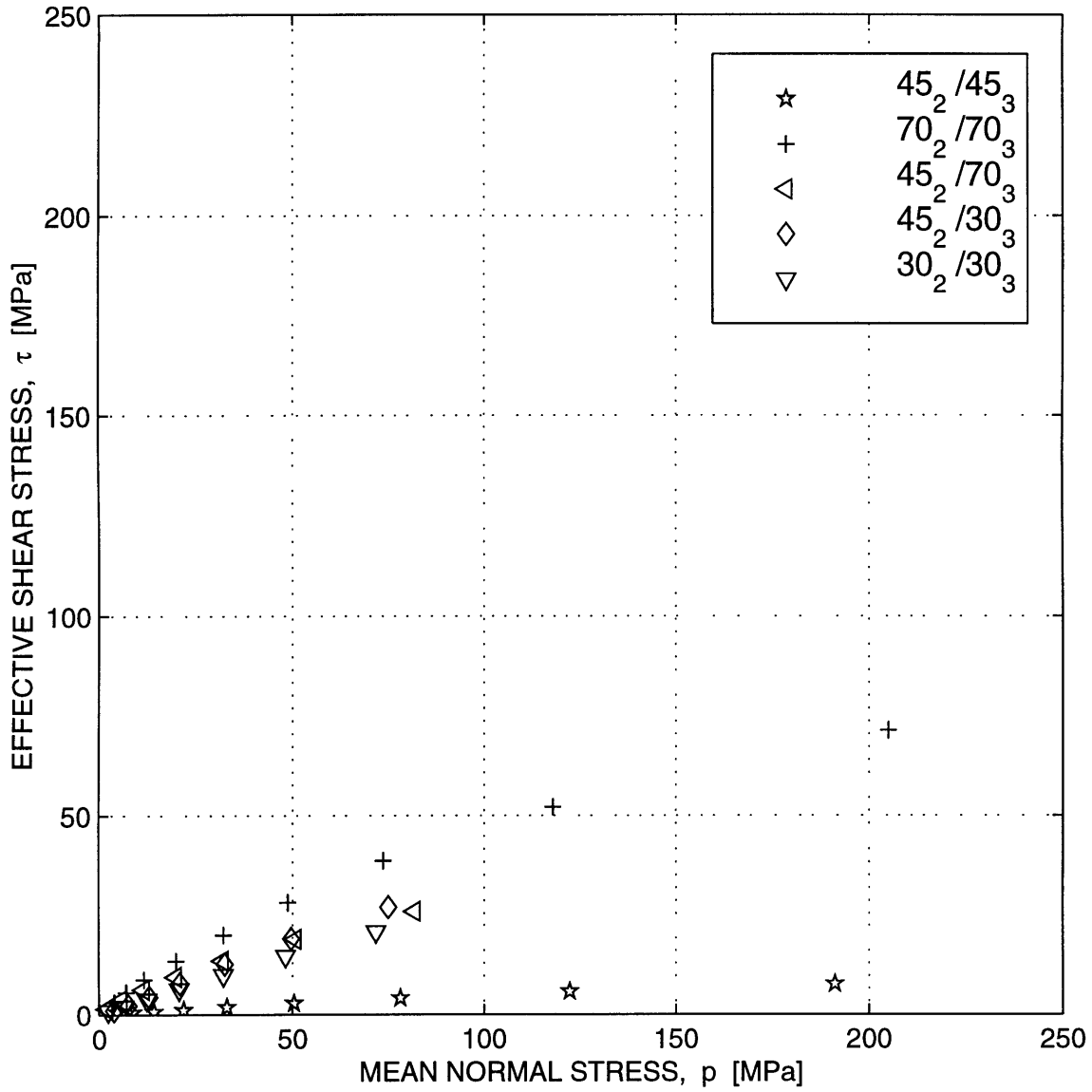

Figure 3-18: Experimentally measured stress paths achieved by triaxial compression experiments of ANCOR MH-100 iron powder.

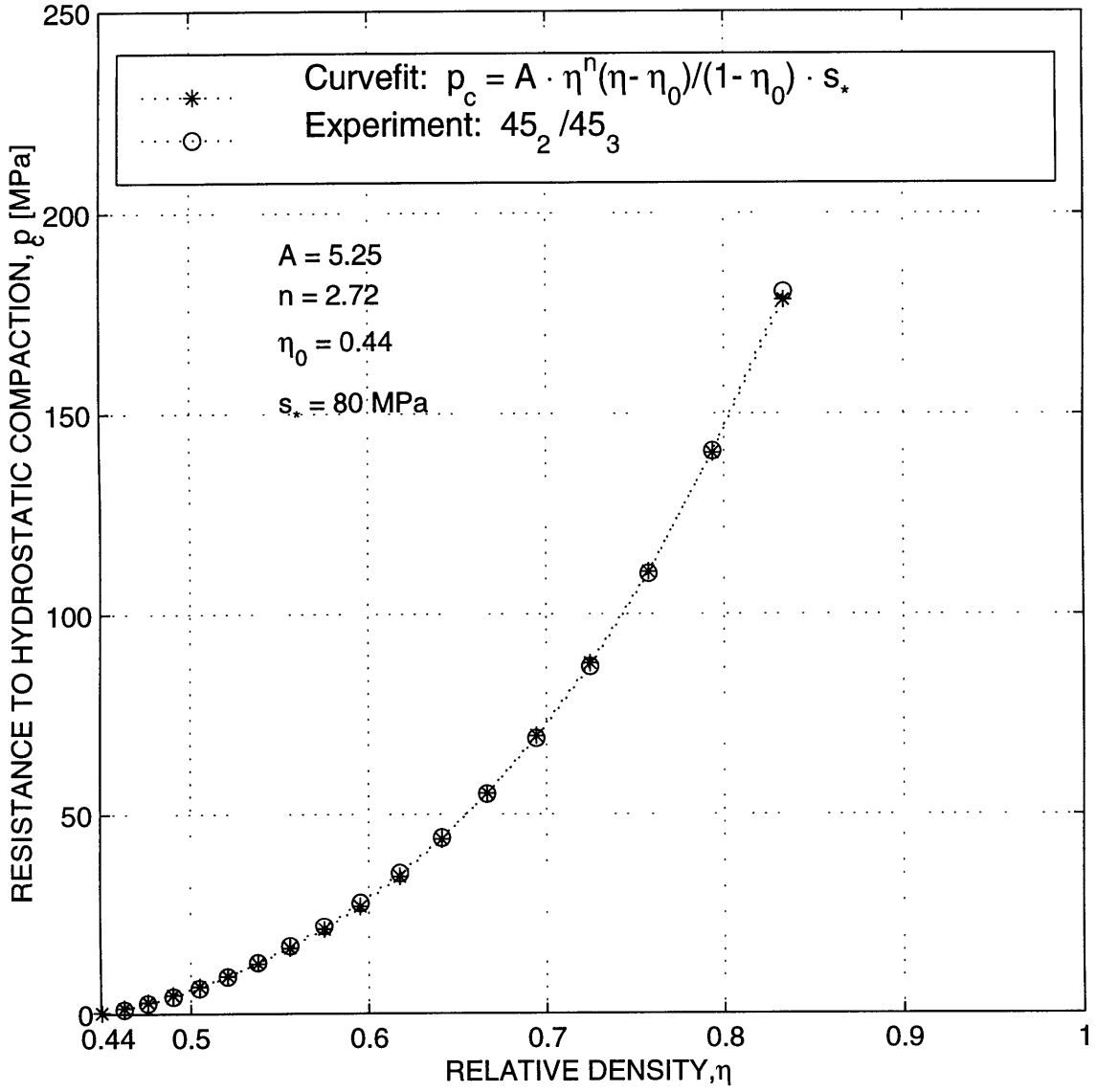

Figure 3-19: Experimentally determined evolution of the resistance to hydrostatic compaction with relative density.

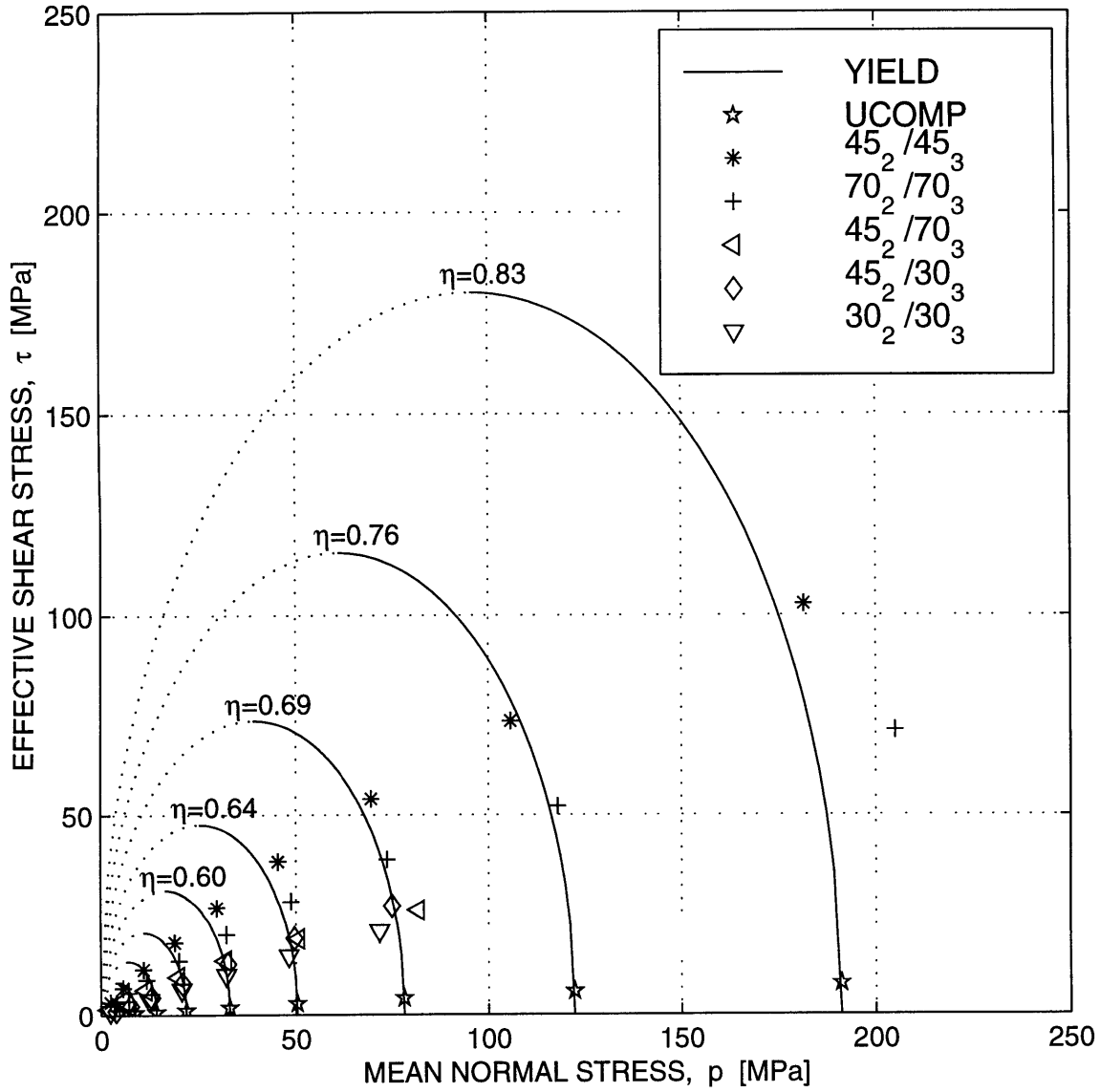

Figure 3-20: Comparison of the triaxial experimental results for the ANCOR MH-100 yield surface with predictions of Cam-clay type yield surface.

3.3 Torsion Ring Shear Tests

3.3.1 Introduction

A torsion ring shear apparatus was designed and fabricated in order to investigate the frictional behavior of ANCOR MH-100 sponge iron powder at large deformations. Although the simplest form of testing the shear response of granular materials is the well established (ASTM D3080-90) direct shear box test, this method was unsuitable in this investigation because the effective cross-sectional area, or metal powder in contact with metal powder, decreases with increasing displacements. Also, the metal powder remaining in the original cross section of the box is still in contact with the metal frames, and the corresponding frictional resistance increases the measured shear load. Approximate corrections can compensate for the influence of some of these sources of error, but such corrections become increasingly uncertain with increasing deformations, and the direct shear box test permits only a limited investigation of the shearing resistance characteristics at large deformations [41].

Many of the difficulties associated with the direct shear box are eliminated when a torsion shear apparatus is used. The first torsion shear machine used in soil mechanics was reported in 1916 (U.S. Bureau of Standards, 1916). It was not until the early 1930's, however, that the rotation shear machine became a significant research tool (e.g., Hvorslev [38]). The early torsion shear machines were stress-control devices. The shape of the stress-deformation curve beyond the peak strength was obtained by adjusting the shear load until a uniform rate of deformation was achieved. In 1947, Hvorslev designed and built a sophisticated rotation shear machine capable of both stress-control and strain-control loading (Hvorslev and Kaufman [39]). Most contemporary rotation shear machines are closely patterned after his basic design and are capable of attaining large deformations in torsion without changing the cross-sectional area.

Although simpler to fabricate, a solid circular specimen geometry in the torsion shear machine is undesirable because the shear stresses and strains in a solid test specimen increase from a maximum at the periphery to a vanishing stress and strain

at the center. Consequently, progressive failure is also nonuniform during the test. Volume changes and linear displacement in a solid cylindrical specimen also vary from a maximum at the periphery to a minimum at the center. The varying changes in height of the specimen are counteracted by radial displacements and plastic flow for the metal powder, but cause an unequal distribution of the vertical normal load. These difficulties in interpreting the results of torsion shear tests are minimized when the specimen has a ring-shaped cross section.

The construction of the torsion shear apparatus could also be simplified and simple external stress conditions could be obtained if the specimen is unconfined laterally. However, tests on unconfined specimens can be performed only when a considerable amount of cohesion exists in the granular material. Furthermore, specimens exhibiting a lot of plastic flow may undergo lateral deformation during and after failure, in which case an investigation of shearing characteristics such as volume changes cannot be made with accuracy. Placing the specimen in a rubber membrane may seem like a viable alternative, however, rubber membranes restrict the permissible deformations and nullify the principal advantage of large deformation in torsion ring shear tests.

Figure 3-21 illustrates the layout of the assembled apparatus and specimen for the adopted method of investigation. An annular ring-shaped specimen, subjected to a constant normal stress σ_z via two annular platens, is confined laterally by inner and outer coaxial confining cylinders. The specimen is ultimately caused to rupture on a plane of relative rotary motion as depicted in Figure 3-22. The confining rings consist of a pair of cylinders, in which case the localized shear surface usually takes place a short distance above the rotating lower platen. The knurled pattern on the surface of this platen causes partial disturbance of the metal powder close to the zone of failure, and therefore should not protrude excessively into the specimen. The friction between the metal powder and confining rings influences the degree of uniform consolidation, and since this influence increases with increasing height of the test specimen, the height of the specimen should be minimized.

The operation of the cell involves constraining the two cylinders and the top ring in the laboratory reference frame while a rotation is imparted to the base plate and

lower platen. This causes the sample to shear, the shear surface forming close to the lower platen (which is roughened to prevent slip at the platen/metal powder interface). The torsion ring shear apparatus is designed so that the total normal load and shear torque being transferred through the granular material across the plane of rotary motion are precisely and accurately known. The displacement of the upper platen during consolidation or shear is monitored by means of a displacement sensor of the same type employed in the triaxial compression experiments bearing on the top of the center cap. The apparatus is a controlled rate of displacement device. The normal load is maintained constant during shear. The variation in the normal load during shear is very small and can be allowed for in the analysis with no loss of accuracy, since the object of the test is to define the ratio of τ to σ_z.

3.3.2 Structural Design

The entire apparatus is constructed of D2 tool steel hardened to Rockwell 61 C. D2 tool steel was chosen for its dimensional stability during heat treatment which resulted in savings by avoiding costly post heat treatment grinding. Making the width of the test section 70 particle diameters of the ANCOR MH-100 sponge iron powder was deemed sufficient to minimize the effect of the confinement boundary.

The remaining dimensions of the cell that needed to be set were the two radii of the cylindrical inner and outer walls. Ideally one would want as large a diameter as possible to reduce the effects of curvature, and attempt to make the curvature of the two walls as close to one another as possible at infinite diameters. At the same time one is faced with the real world limitations of size and weight. These two considerations are based on concerns of bulk, which in excess would make the apparatus very cumbersome to use. Most importantly, the cost of such a device is proportional to the volume. Aware of the torsional capacity of 20 kip-in and that the axial yield strength of solid iron is $\cong$ 80 MPa, the two diameters were set at 2.750 in and 2.500 in, respectively, and then nominal size materials were chosen. The inner diameter of the sample is sufficiently large relative to the outer diameter for uncertainties arising from an assumed non-uniform stress distribution across the

plane of relative rotary motion to be reduced to an acceptable level. The ring shearing system was designed so that the sample (O.D.=69.85 mm., I.D.=63.50 mm., initial height $\cong$ 2 mm) could be subjected to a maximum normal stress of 350 MPa and a maximum shear stress of 100 MPa.

The annular sample is laterally confined between inner and outer confining rings, and is loaded normally (vertically) through annular platens. In order to minimize the risk of slip occurring at the iron powder/tool steel interfaces, a cross-hatched pattern, 200 μm deep(approximately two to four particle diameters deep) and extending the full width of the sample, were provided on the exposed face of each upper and lower annular platen. The effective roughened surface of the upper punch is sufficient to supply a no-slip boundary condition at the top interface, and examination of specimens after shearing verified that the knurl pattern at the top of the specimen was intact. The possibility of failure taking place at the lower interface between the iron powder specimen and the roughened lower platen seems remote when one contrasts the mean size of the ANCOR MH-100 particles (45 μm) with the height of the asperities on the electro-discharge machined annular platen (on the order of 200μm). In tests with ANCOR MH-100 iron, only a thin film of iron adhered to the lower platen when the test was dismantled, ensuring that the residual strength of the powder was measured. The design is modular such that it can accommodate different punches with different surface finishes.

The polished confining rings are liberally coated with Teflon spray to minimize friction at the sidewalls during application of the normal load. The confinement rings are machined with a sliding clearance to rotate around the lower punch, but with a tolerance small enough to prevent any powder from escaping. The presence of Torrington thrust bearings also minimizes friction between the confinement ring and lower turntable. This rotational freedom minimizes error in torque measurements during shearing.

The MTS hydraulic gripping mechanism of the biaxial Instron is the most vital piece to this apparatus, since it supplies the alignment for all the pieces. This mechanism grips the upper and lower grips to which are fastened the upper platen and lower

turntable, respectively. Ten 5/16-18UNCx0.75 socket head cap screws, which attach the upper and lower platens to the upper grip and lower turntable, respectively, are used to transmit the necessary torques up to the maximum torsional capacity of the Instron. Similarly, eight 5/16-18UNCx1-1/4 socket head cap screws, which fasten the lower turntable to the lower grip, are used to transmit the torque to the lower turntable.

3.3.3 Instrumentation

The shear cell is designed to accommodate a linear potentiometer displacement sensor through a port in the upper grip. The reasoning behind the redundant displacement sensor in addition to the Instron axial LVDT was to measure the relative displacement between the annular compression platens and eliminate system compliance due to the load frame and apparatus. Wires may be led from the center of the apparatus to the outside through machined wire reliefs. This feature accommodates future instrumentation such as radial pressure transducers in the wall of the inner confinement ring. The ring shearing apparatus was designed to be used in a biaxial Instron[9] Model 8500 PLUS servohydraulic loading system capable of axial forces up to 225 kN and displacements up to 100 mm. The Instron is also capable of accurately and precisely transmitting a torque of 20 kip-in, and rotations up to 90 degrees. Consequently, the Keithley Series 500 AMM2 analog-to-digital converter, linear potentiometer interface box, and LABTECH Notebook data acquisition software used for the triaxial compression tests are used to accurately and precisely measure and record the axial force, axial displacement, torque, and displacement at a set frequency of 5 Hz.

3.3.4 Test procedure

After pluviating the iron powder in the annular cavity, the shearing resistance is determined by first loading the specimen to generate a uniform normal pressure.

[9]Instron Corporation. 100-TR Royall Street. Canton, MA 02021-1089. Tel: 800.373.6978 http://www.instron.com

Afterward, shearing is commenced via rotation about the axis of symmetry. Two slightly different set-ups are used in our experiments. A roughened lower platen was used for the ring shear tests. The roughened lower platen was replaced with a smooth lower platen for the interface friction tests.

For the ring shear tests, the shearing speed was sometimes increased by 5-25 times the initial slow speed after peak strength, to obtain large deformations more quickly. Readings were taken over the entire period of time at 5 Hz to confirm whether or not a steady state had been achieved.

To simulate the interface frictional behavior between powder compact and confinement dies, the roughened lower platen was replaced with a smooth lower platen. The initial state of the specimen was determined by first loading the interface in compression to generate an initial contact pressure of 68 MPa. Afterwards, torsion interface friction tests were performed by unloading to normal stresses of 51 MPa, 34 MPa, 17 MPa, 9 MPa, and 4 MPa. The entire procedure was repeated with an initial contact pressure of 34 MPa. Finally, the interface was lubricated with Teflon powder spray and the procedure was repeated for initial contact pressures of 68 MPa and 34 MPa. For the interface friction tests, the shearing speed was kept constant at 0.15 mm/sec. Readings were taken over the entire period of time at 1000 Hz.

A summary of the detailed experimental procedures used in the testing are included in Appendix B.

3.3.5 Results and Discussion

The residual strength is the shearing resistance measured in a torsion ring shear test, at which a granular material undergoes continuous deformation under a constant state of stress and at a constant, critical void ratio. The direct results of a torsion shear test are two sets of corresponding values of torque-twist and load-displacement. The actual shearing strains cannot be determined with satisfactory accuracy since the displacements tend to become increasingly concentrated in a localized shear plane as the test progresses, and response is not in a state of uniform simple torsion.

The direct results of a ring shear test are corresponding values of the normal load

F, the total torque M, and the angular displacement θ. The average displacement is calculated on a mean sample radius of 33.34 mm. Assuming that the normal stress σ_z and the shear stress τ_a are uniformly distributed across the plane of relative rotary motion, these quantities are given by:

$$\sigma_z = \frac{F}{\pi(r_2^2 - r_1^2)}, \tag{3.17}$$

and

$$\tau_a = \frac{3M}{2\pi(r_2^3 - r_1^3)}, \tag{3.18}$$

respectively, where $r_1 = 31.75$ mm and $r_2 = 34.93$ mm.

The average sliding distance, δ_a, between the inner and outer boundaries of the test specimen is

$$\delta_a = \frac{\pi}{180}\theta \cdot D_m \tag{3.19}$$

where θ corresponds to the net rotation in degrees, and D_m is the mean diameter in millimeters.

The average rate of displacement, v_a, corresponding to ω revolutions per minute in a controlled-strain test is

$$v_a = \omega \cdot \pi \cdot D_m \tag{3.20}$$

millimeters per minute.

The shear stress normalized by normal stress versus sliding distance curve obtained in a typical shear test is characterized by a sharp peak. The peak shear strength/normal stress occurs at relatively small displacements and the shearing resistance decreases as displacement continues until it finally reaches a constant value, Marone [40].

3.3.6 Normally Consolidated Specimens

Shear stress versus sliding distance curves for the three tests conducted on ANCOR MH-100 iron powder normally consolidated to 25 MPa, 50 MPa, and 75 MPa are shown in Figure 3-24. The mass of powder used was 5 g for all tests. The maximum

average shear stress occurs at sliding distances of 0.01 to 0.03 cm. The shear stress versus sliding distance curves for all these tests reach a peak strength after which there is an abrupt decrease in shearing resistance to about 50% of the peak strength.

The residual strength versus normal pressure line (τ_r) obtained from the tests (Figure 3-25) is a straight line through the origin with a slope of 21.8 deg. The peak strength line (τ_p), also shown in Figure 3-25, is a straight line through the origin with a slope of 38.7 deg.

Figure 3-26 shows a photo of the failure plane at the end of a typical torsion ring shear test. This localized shear plane corresponds to the well-developed Y shears discussed by Marone. Typical failure planes are very shiny and essentially flat with shallow circular striations as shown at a magnification of 200X in Figure 3-27. Striations on the shear surfaces of typical confined ANCOR MH-100 iron powder specimens have a concentric circular pattern. Presence of spiral striations may be indicative of combined tangential and radial displacements on the failure plane.

3.3.7 Overconsolidated Specimens

A series of torsion ring shear tests was performed on ANCOR MH-100 iron powder in which specimens were consolidated to 50 MPa and then unloaded to a stress of 12.5 MPa, 25 MPa, or 37.5 MPa. The mass of powder inserted into the annular cavity was 5 g for all tests. Shear stress versus sliding distance curves for these tests are shown in Figure 3-28 along with the normally consolidated 50 MPa shear stress versus sliding distance curve. Similar to the phenomena observed in soil mechanics, peaks in the shear stress versus sliding distance curves were more pronounced at lower overconsolidation ratios. The residual strength versus normal pressure line obtained from these tests is a straight line through the origin with a slope of 22.6 deg. The failure planes for tests on overconsolidated specimens were very shiny, with no observable difference in shine between these failure planes and those observed in normally consolidated specimens.

3.3.8 Torsion Interface Friction Tests

A tremendous amount of effort has been directed towards the modeling of frictional effects at contacting interfaces (Anand [43], [44]). A typical measurement of the shear stress versus sliding distance, at a constant normal pressure of 68 MPa and a constant shearing rate of 0.15 mm/sec is shown in Figure 3-29. During the experiment the twisting was stopped and reversed by a small amount such that a complete unloading of the interface was achieved. The normal pressure was decreased to 51 MPa, and the shearing in the forward direction was resumed. Figure 3-29 shows the evolution of the state of the specimen surface with the sliding distance for normal pressures of 68 MPa, 51 MPa, 34 MPa, 17 MPa, 9 MPa, and 4 MPa.

To assess the initial pressure dependence and the sliding distance dependence of the shearing resistance, another constant shearing rate torsion interface friction test was conducted at normal stresses of 34 MPa, 34 MPa $\rightarrow$ 17 MPa, 34 MPa $\rightarrow$ 8 MPa, 34 MPa $\rightarrow$ 4 MPa, and 34 MPa $\rightarrow$ 2 MPa. Results of the five tests are shown in Figure 3-30. As can be seen in Figure 3-33, the effect of initial normal pressure on the coefficient of friction of the non-lubricated interface is very small.

Next, Teflon powder spray was liberally applied on the smooth lower platen. To assess the effect of the Teflon lubricant, the loading-unloading experiments were repeated at initial normal pressures of 68 MPa and 34 MPa. Typical measurements of the shear stress versus sliding distance, at normal pressures of 68 MPa and 34 are shown in Figure 3-31 and Figure 3-32, respectively. As can be seen in Figure 3-33, the effect of initial normal pressure on the coefficient of friction of the lubricated interface is also very small. In addition, the application of Teflon powder spray significantly reduced the coefficient of friction.

3.3.9 Conclusion

The torsion ring shear apparatus provides a means for studying shear stress-sliding distance properties of granular materials at large deformations. The simple torsion ring shear apparatus is capable of accurately and precisely measuring both normal

stresses, shear stresses, and sliding distances.

The frictional behavior of ANCOR MH-100 sponge iron powder was investigated using this torsion ring shear apparatus, and the residual strength line and peak strength line were determined to have internal angles of friction equal to 21.8 deg and 38.7 deg, respectively, for normally consolidated specimens.

A series of torsion ring shear tests was performed on ANCOR MH-100 iron powder in which specimens were consolidated to 50 MPa and then unloaded to a stress of 12.5 MPa, 25 MPa, or 37.5 MPa. The residual strength line from these tests was not significantly different from the torsion shear tests on the normally consolidated specimens. These results are qualitatively consistent with the torsion ring shear tests of investigators such as La Gatta [41] and Bishop et. al [42] on normally consolidated clays at low normal pressures.

Tests were also conducted by replacing the roughened lower platen with a smooth lower platen to simulate the important interface friction between powdered specimens and confinement dies. The effect of initial normal pressure on the coefficient of friction between the specimen and platen was very small. Application of Teflon lubricant, however, significantly reduced the coefficient of friction from $\cong 0.4$ to below 0.1.

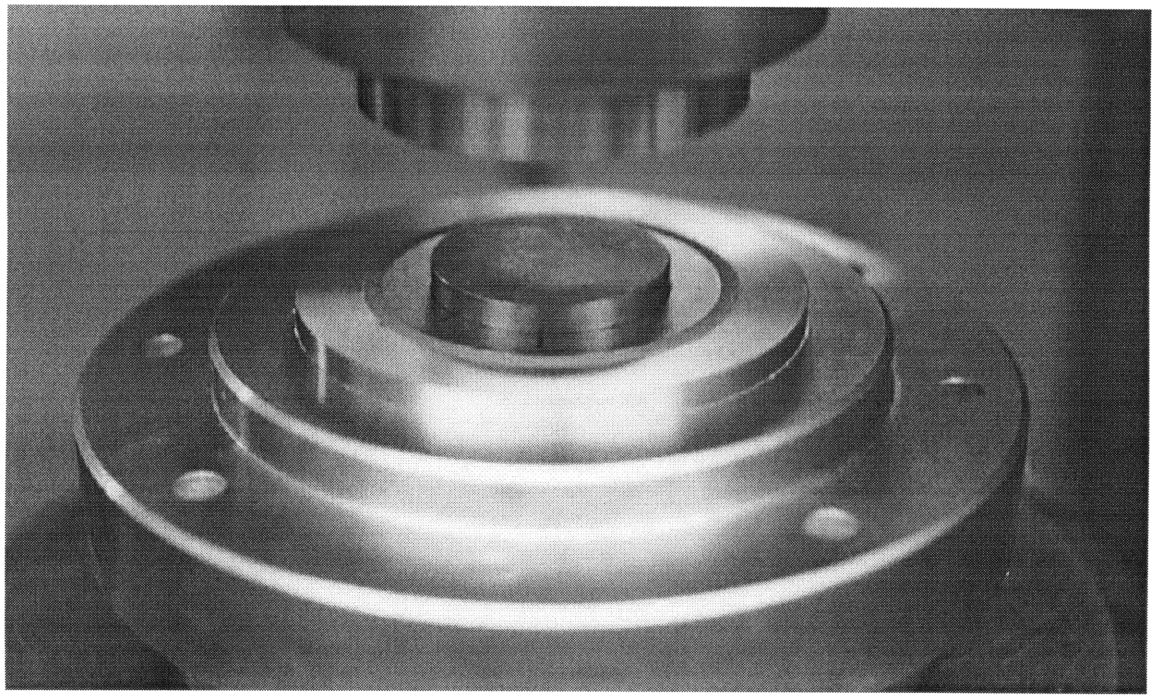

Figure 3-21: Photo of torsion ring shear test system assembled apparatus and specimen.

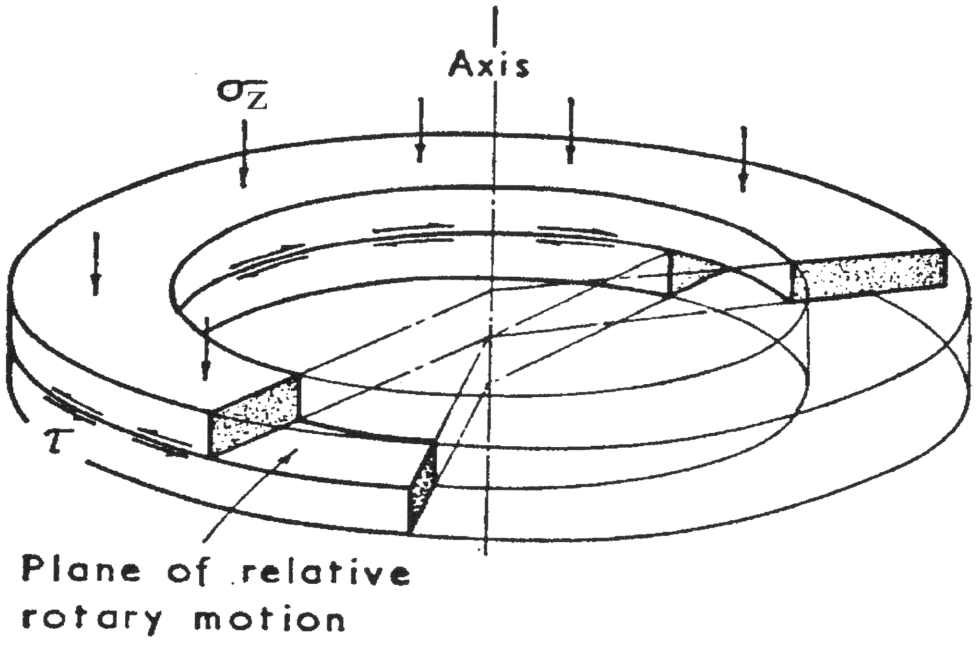

Figure 3-22: Sketch of plane of relative rotary motion. After [42]

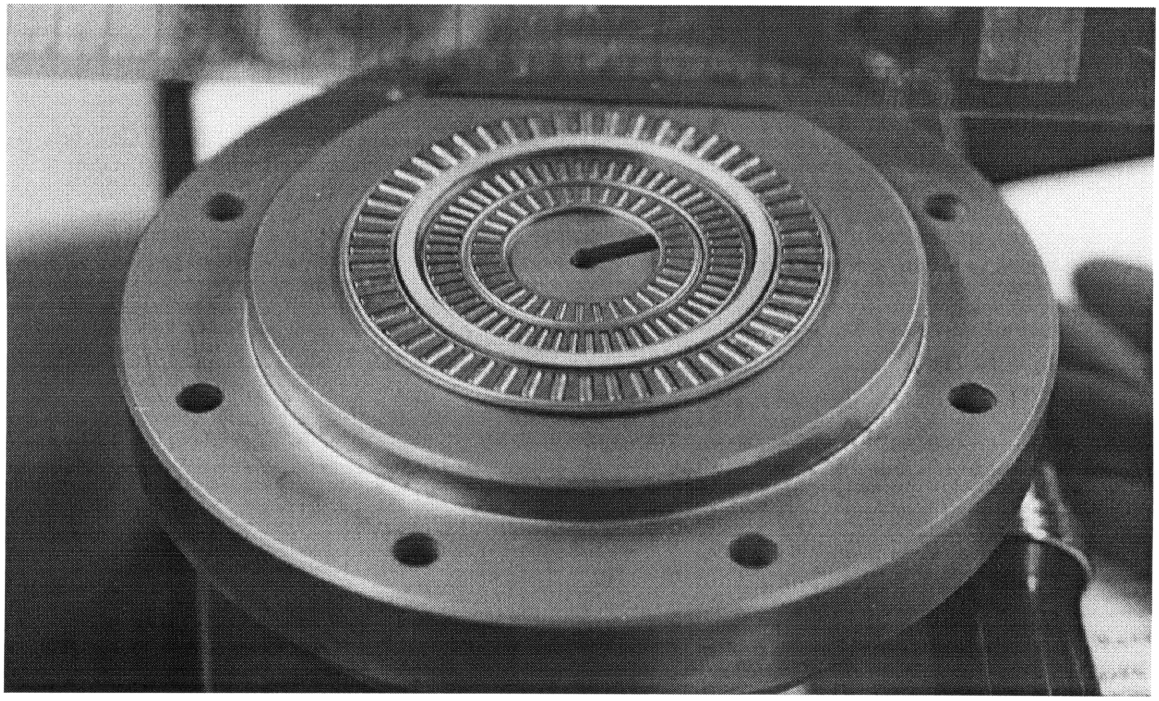

Figure 3-23: Photo of ring shearing test system thrust bearings.

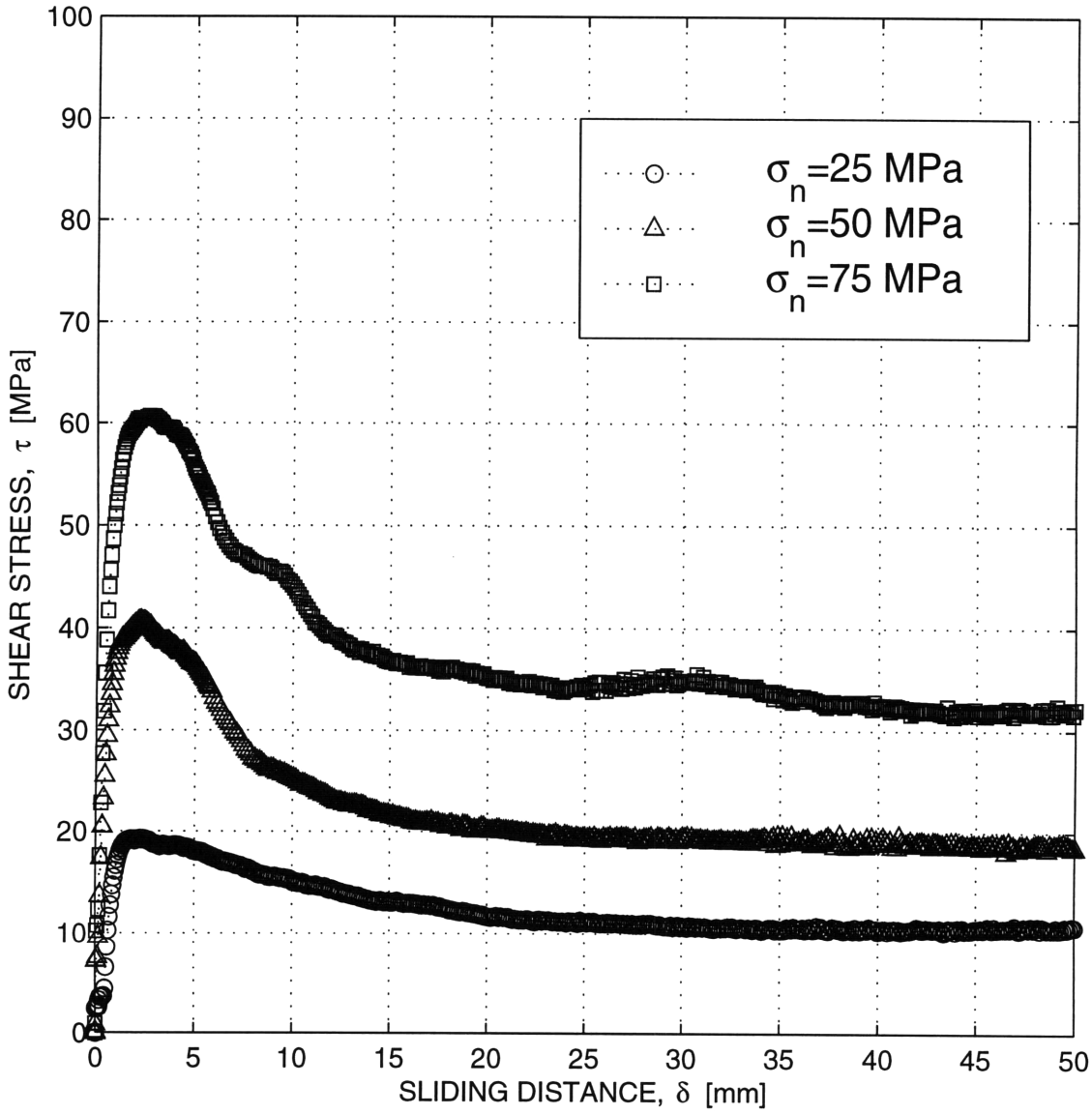

Figure 3-24: Shear stress-sliding distance relationship for normally consolidated ANCOR MH-100 sponge iron powder: test R0829A.

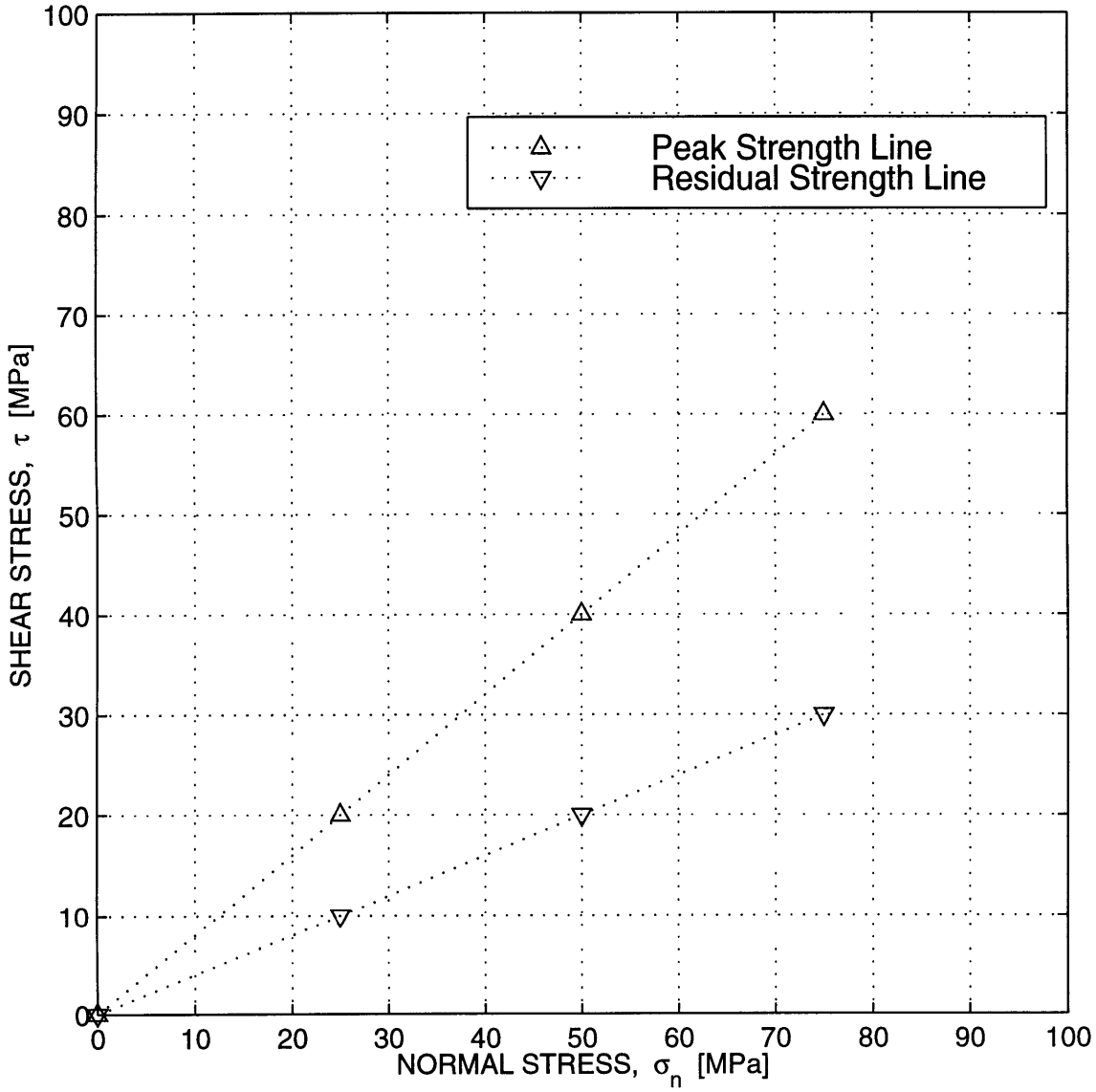

Figure 3-25: Residual strength line and peak strength line for normally consolidated ANCOR MH-100 sponge iron powder: test R0829A.

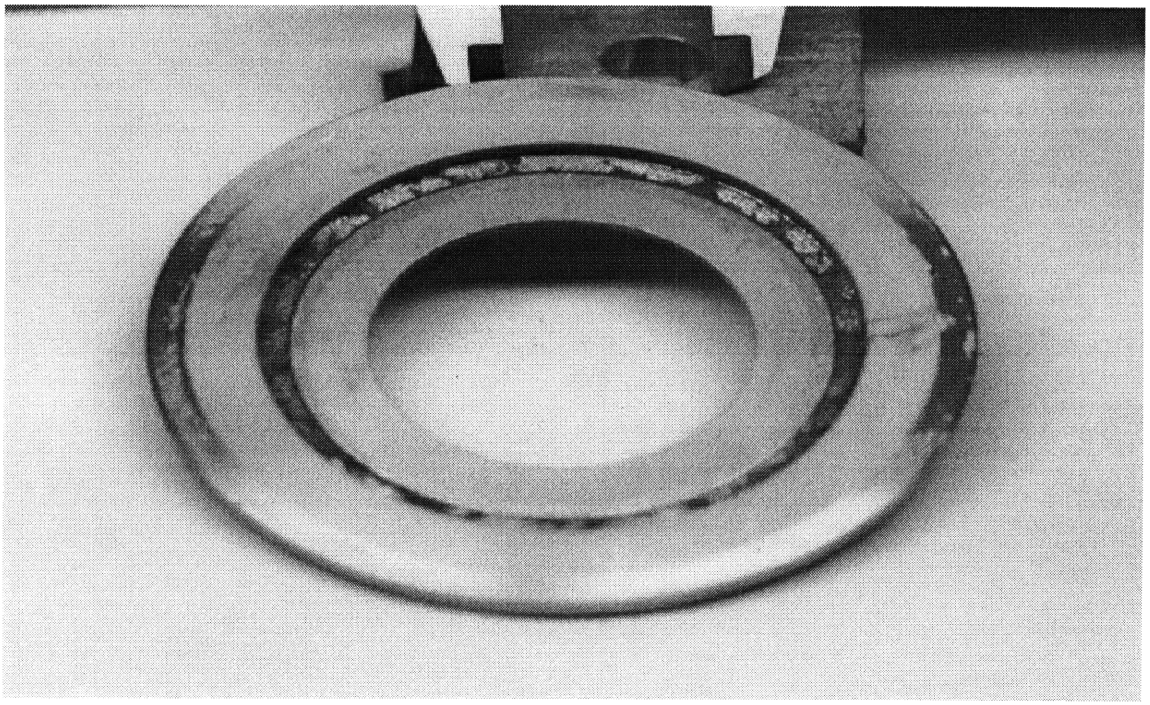

Figure 3-26: Typical torsion ring shear test specimen.

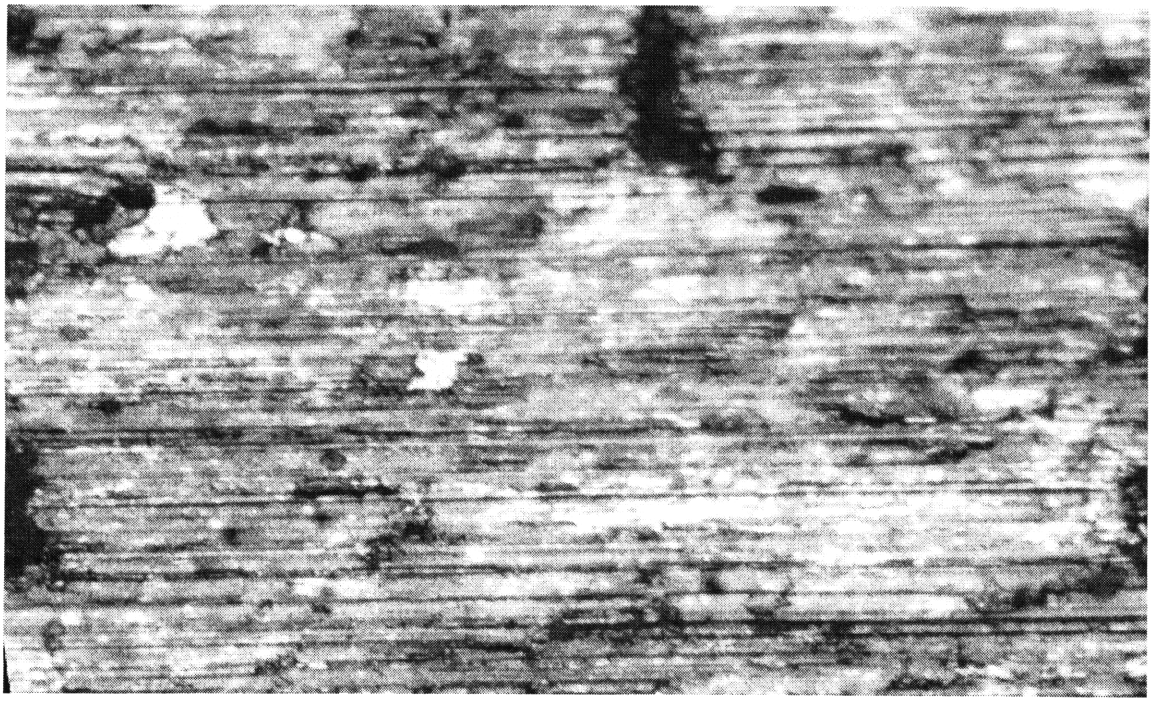

Figure 3-27: Typical torsion ring shear specimen failure plane striations concentric to the axis of rotation. [Magnification 200X.]

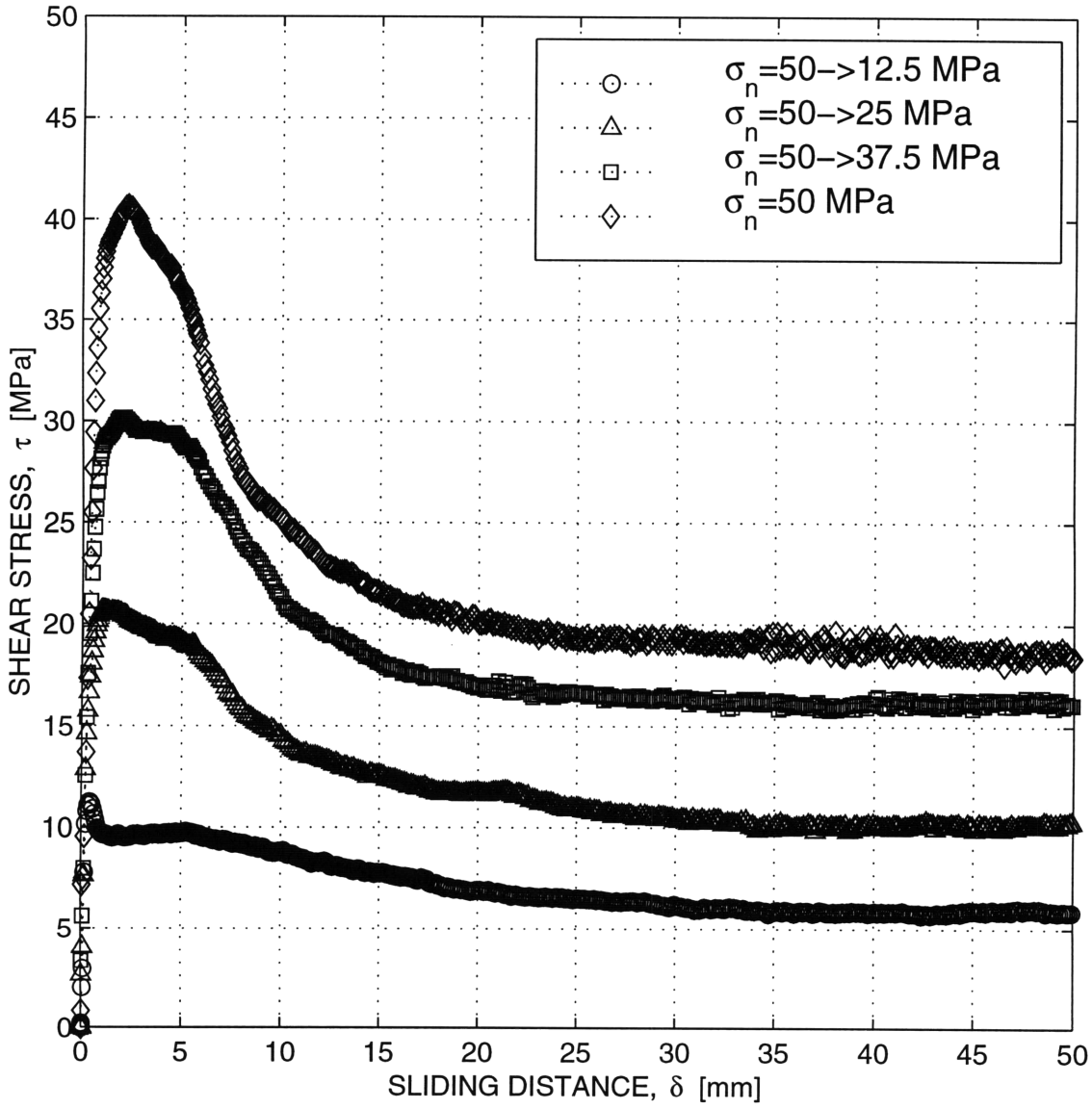

Figure 3-28: Shear stress-sliding distance relationship for over-consolidated ANCOR MH-100 sponge iron powder: test R0830A.

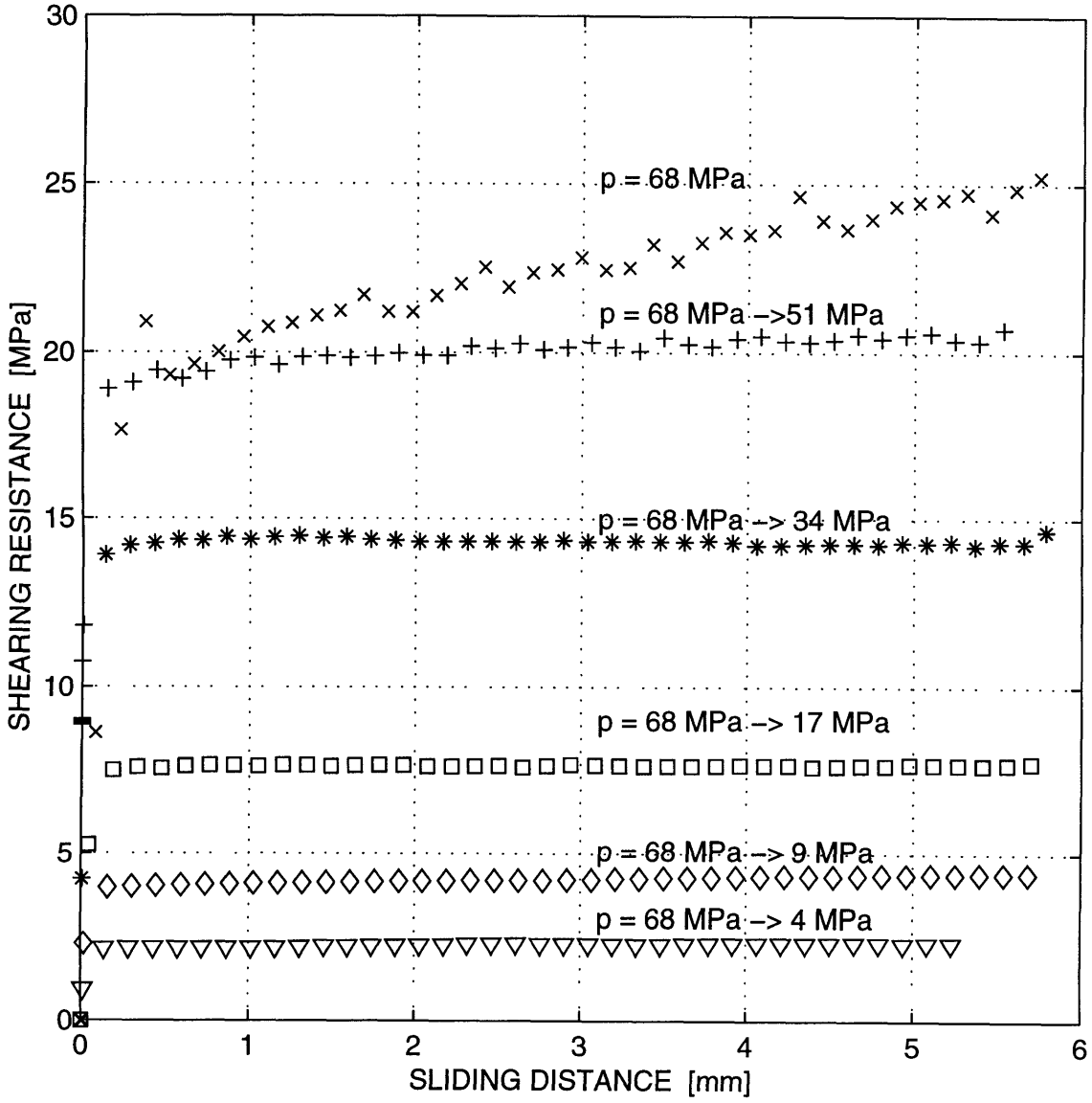

Figure 3-29: Interface friction experiments at six different normal pressures of 68 MPa, 68 MPa $\rightarrow$ 51 MPa, 68 MPa $\rightarrow$ 34 MPa, 68 MPa $\rightarrow$ 17 MPa, 68 MPa $\rightarrow$ 9 MPa, 68 MPa $\rightarrow$ 4 MPa: test F1027J.

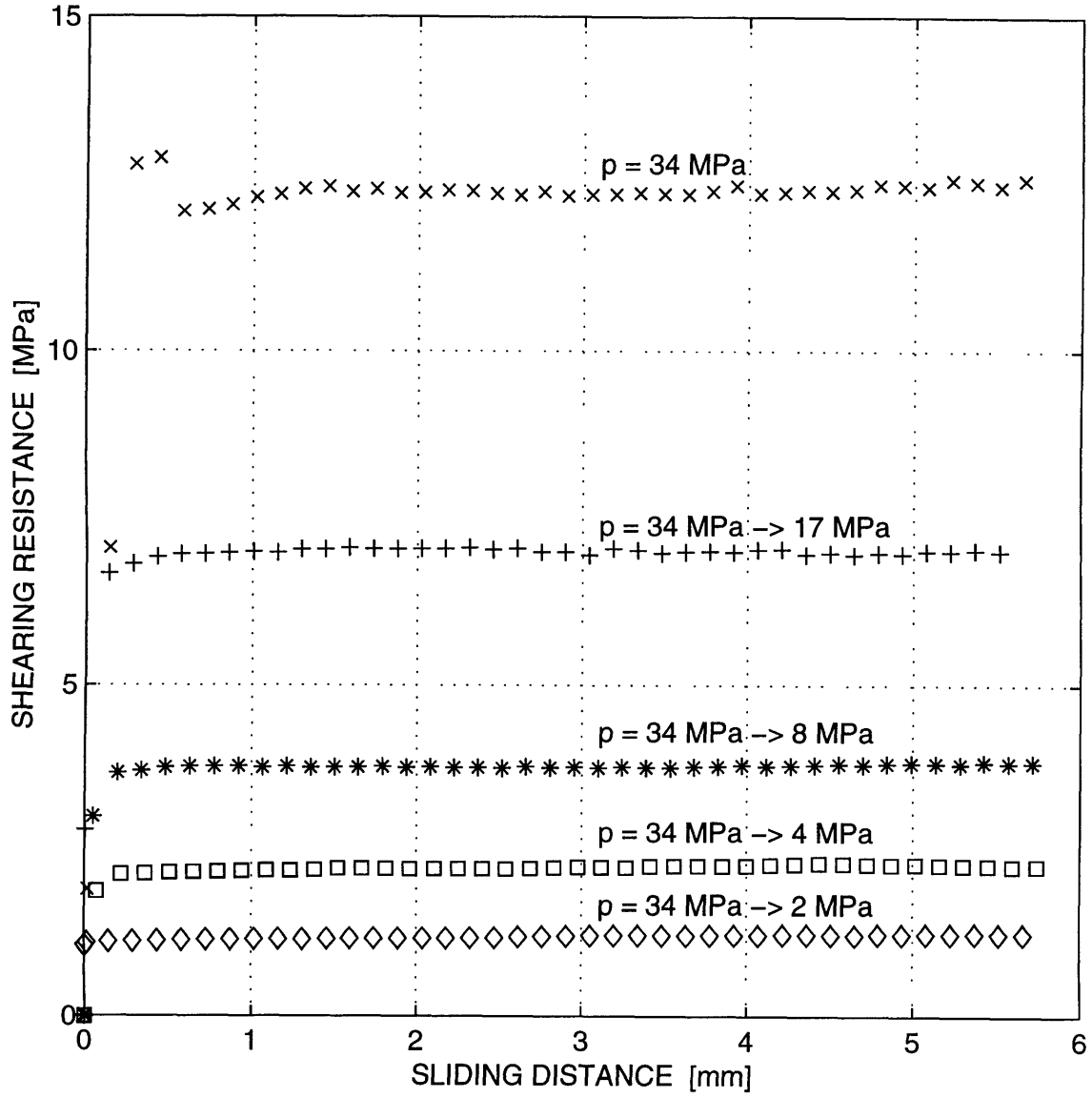

Figure 3-30: Interface friction experiments at five different normal pressures of 34 MPa, 34 MPa $\rightarrow$ 17 MPa, 34 MPa $\rightarrow$ 8 MPa, 34 MPa $\rightarrow$ 4 MPa, 34 MPa $\rightarrow$ 2 MPa: test F1028A.

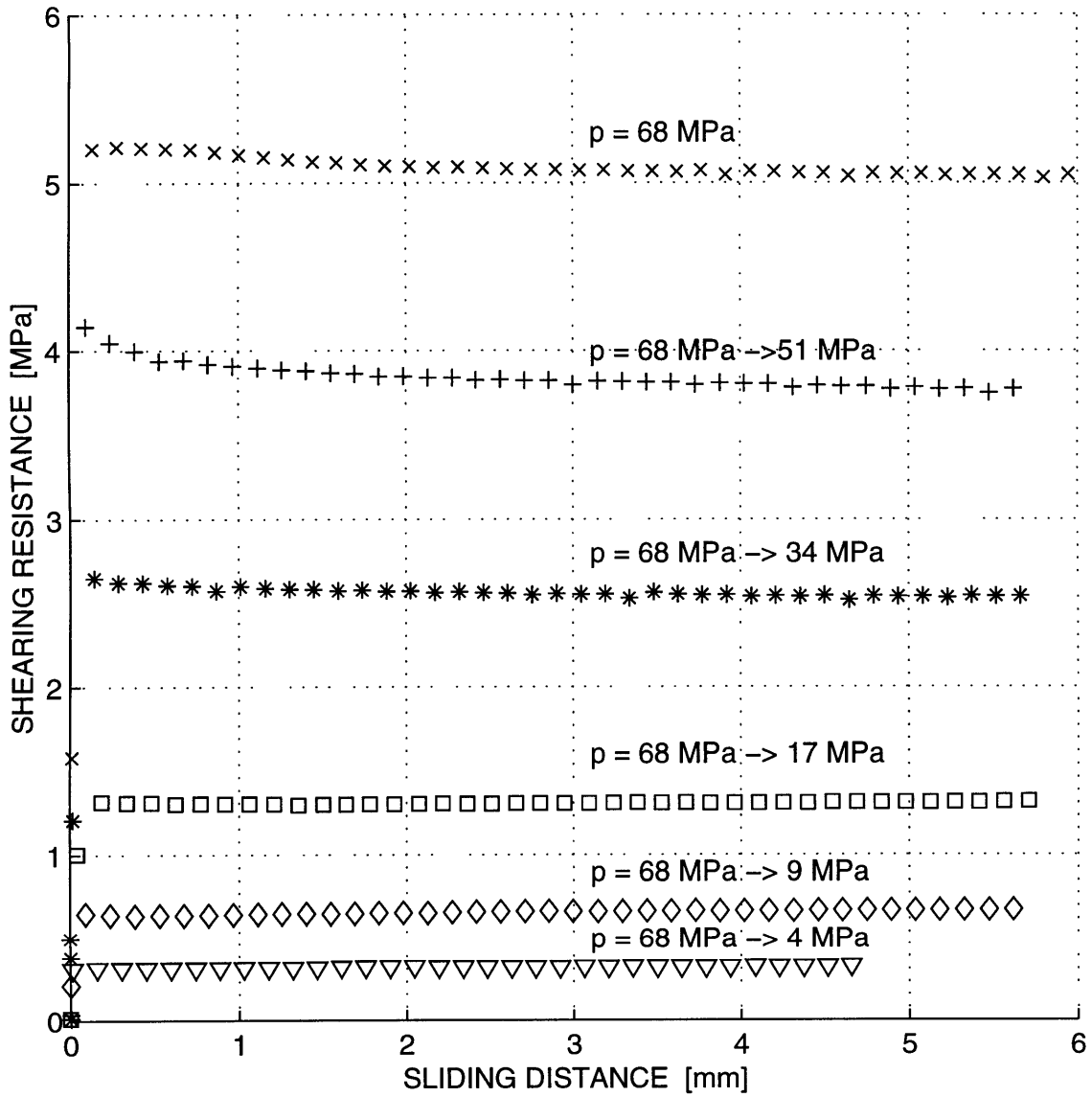

Figure 3-31: Teflon lubricated interface friction experiments at six different normal pressures of 68 MPa, 68 MPa $\rightarrow$ 51 MPa, 68 MPa $\rightarrow$ 34 MPa, 68 MPa $\rightarrow$ 17 MPa, 68 MPa $\rightarrow$ 9 MPa, 68 MPa $\rightarrow$ 4 MPa: test F1028F.

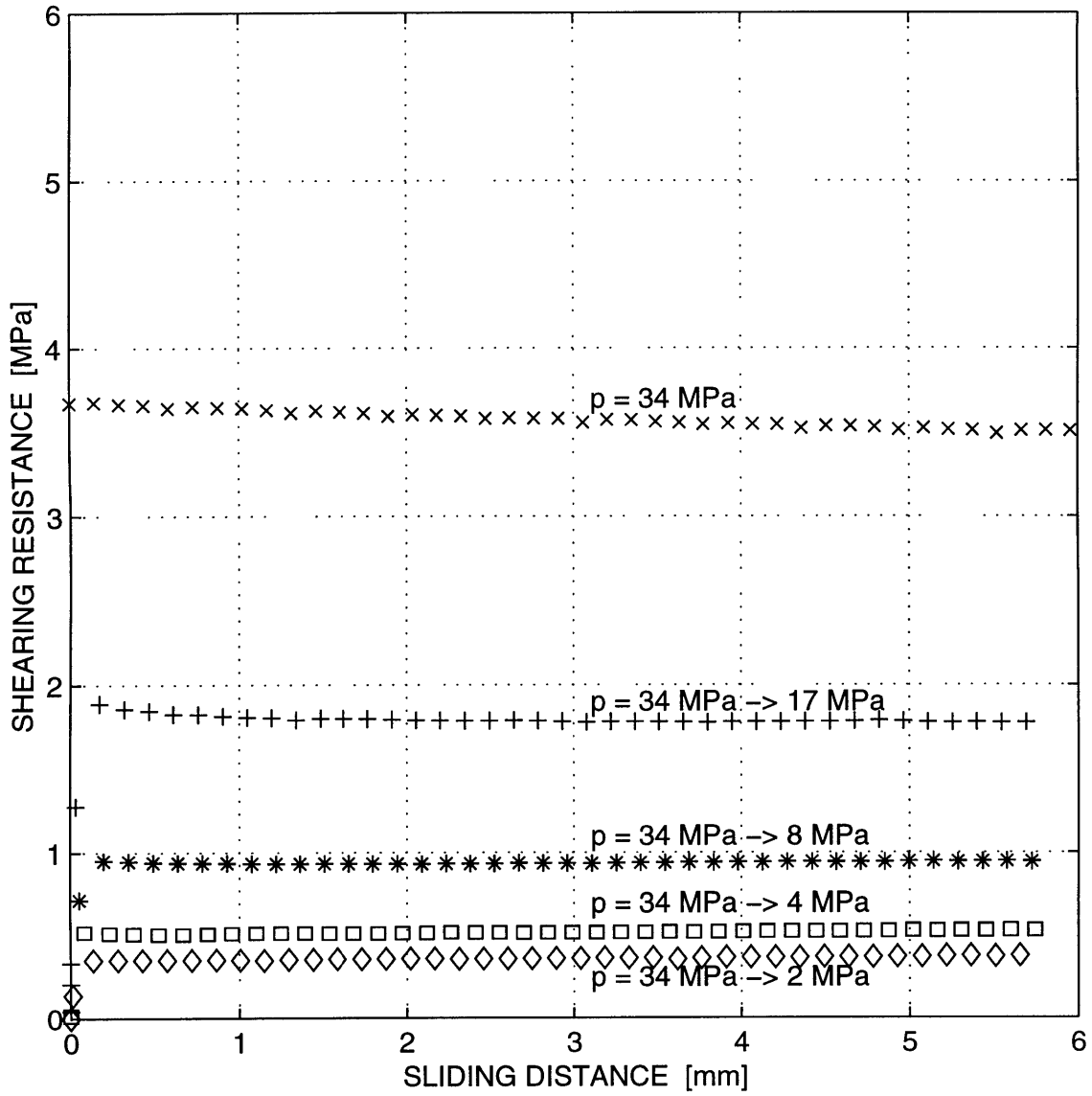

Figure 3-32: Teflon lubricated interface friction experiments at five different normal pressures of 34 MPa, 34 MPa $\rightarrow$ 17 MPa, 34 MPa $\rightarrow$ 8 MPa, 34 MPa $\rightarrow$ 4 MPa, 34 MPa $\rightarrow$ 2 MPa: test F1029A.

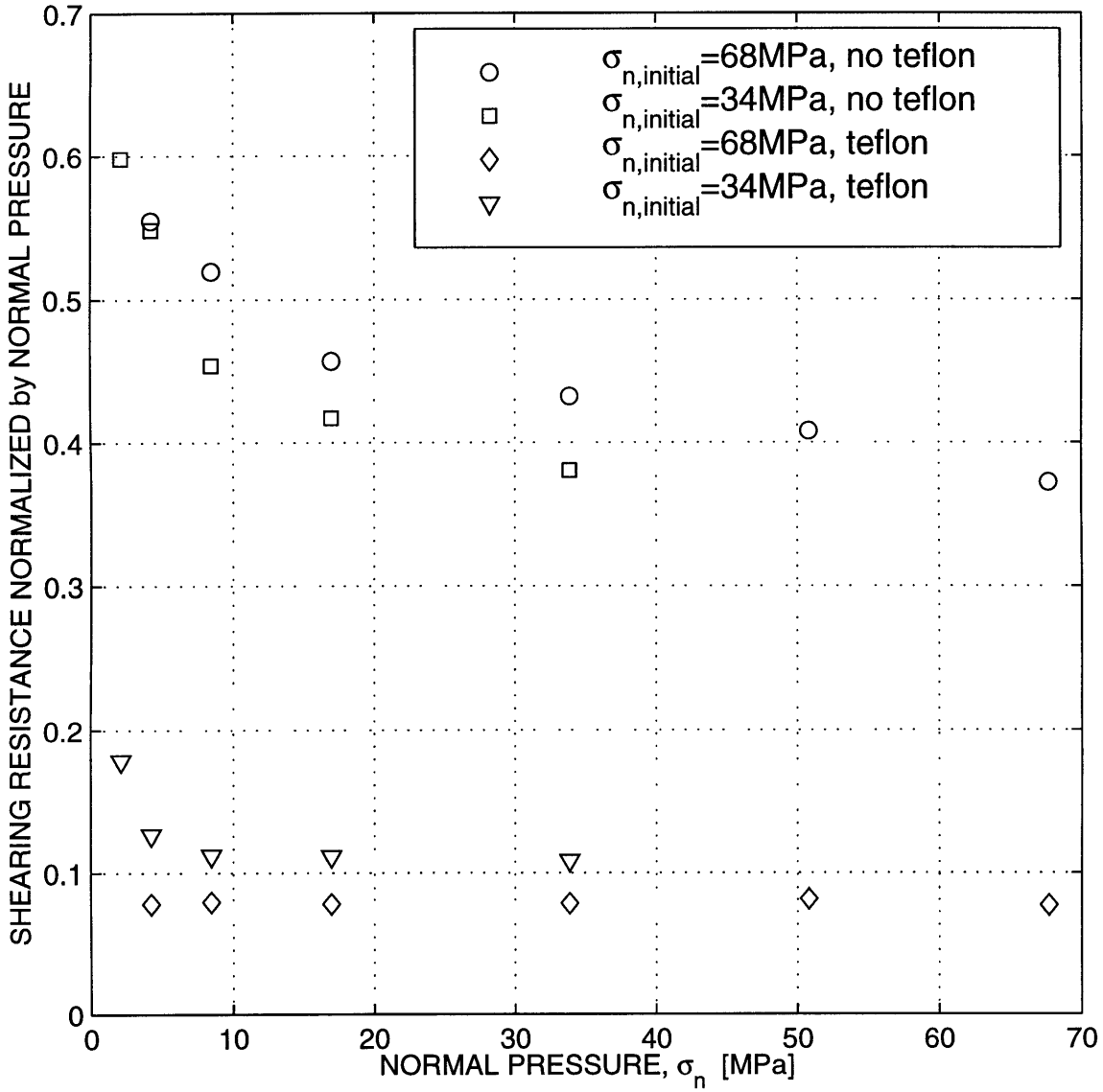

Figure 3-33: Evolution of coefficient of friction with normal pressure.

3.4 Uniaxial Strain Compression Tests

3.4.1 Experimental Setup

The flow behavior of ANCOR MH-100 sponge iron powder was evaluated using a uniaxial strain compression system, which was also designed, fabricated, and documented by Abou-Chedid (1993) [34]. The apparatus consists of a cylindrical die with upper and lower compression platens that compact the granular material within a cylindrical test volume. The 76.2 mm thick walled cylinder and ϕ25.4 mm piston used in the present study were fabricated from A2 tool steel. The high surface hardness (Rockwell C 61) after heat treating also helps to avoid surface scoring and scratching during testing. A vertical cross-sectional view of the uniaxial strain compression system is shown in Figure 3-34.

The axisymmetric test specimen diameter is 25.4 mm. The 225 kN capacity of the biaxial Instron Model 8500 PLUS servohydraulic loading system produced axial stresses up to 450 MPa. The specimen height can be variable, but an initial specimen height of approximately 12.7 mm was generally used.

The Instron's load cell along with the cross-sectional area was used to calculate the upper axial normal stress. A strain gauged pressure sensor (identical to the one used in the triaxial compression system) on the lower compacting surface was used to measure the lower axial normal stress, while a lateral strain gauged pressure sensor measured the radial normal stresses. The Keithley and LABTECH Notebook data acquisition system described for the triaxial compression system were used to measure and record the normal stresses, radial stress, and axial deformation at a set frequency of 20 Hz.

In order to obtain a uniform initial density distribution within the specimen, the sponge iron powder was carefully pluviated with a measured mass of particles (approximately 0.050 kg). Different densities can be achieved by controlling the falling height and diameter of the funnel. The surface of the specimen was kept parallel to the base plate to minimize final height imperfection.

Accurate determination of the vertical deformation is quintessential for accurate

estimation of the relative density. Corrections to the axial deformation of the specimen for the loading system compliance were performed on all test data. This was accomplished by performing load tests in the testing setup without a specimen to the maximum load employed in the tests on the MH-100 iron powder. A typical uniaxial strain compression system compliance displacement correction curve has been included in Figure A-7 in Appendix A. No corrections were made for the elastic expansion of the containment cell during loading, because they were analytically determined to be insignificant in a uniform cylinder under full internal pressure. (Roark and Young [45])

Minimization of sidewall friction is essential for accurate determination of the effective vertical stress within the specimen below that applied by the platen at the top of the specimen. The maximum axial stress occurs at the top of the specimen, and the lowest stress condition would be at the bottom of the specimen. The vertical axial stress gradient also creates a gradient in the horizontal stresses as applied by the granular material to the cell wall, relative to the vertical stress applied to the top of the specimen. Abou-Chedid tested a variety of lubricants via rotary friction tests and concluded that Teflon powder was the best lubricant which significantly reduced the friction between the powder and the die wall. In addition, to minimize the effect of these side friction forces the thickness to diameter ratio of the specimen was kept small, generally 1:2. The state of stress was assumed to be principal because of the Teflon lubricant applied to the die walls and the small thickness to diameter ratio. The detailed uniaxial strain compaction procedure is provided in Appendix B.

3.4.2 Results and Discussion

Typical loading and unloading axial stress-strain curves for Hoeganaes Ancor MH-100 iron powder with initial relative density $\eta_o = 0.42$ subjected to a double ramp load-unload cycle $\sigma_z = 0MPa \rightarrow 450MPa \rightarrow 0MPa$ at a rate $890N/sec$ in uniaxial strain are shown in Figure 3-35.

A strain-gaged lateral pressure sensor was used to measure radial stress, and recorded the cycle: $\sigma_r = 0MPa \rightarrow 175MPa \rightarrow 125MPa$. Since the uniaxial strain

test is a fully confined test, the maximum capacity of the load system determined the termination point of the test. Figure 3-35 clearly shows that the stiffness of the granular material continually increases as strain increases.

Since the uniaxial strain die cavity is completely confined and the mass of the specimen can be determined after the test, the data on the specimen height is sufficient to calculate the current volume and corresponding relative density. The relative densities plotted against the corresponding axial stress for MH-100 are shown in Figure 3-36.

The relative density is seen to change more rapidly at low stress levels. Large volume reductions occur as particle deformation and rearranging increased with increasing axial stress. The relative density is seen to change more rapidly at low stress levels, and asymptotically approaches $\eta = 1$ as the material becomes fully compacted and no further void collapse takes place.

3.4.3 Uniaxial Strain Compression Loading Path

Analogous to the triaxial compression tests, the uniaxial strain compression test is a displacement controlled experiment. Figure 3-37 shows the typical strain path traversed in a deviatoric strain versus volumetric strain coordinate system.

The measured normal stresses were used to calculate the mean normal stress $p = -(\sigma_z + 2 \cdot \sigma_r)/3$ and the effective deviatoric stress $\tau = abs(\sigma_z - \sigma_r)/\sqrt{3}$. Corresponding to the uniaxial compression strain path, the resulting stress path for this test is shown in Figure 3-38, in an effective deviatoric stress versus mean normal stress coordinate system. Shear stresses and shear strains as well as compressive stresses and volumetric changes occur in this test. Consequently, both the compaction mechanism and the shearing mechanism are active.

The uniaxial constrained compression mean normal stress and effective deviatoric shear stress results, combined with the corresponding calculated values of relative density (c.f. Figure 3-36), can be used to locate a series of points in stress space, defining the position of the yield surface as a function of relative density. Comparison of the uniaxial strain compression and triaxial compression experimental results

for the ANCOR MH-100 yield surface with predictions of the Cam-clay type yield surface can be seen in Figure 3-39. The role of deviatoric stresses on densification can be understood by considering the representative yield surfaces for a particular relative density. The magnitude required to attain a relative density by purely hydrostatic stress is represented graphically by the distance from the origin to the point where the yield surface intersects the mean normal pressure axis. If densification is accomplished by a combination of hydrostatic and shear stresses as in uniaxial constrained compression, the hydrostatic stress required for densification is reduced by the presence of a shear stress.

3.4.4 Conclusion

The uniaxial strain compression test is the easiest test for studying volumetric stress-strain relationships. The uniaxial strain compression system designed, fabricated, and documented by Abou-Chedid is capable of accurately and precisely measuring both the stresses and strains of granular materials. A strain gauged pressure sensor of the type employed in the triaxial compression system was used on the lower compacting surface to measure the lower axial normal stress, while a lateral pressure sensor measured the radial normal stresses. The upper axial stress was calculated from the Instron load cell measurement and the cross-sectional area of the specimen.

ANCOR MH-100 sponge iron powder was tested at initial density $\eta_0 = 0.42$. Sidewall friction was minimized via Teflon spray, and the stresses measured were assumed to be principal. Stress versus strain curves were obtained for the iron powder for pressures up to 450 MPa.

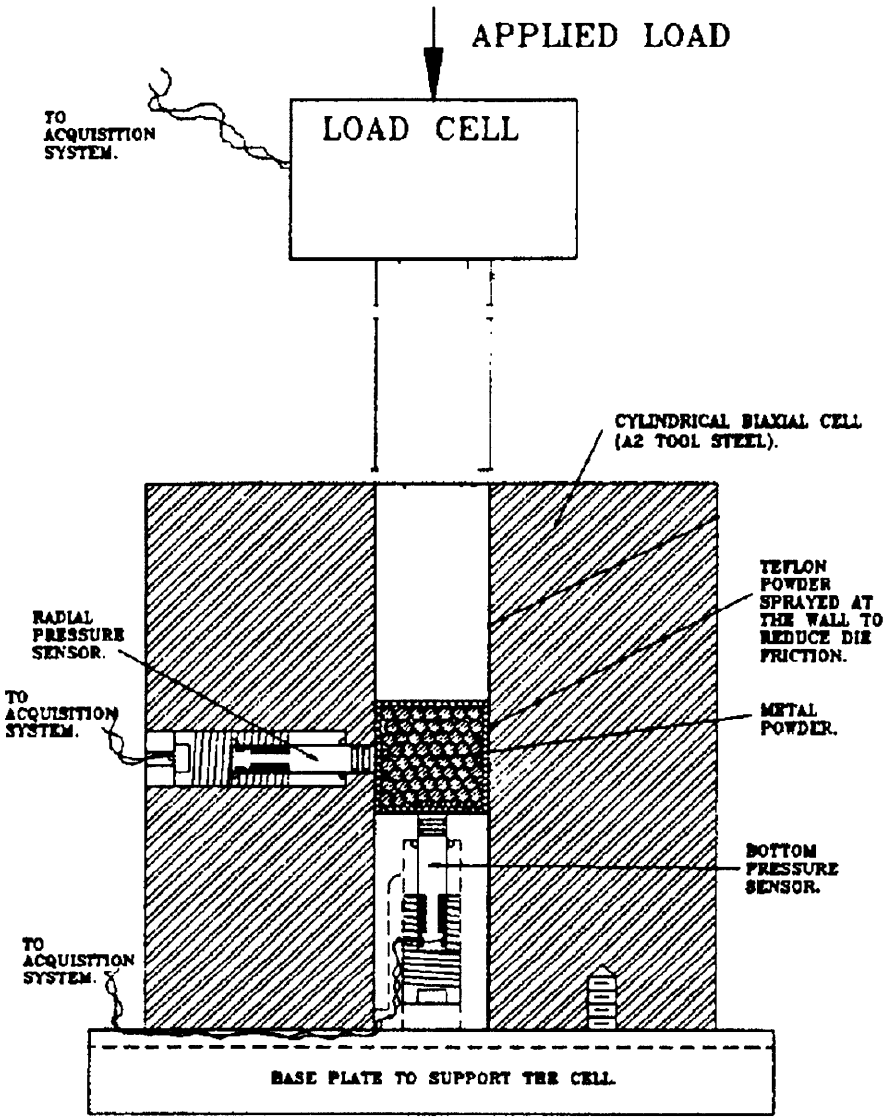

Figure 3-34: Uniaxial strain compression system assembled apparatus, pressure sensors, and specimen. After [34].

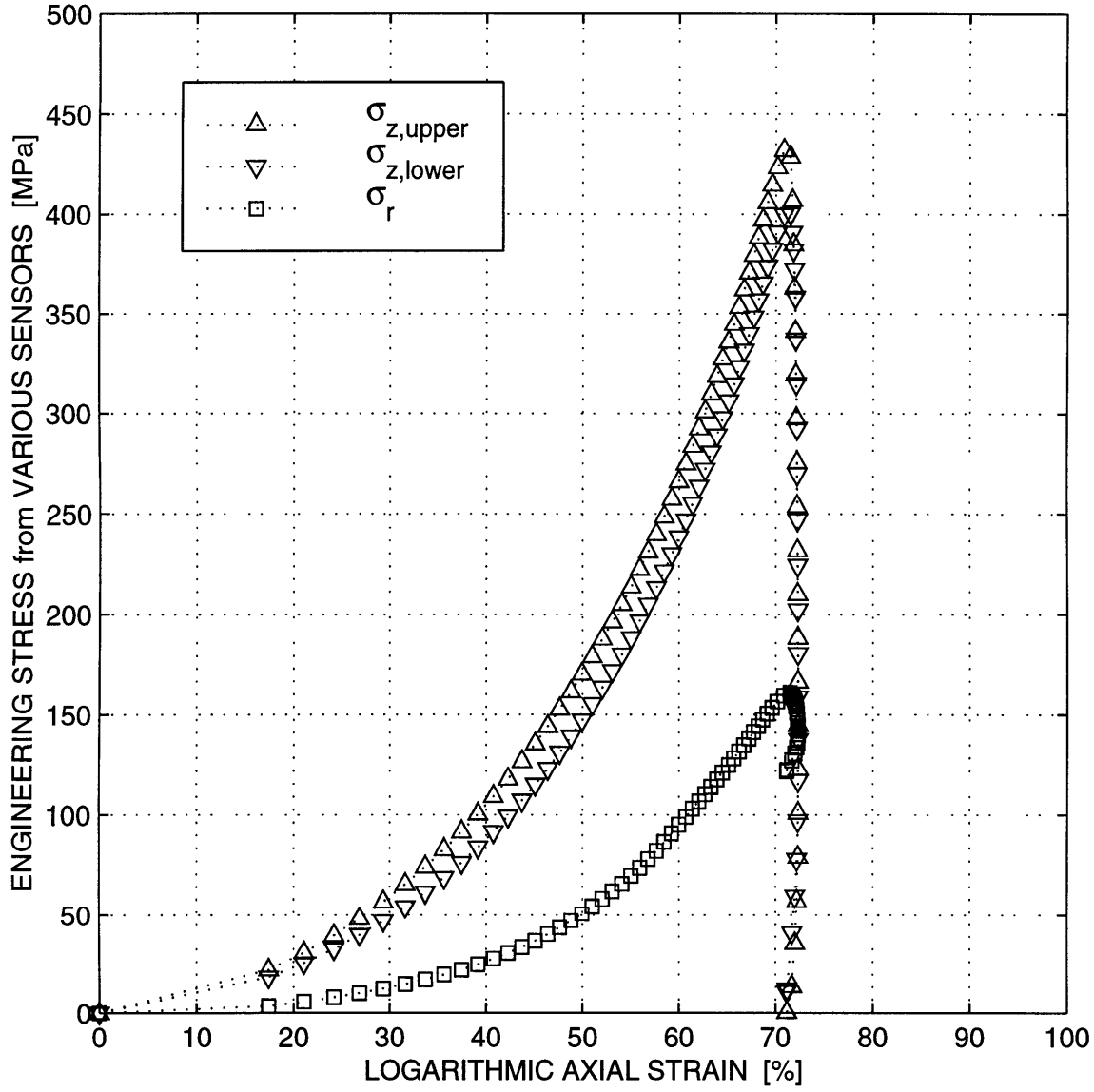

Figure 3-35: Typical loading and unloading axial stress versus axial strain curves for uniaxial strain compression of ANCOR MH-100 iron powder: test U0625E.

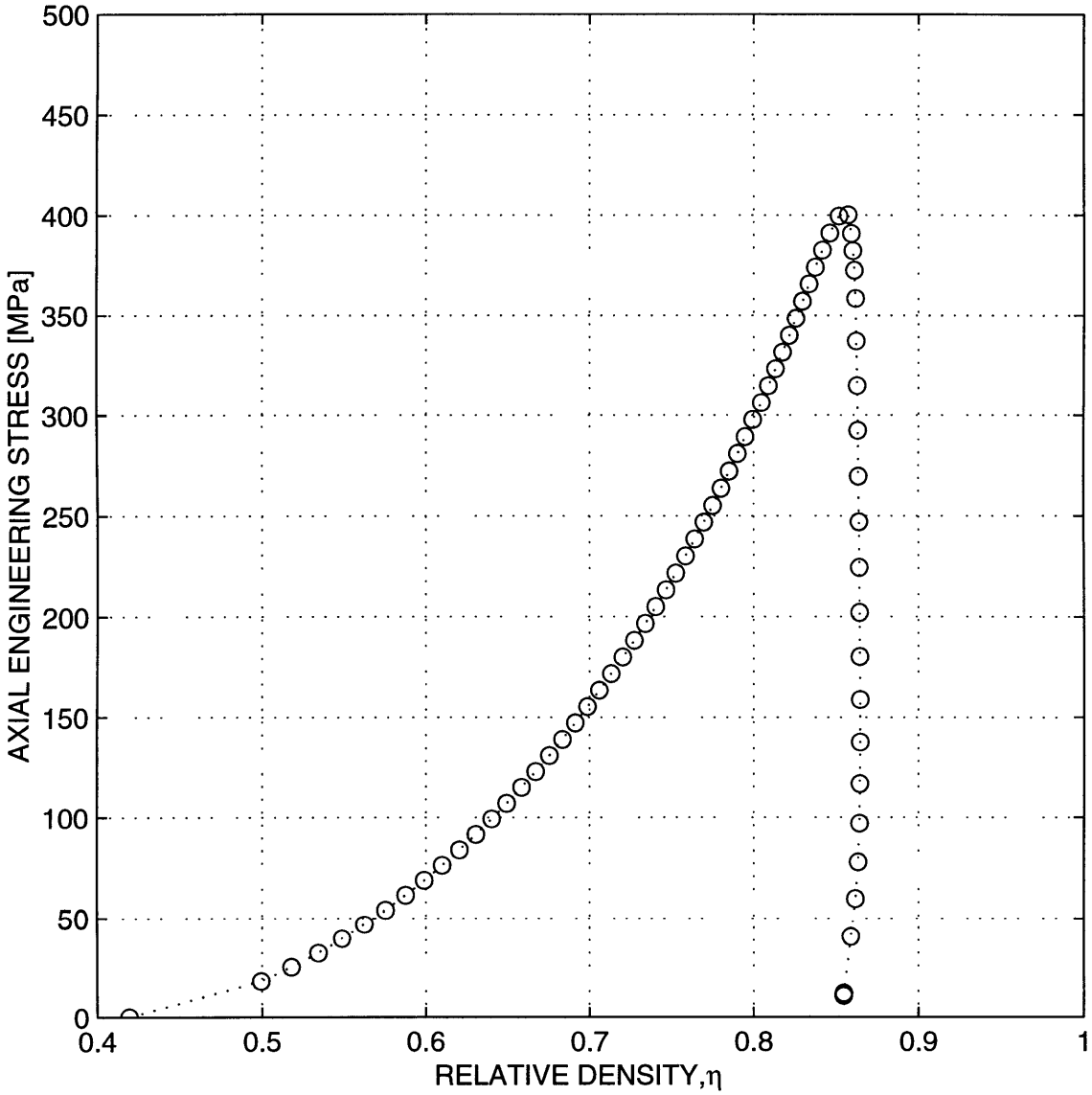

Figure 3-36: Typical axial stress versus density response for uniaxial strain compression of ANCOR MH-100 sponge iron powder: test U0625E.

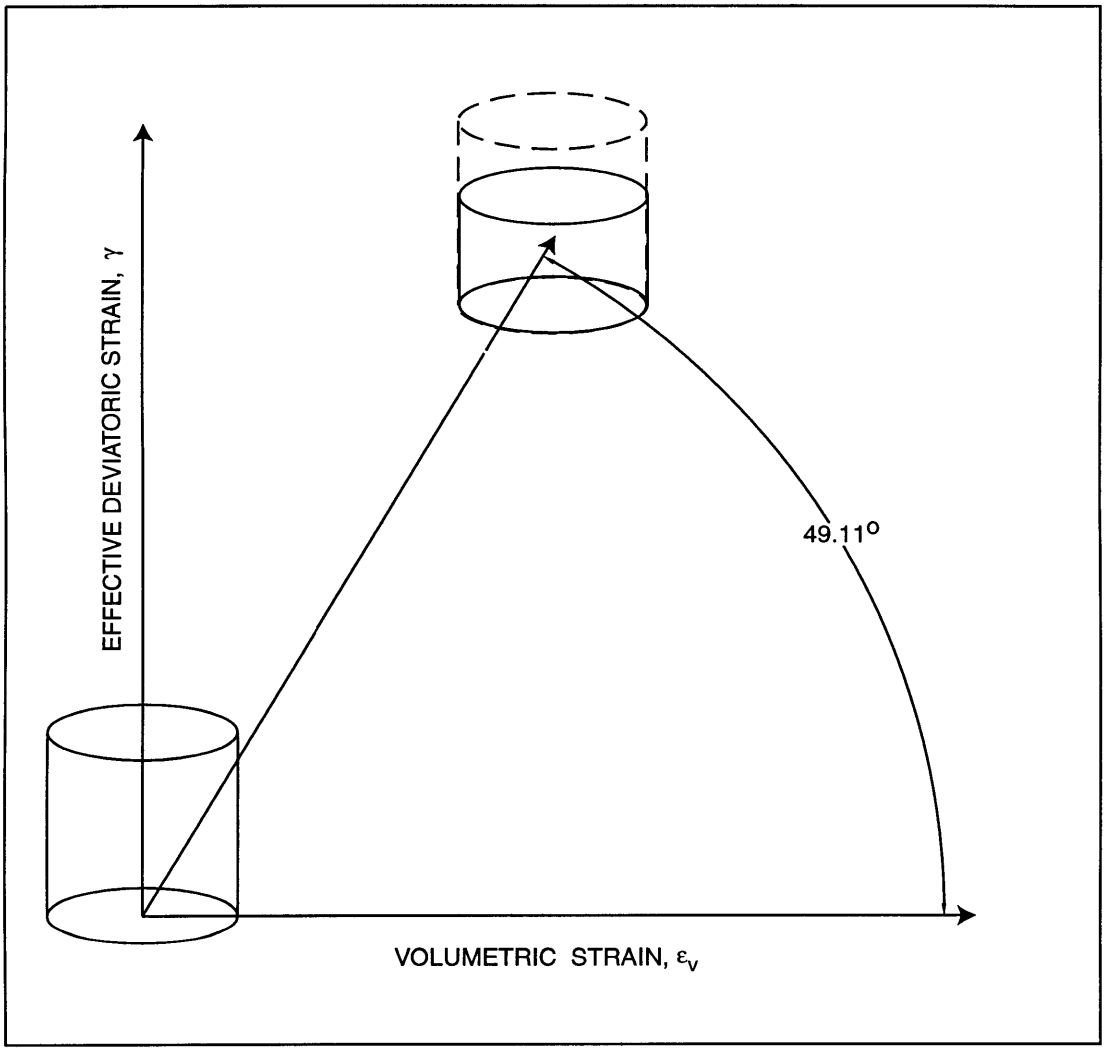

Figure 3-37: Theoretical strain path traversed during uniaxial strain compression test.

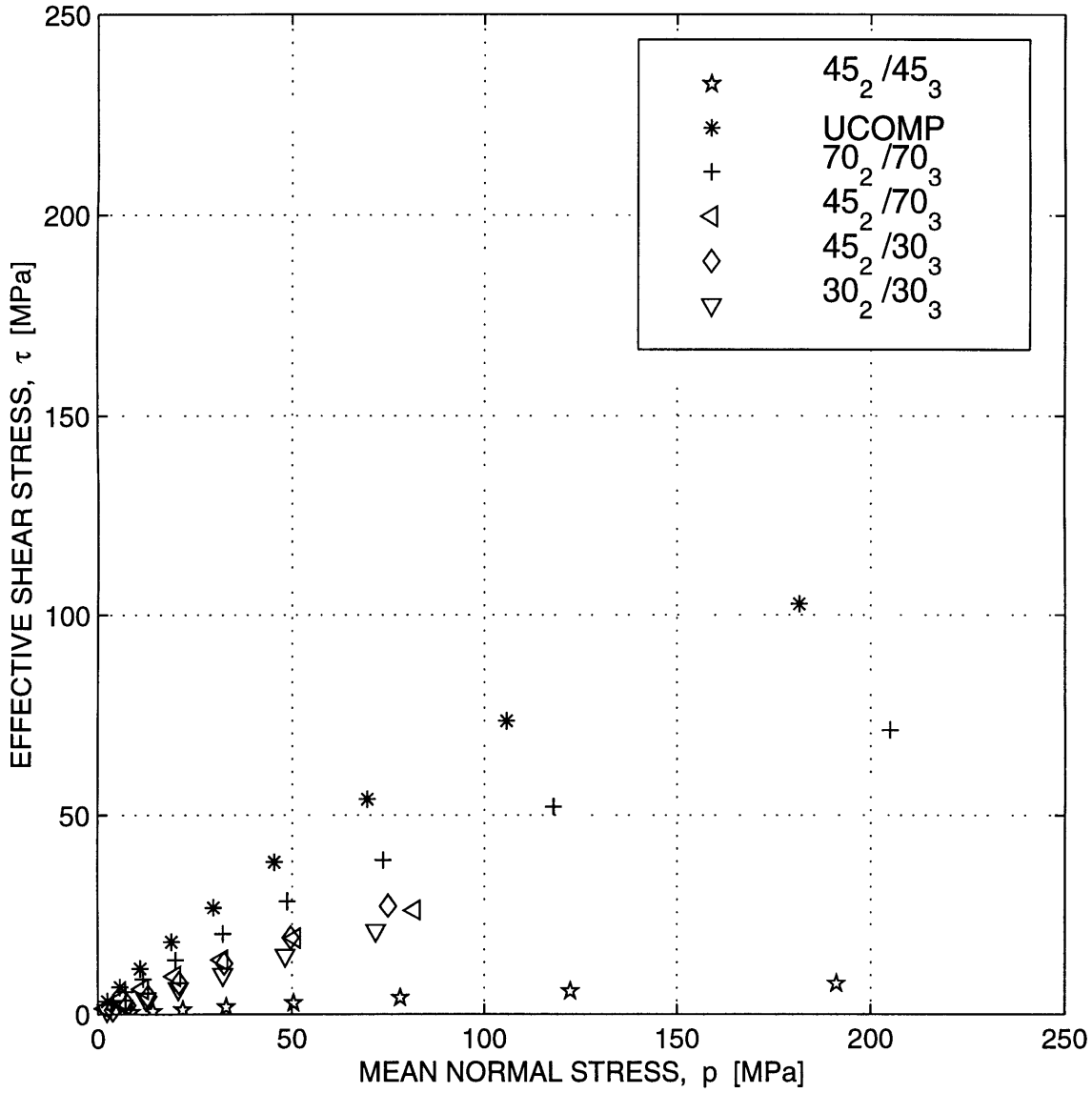

Figure 3-38: Experimentally measured stress paths achieved by uniaxial strain compression and triaxial compression experiments of ANCOR MH-100 iron powder.

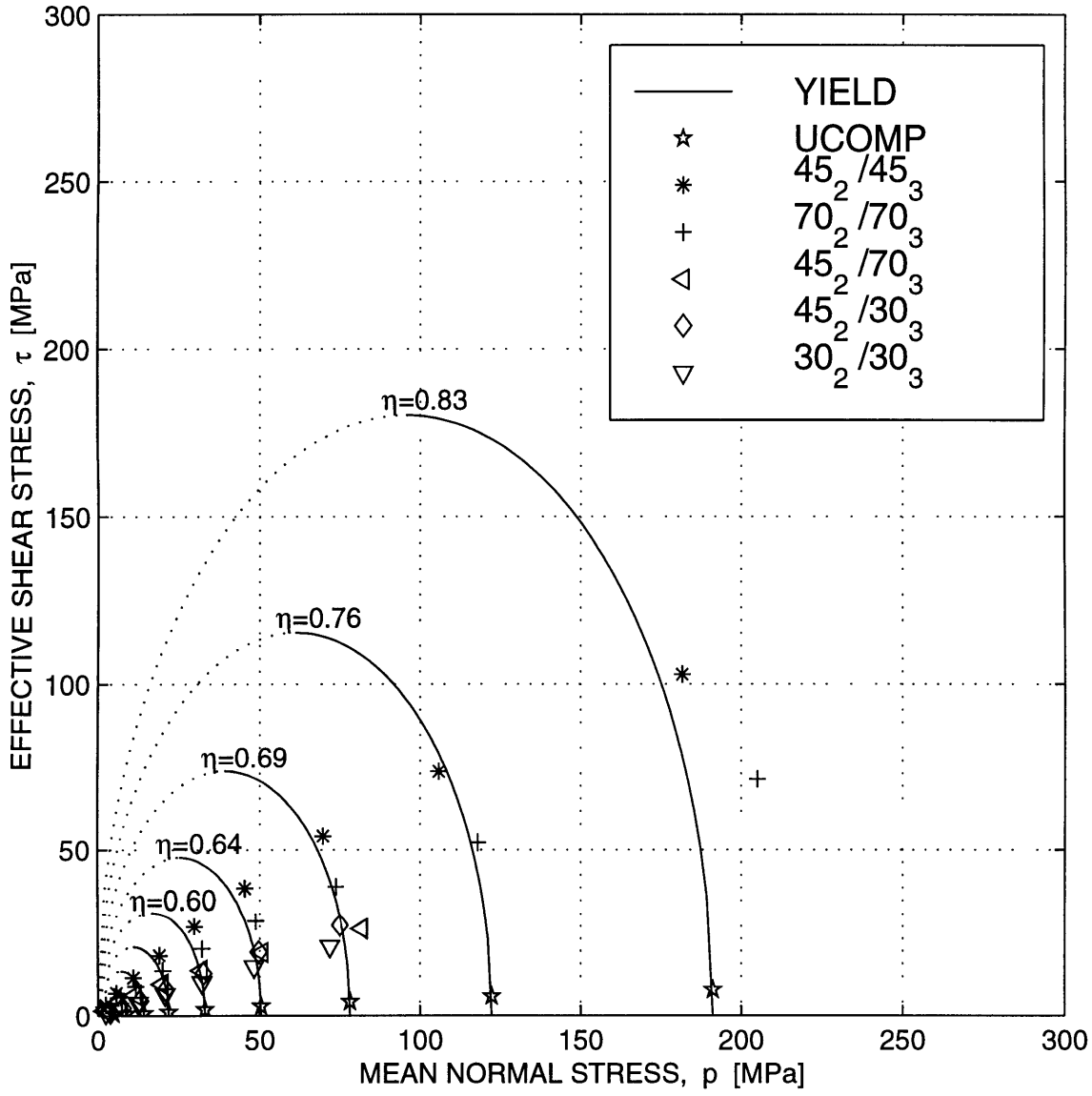

Figure 3-39: Comparison of the experimental results for the ANCOR MH-100 yield surface with predictions of Cam-clay type yield surface.

3.5 Simple Compression

3.5.1 Introduction

The simple compression tests is a convenient, standard means by which to obtain stress-strain information for a material. The role of the simple compression test in the study of the large deformation of metals is well established [ASTM Standard E209-65]. Compression testing achieves large strains due to the absence of necking and permits a fairly simple means of measuring strain by determining the relative displacement of the compression platens. Also it is also easier to perform than torsion shear tests since it requires a simple and more common experimental apparatus and requires less complicated alignment of loading fixtures. Two limitations are (i) lateral buckling and (ii) friction between the compression specimen and compression platen which may create inhomogeneous deformation. These limitations constrain the size and dimensional portion of compression specimens. The maximum length to diameter ratio which will dissuade buckling was determined to be smaller than or equal to 1.5[47].

3.5.2 Experimental Setup

Nominally homogeneous simple compression tests were performed on ANCOR MH-100 samples of height approximately 12.5 mm and diameter 25.4 mm and of different densities, obtained by pre-consolidation in the uniaxial strain system described in Section 3.4. All testing was performed using the uniaxial servo-hydraulic system and data acquisition system described in Section 3.4. The pre-compacted specimen was placed between a pair of six inch diameter main compression platens.

To minimize the barreling due to the friction of the material against the compression platens, the ends were lubricated with Teflon film[10] and Dow Corning G-n lubricant. Teflon film used for all compression testing was in the form of sheets, 0.508 mm thick. Two sheets were used at each of the top and bottom surfaces, giv-

[10]BLH Electronics, Inc. 75 Shawmut Rd. Canton, MA 02021. Tel: 781.821.2000

ing an initial lubricant film thickness of 1.016 mm. The Dow Corning G-n lubricant was spread between the Teflon sheets, and between the specimen and Teflon sheet interface. All compression testing was performed under displacement control, using a constant displacement rate corresponding to an initial engineering strain rate of 0.001 $s^{-}1$. A summary of the detailed experimental procedures used in the testing are included in Appendix B.

Specimen reduction of height was measured externally via short stroke linear potentiometer of 25.4 mm displacement capacity, and a two piece compression displacement fixture. The reasoning behind the redundant displacement sensor (in addition to the Instron crosshead LVDT) was to measure the relative displacement between main platens and eliminate system compliance due to the load frame.

3.5.3 Results and Conclusions

MH-100 green compacts formed in the uniaxial strain compaction apparatus were compressed in a state of uniaxial stress. Due to the highly irregular morphology of the iron particles, the iron samples exhibited significant strength during simple compression even at relative densities as low as $\eta = 60.4\%$. The maximum relative density was achieved was $\eta = 85.0\%$.

The appearance of the sheared specimens after being extruded from the uniaxial strain compression apparatus was striking. The specimens extruded as solid cylinders and visually appear as solid iron (Figure 3-40, right specimen). The outer layer of the iron powder adjacent to the cell wall exhibited signs of being so heavily sheared that there did not appear to be any observable aggregate structure. The green compact appeared to be solid iron. The powdered lubricant used in these tests appeared as a thin layer of white Teflon within the heavily sheared outer layer of the uniaxially strained specimen.

Throughout the rest of the specimen, as seen after failure in simple compression (Figure 3-41), there is a definable individual particulate structure, though heavily crushed and compressed. The micrograph demonstrates the different forms of behavior when a powdered metal undergoes large amounts of compression. From its

original condition shown in Figure 3-1, Figure 3-42 shows at greater magnification how the soft MH-100 grains exhibit highly plastic behavior during compression.

Figure 3-43 shows engineering stress versus true strain results from the simple compression for five green compacts with differing initial relative densities. Each stress strain curve represents the three stages of compaction. The beginning of the stress-strain curve is unusual during the simple compression of pre-compacted granular materials. This phenomenon may be attributable to the closing of microcracks created during the preparation of the sample by uniaxial strain compaction, perhaps during the ejection from the die. The relative length of the third stage increases with increasing relative density. Abou-Chedid [34] attributed the increasing length of the third stage to the increasing importance of the plastic deformation of particles over the detachment mechanism of inter-particle cohesion at lower densities.

The yield point from the simple compression test is evaluated using the convention in solid metals of fitting a line through the second stage of the stress strain curve and then employing a 0.2% offset criteria. The evolution of the yield stress as a function of the density of the green compact is plotted in Figure 3-44. For comparison purposes, we have also included the experimental yield data published by Brown and Weber [33] in Figure 3-44. The experimental results of the oxide covered ANCOR MH-100 simple compression tests are in reasonable agreement with the data of Brown and Weber and the yield strength is seen to increase with increasing relative density. The significantly different yield behavior of the sintered ANCOR MH-100 iron powder can also be seen in this figure.

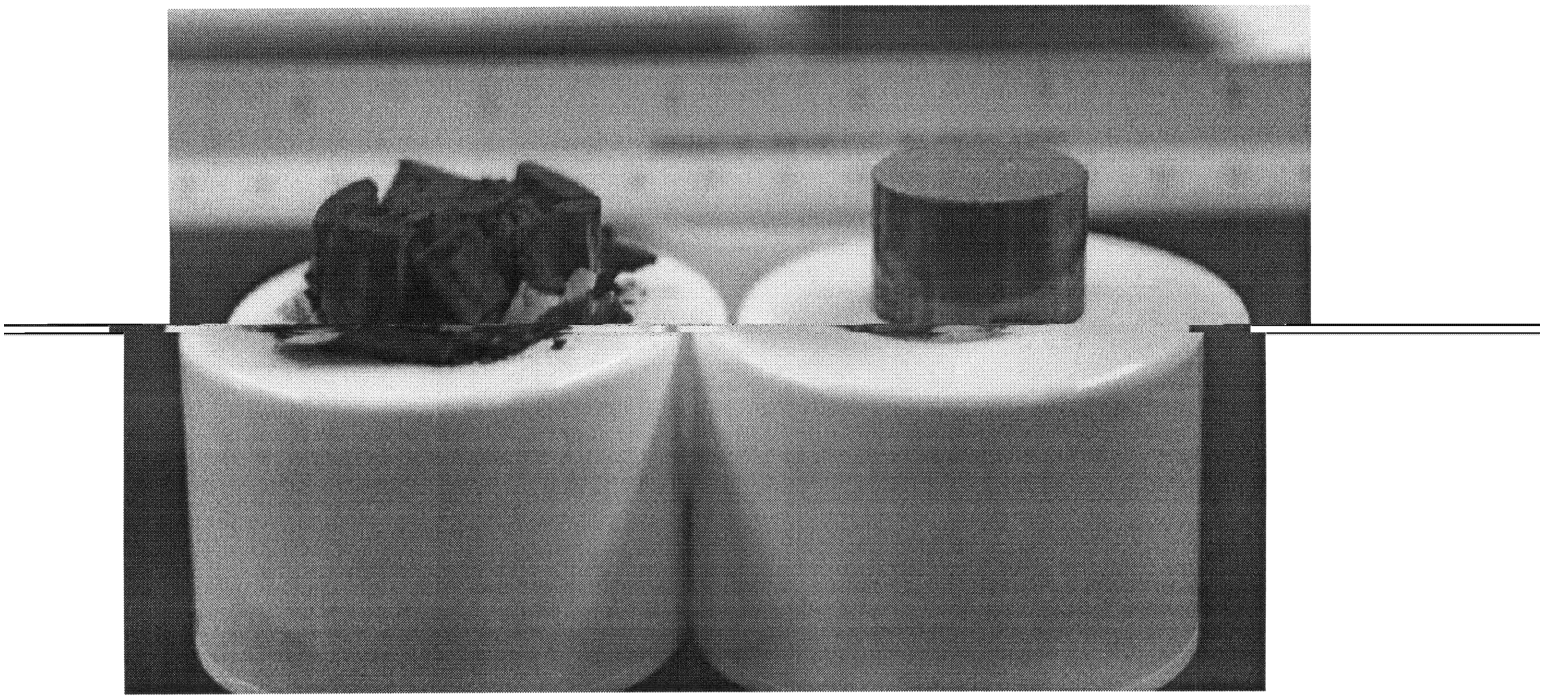

Figure 3-40: ANCOR MH-100 specimen after failing in simple compression (left); the original uniaxial strain compression specimen is on the right.

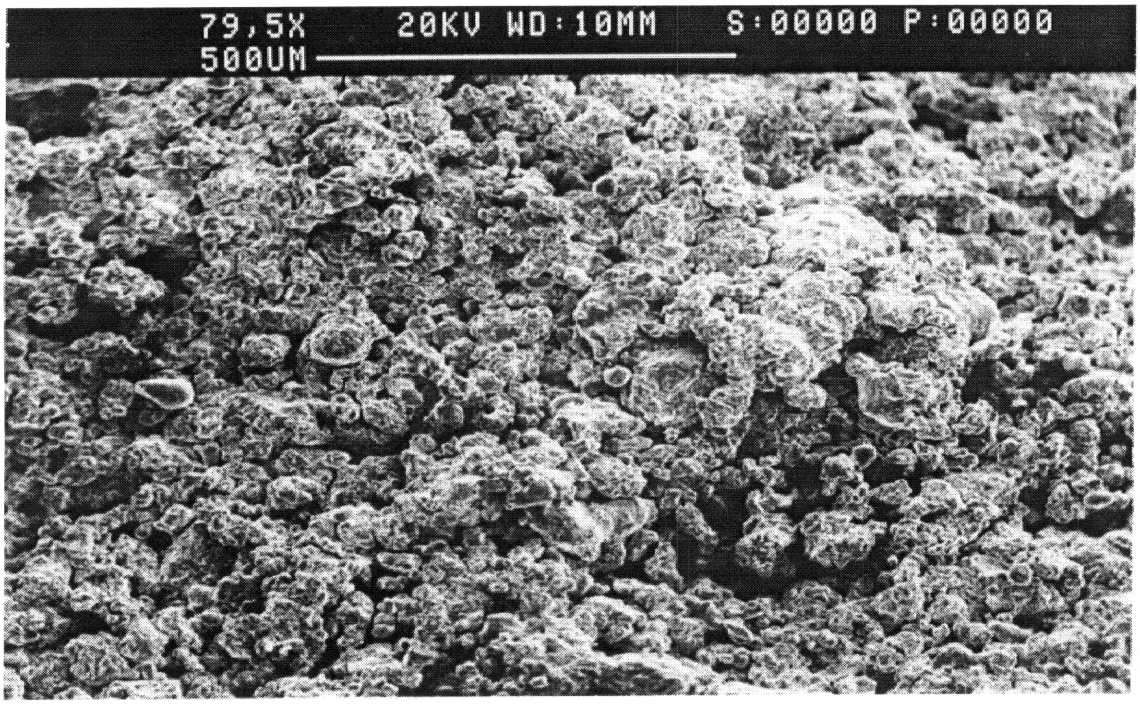

Figure 3-41: SEM Micrograph 500 micrometers.

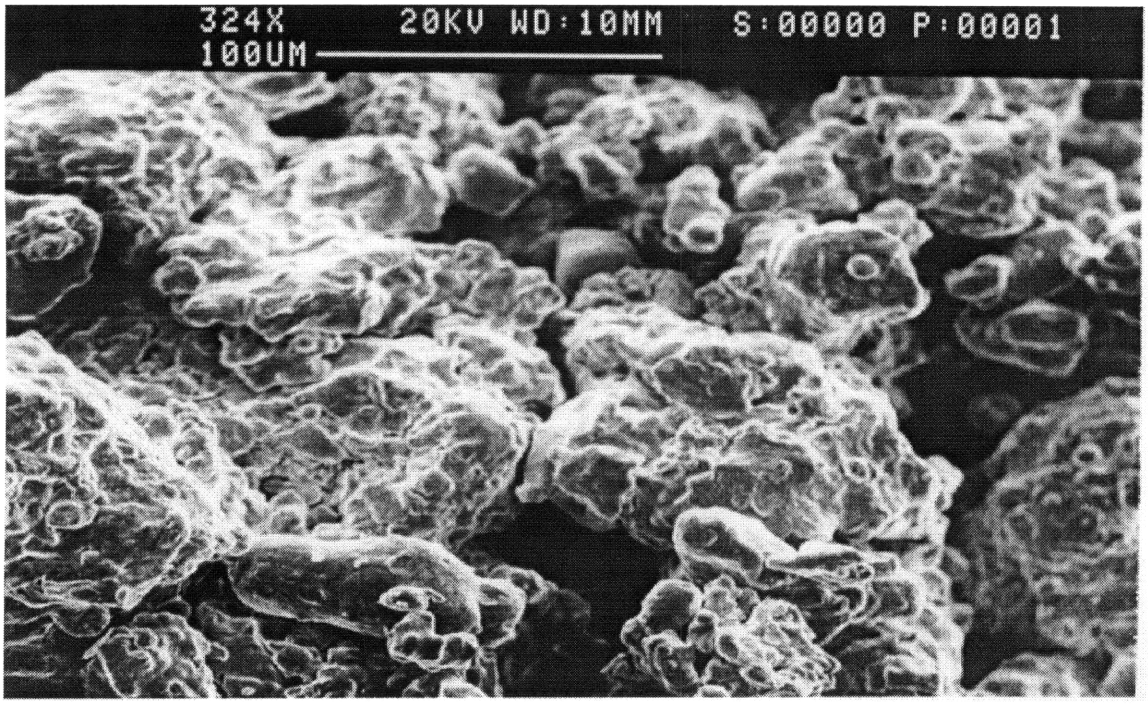

Figure 3-42: SEM of two particles plastically deforming.

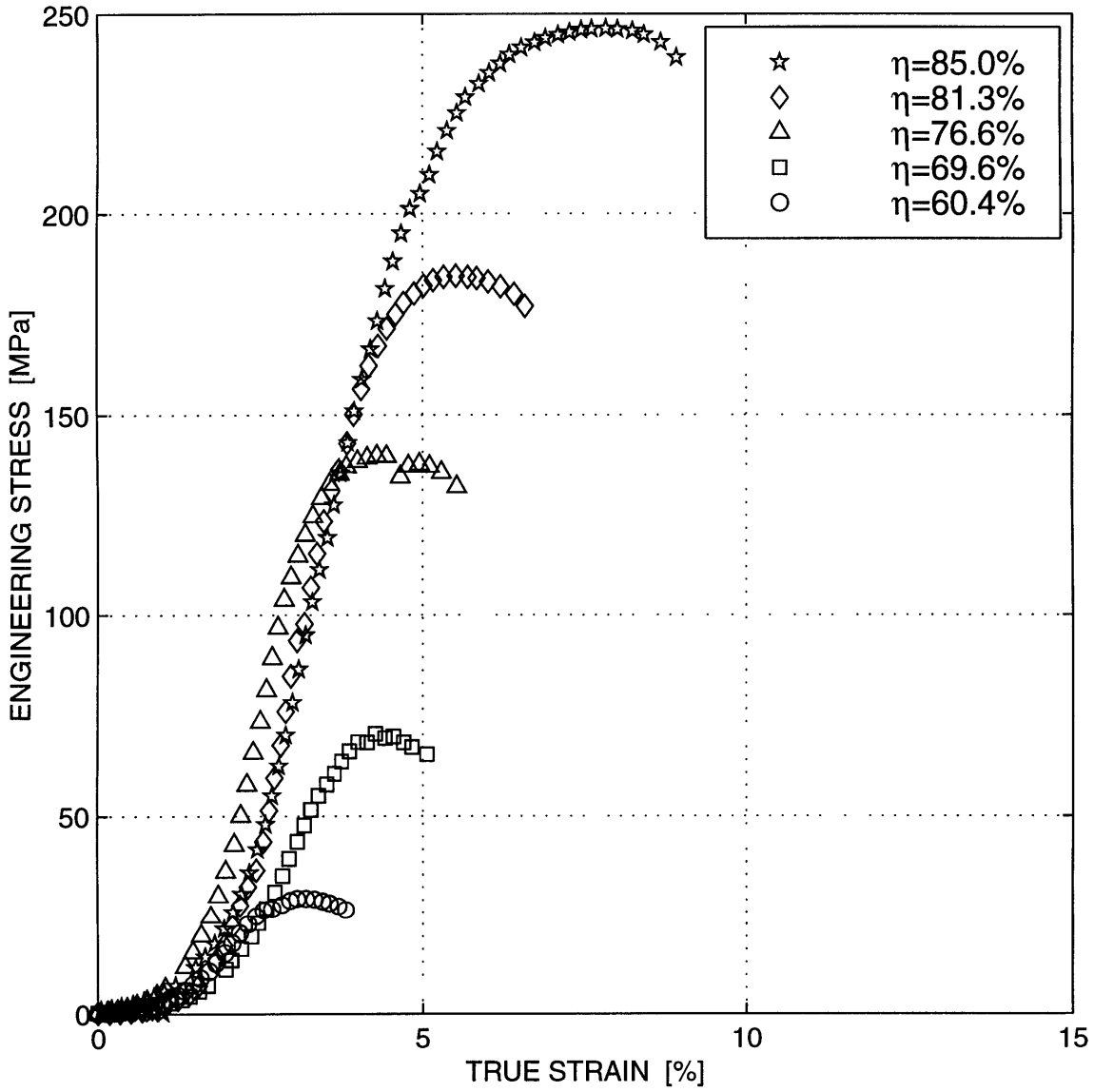

Figure 3-43: Engineering stress versus true strain curves for irregularly shaped MH-100 iron powder loaded in simple compression: test S0625.

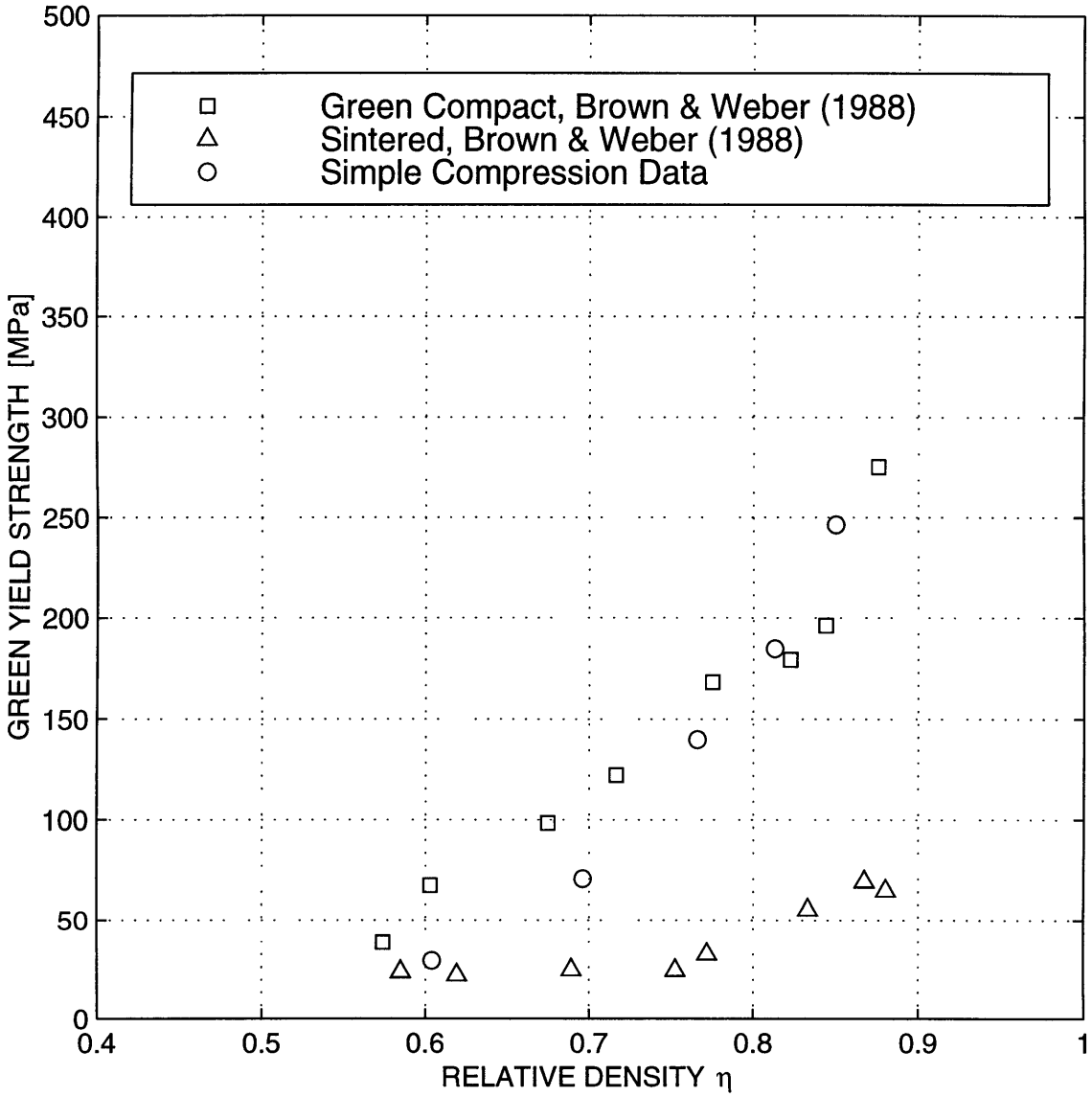

Figure 3-44: Evolution of green compact yield strength, including data by Brown and Weber [33], with relative density for irregularly shaped MH-100 iron powder.

Chapter 4

Conclusion

Existing porous plasticity models are inappropriate for the modeling of cold compacted metal powders. To investigate the yield characteristics and frictional behavior of ANCOR MH-100 iron powder, the following experiments were performed:

- Triaxial compression experiments covering much of the high stress triaxiality region have been conducted on sponge iron powder. Comparison of these results against corresponding predictions from a portion of the modified Cam-clay model shows the model to be reasonably accurate.

- A torsion ring shear apparatus was designed and fabricated to investigate the shearing behavior of iron powders at large deformations as well as the important interface friction between the iron powders and confining dies. The results of this new apparatus are qualitatively consistent with similar torsion ring shear experiments done on clays at lower normal pressures.

- Uniaxial strain compression tests were conducted in which shear stresses and shear strains as well as compressive stresses and volumetric changes occur in the iron powder specimen. Consequently, both the compaction mechanism and the double shear mechanism were active in the uniaxial strain compression test.

- Simple compression tests were conducted on the extruded uniaxial strain compression specimens. The yield data indicate that the yield surface of the irregu-

larly shaped ANCOR MH-100 iron powder may be dependent on inter-particle cohesion as well as relative density. It was concluded that the portion of the Cam-clay model used to model the compaction yielding behavior of ANCOR MH-100 iron powder was inadequate for predicting the shearing yield behavior.

In light of these experimental results, a more sophisticated multi-mechanism yield surface, such as a Cam-clay consolidation yield surface in conjunction with a Mohr-Coulomb shearing yield mechanism, is necessary to model the complete yielding behavior of ANCOR MH-100 iron powder.

4.0.4 Suggestions for Future Research

Following are some areas for future research:

- Confined triaxial tests of pre-consolidated specimens and loose powder are needed to verify the torsion ring shear results and to investigate the shearing yield mechanism more thoroughly. Such a device is available in the Geotechnical measurements lab with a 10 MPa capacity confining pressure. The shearing yield surface could be experimentally probed using this confined triaxial apparatus and the evolution of cohesion with relative density could be accurately determined.

- Further torsion ring shear tests are needed to determine the shearing behavior of ANCOR MH-100 iron powder. Tests could also be performed to investigate the magnitude of change in shearing resistance accompanying a reversal in the direction of movement on the plane of failure.

Appendix A

Calibration Curves

A.1 Pressure Sensor Calibration Curves

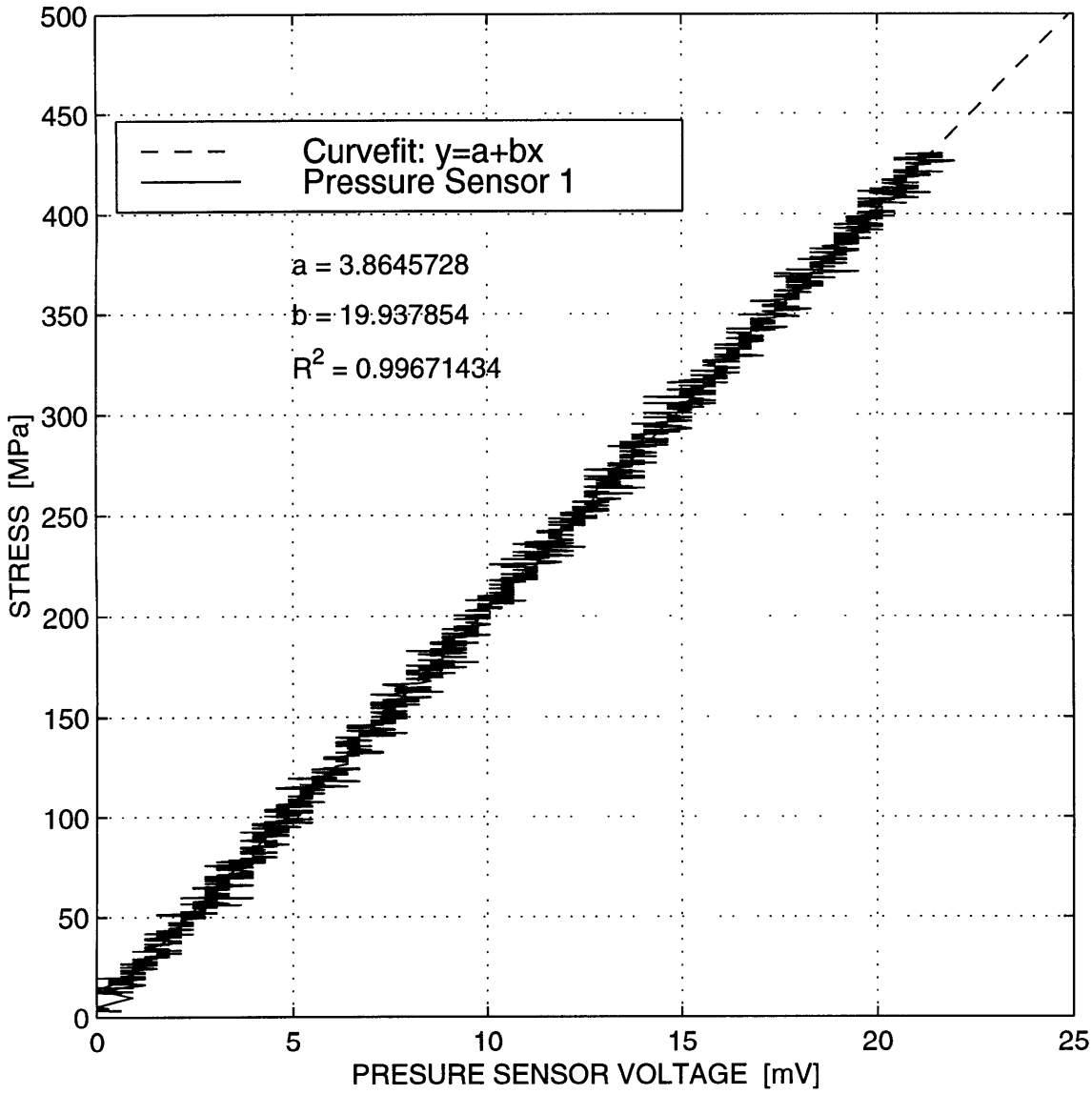

Figure A-1: Pressure Sensor 1 Calibration Curve

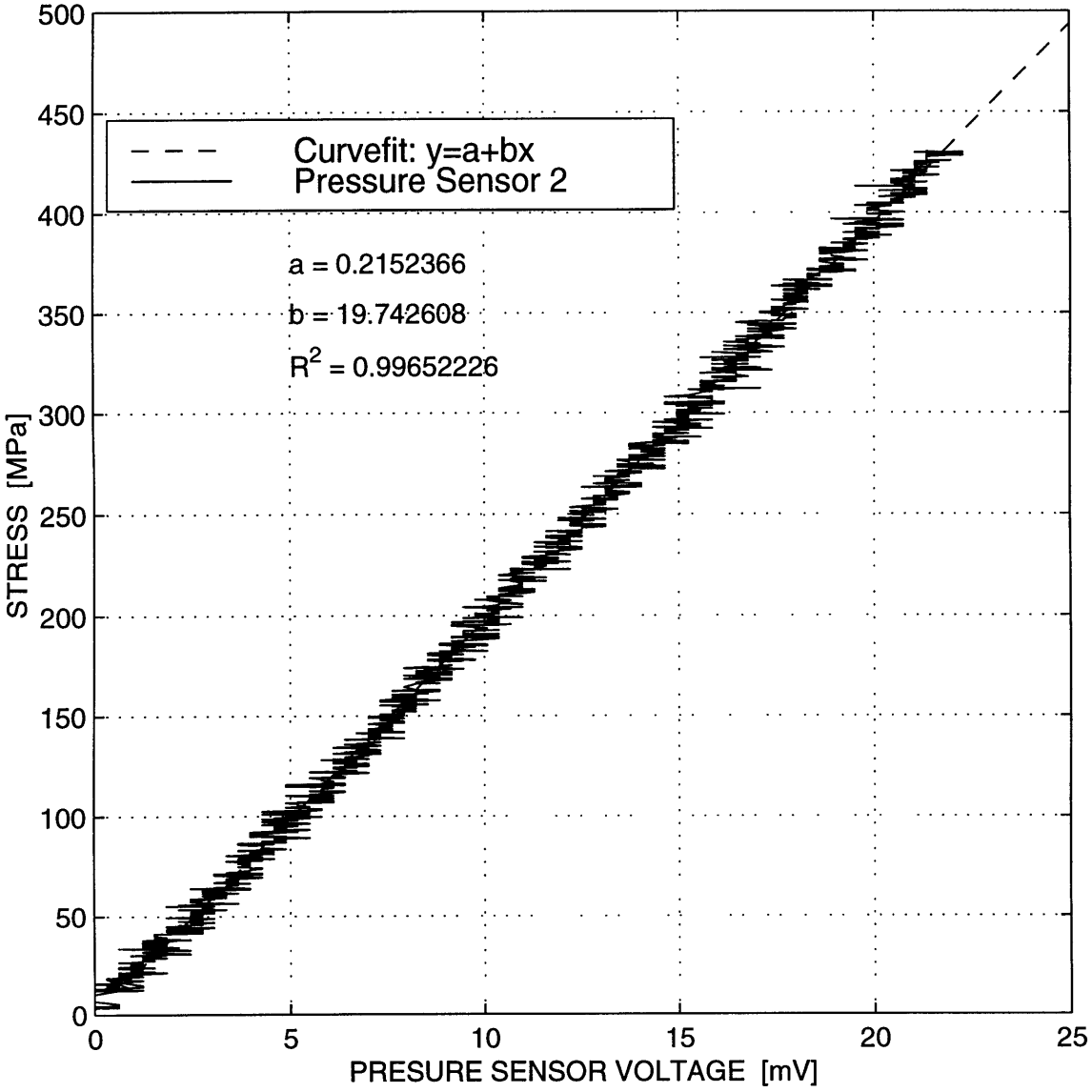

Figure A-2: Pressure Sensor 2 Calibration Curve

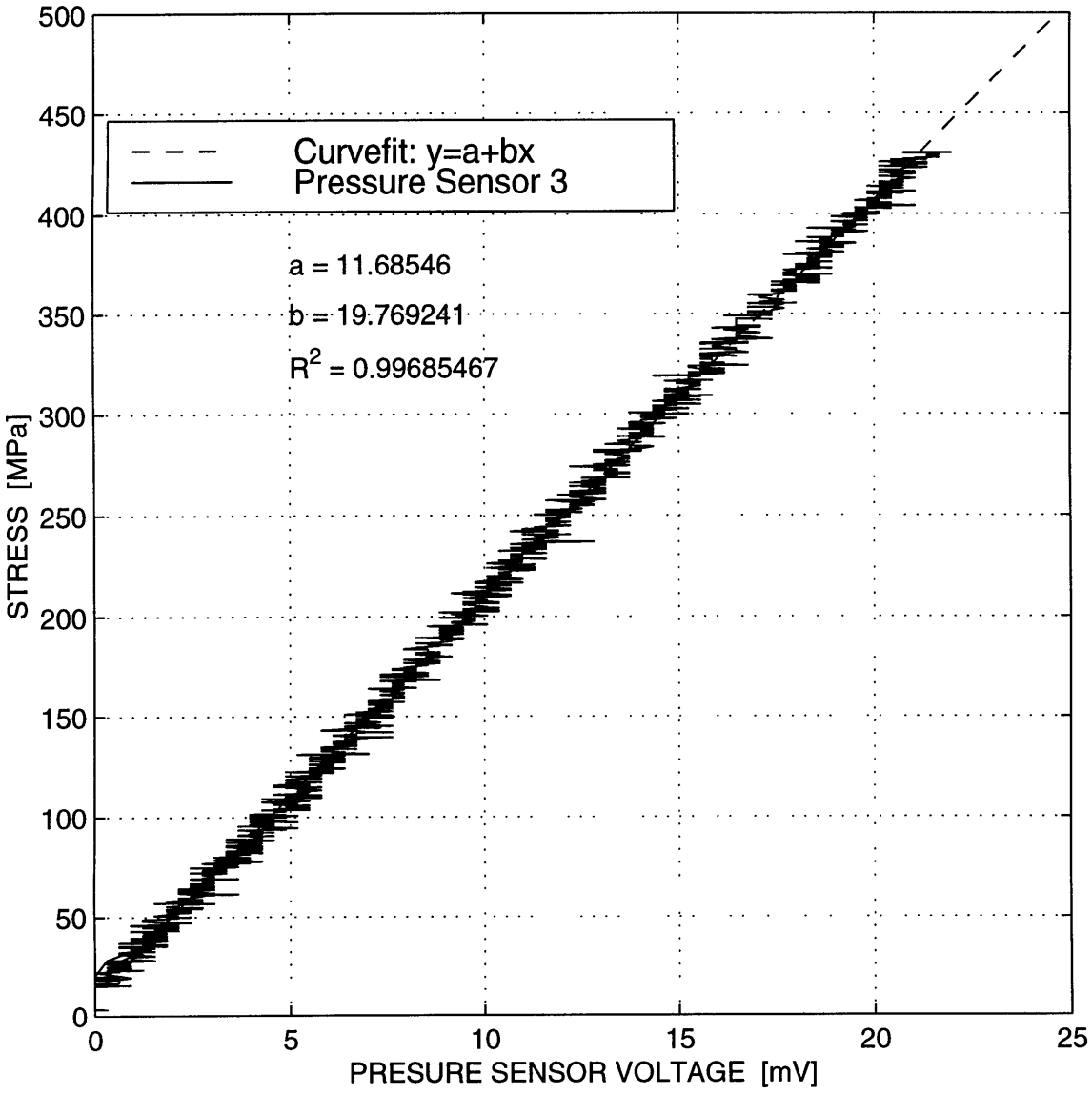

Figure A-3: Pressure Sensor 3 Calibration Curve

A.2 Displacement Sensor Calibration Curves

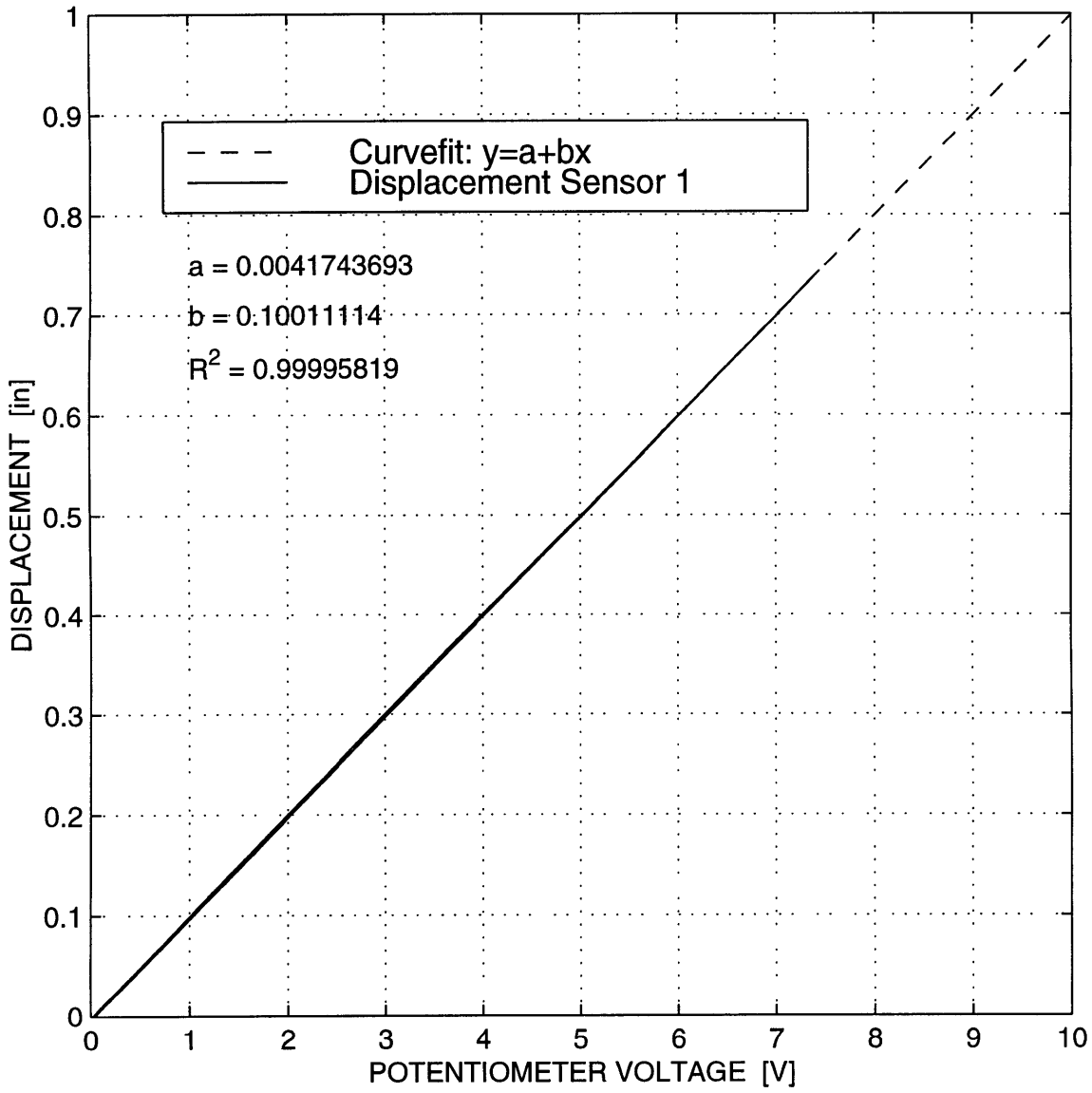

Figure A-4: Displacement Sensor 1 Calibration Curve

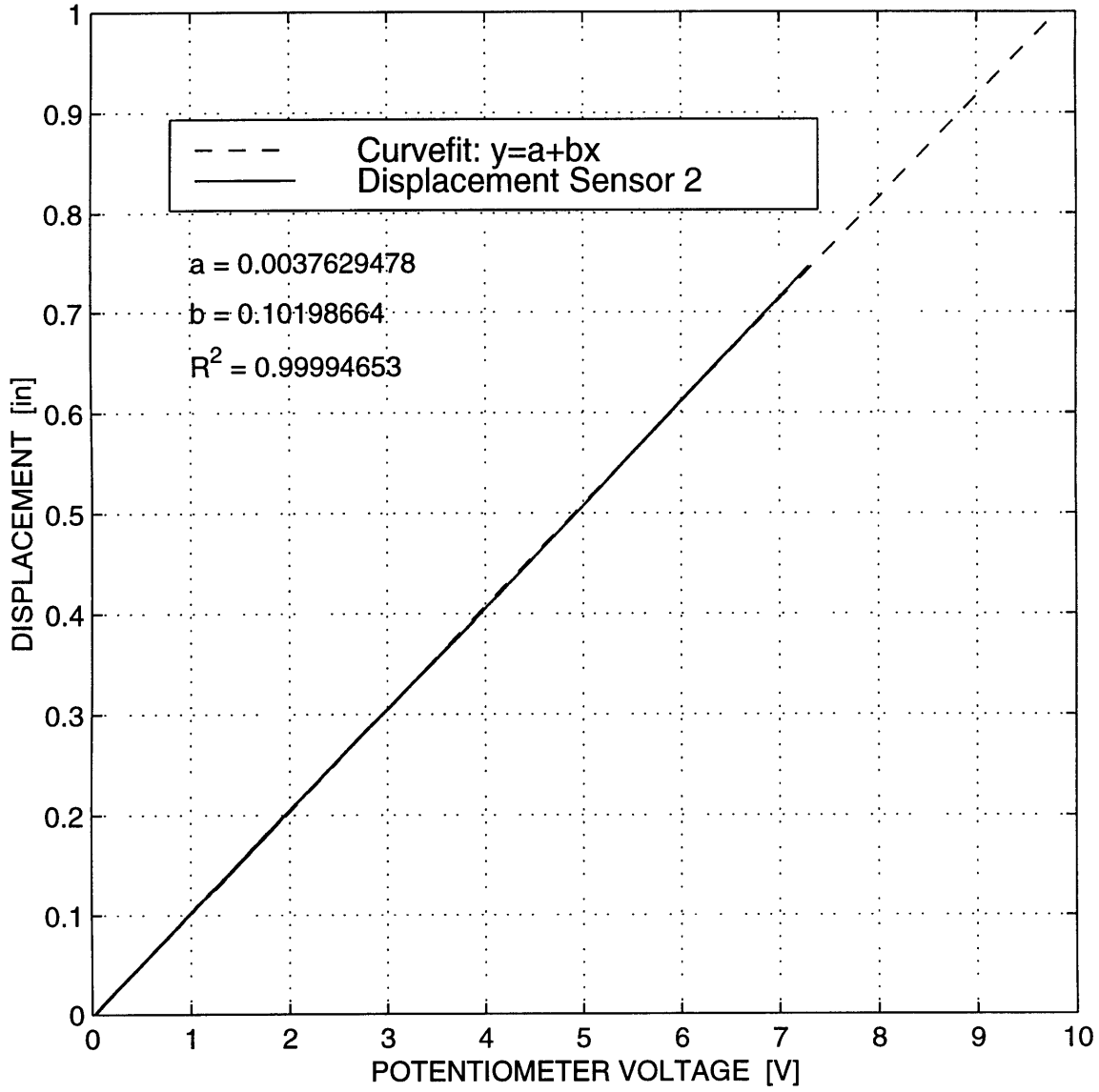

Figure A-5: Displacement Sensor 2 Calibration Curve

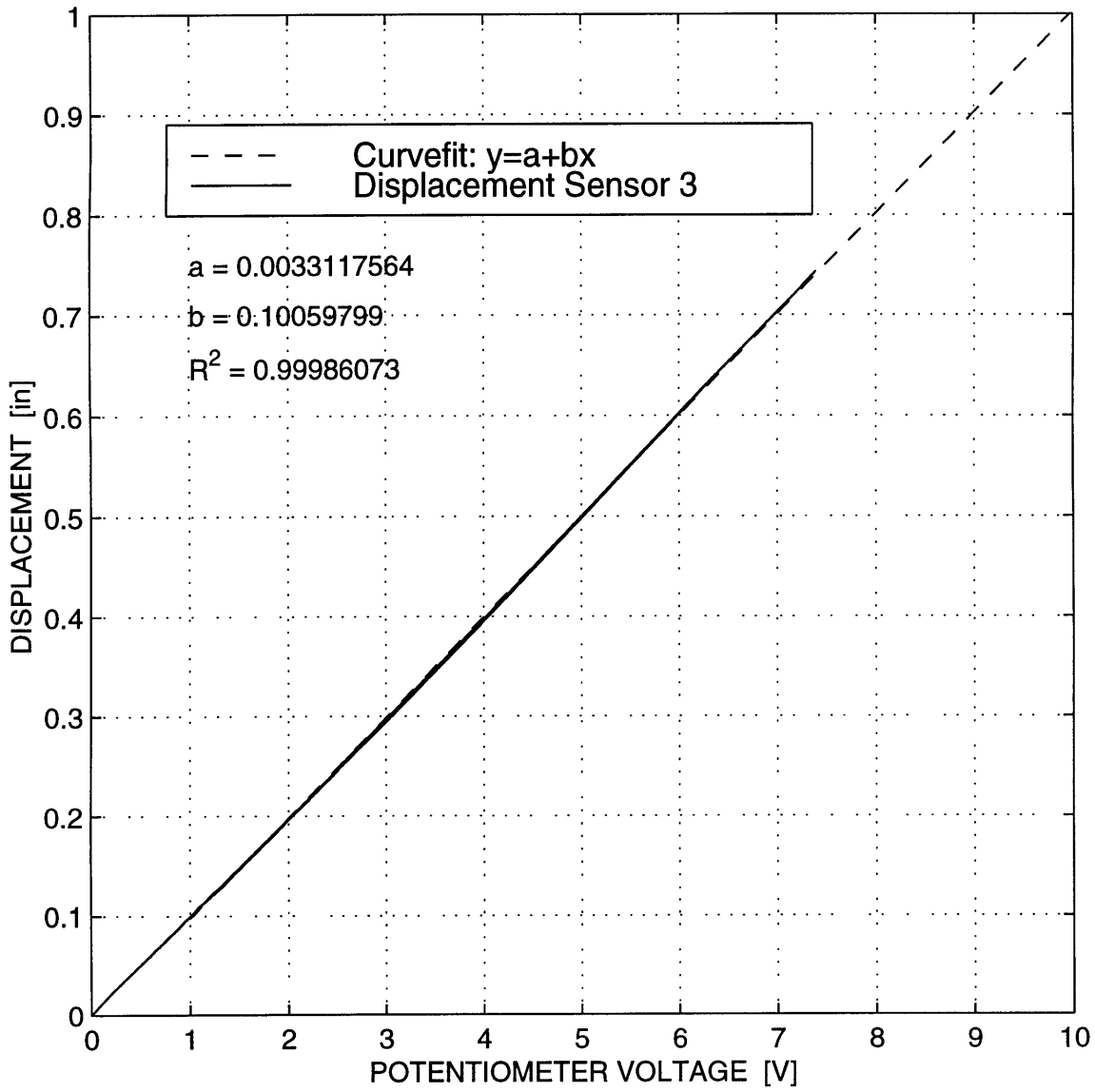

Figure A-6: Displacement Sensor 3 Calibration Curve

A.3 Uniaxial Strain System Compliance Curve

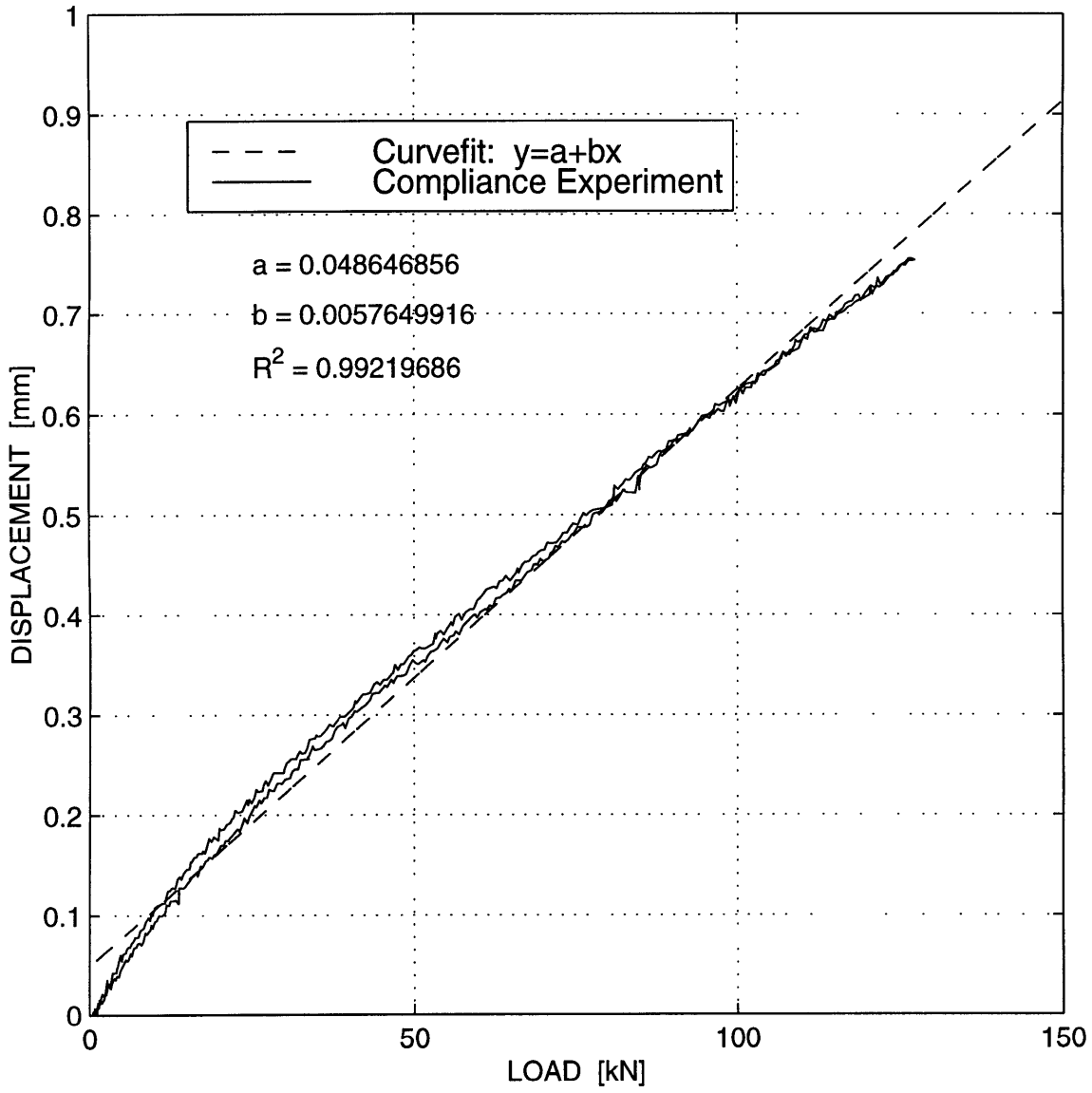

Figure A-7: Uniaxial Strain System Compliance Displacement Correction Curve

Appendix B

Detailed Experimental Procedures

B.1 Triaxial Compaction Test Procedure

This section gives comprehensive documentation of the developed testing procedures utilized to assemble the triaxial compression system, and to perform a high pressure triaxial compression test.

1. Make sure that the frame is free of debris which could lead to misalignment. (C.f. Figure 3-5 for nomenclature of various triaxial compression system components.) First, carefully install the strain gauged pressure sensors in pressure sensor block (DIR 1), pressure sensor block (DIR 2), and pressure sensor block (DIR 3) so that the pressure sensing face of each strain gauged pin is perfectly flush with the face of the corresponding pressure sensor block.

2. Once the empty frame is situated in the desired load system, insert base pressure sensor block (DIR 1) such that the sides are parallel to the walls of the frame. Note the empty frame weighs in excess of 300 lbs and should only be carefully transported with appropriate help.

3. Insert the two inverted L-shaped blocks so that they touch the long faces of the base pressure sensor block (DIR 1). It is important that the springs attached to the inverted L-shaped blocks are normal to the base pressure sensor block (DIR 1).

4. Insert the desired base angled blocks. It is opportune at this point to generously coat the angled block surface with Teflon spray. This will help to minimize the

friction between the angled block and angled loading blocks. Although the accuracy of the local pressure measurements are not affected by application of the Teflon, minimization of friction will promote smoother sliding, less noisy displacement data, and preserve the machined surface from score marks.

5. Insert the square pressure sensor block (DIR 2) flush against the face of the inverted L-shaped block set against the frame wall in the positive 2 direction in Step 3. Insert the rectangular pressure sensor block (DIR 3) flush against the face of the inverted L-shaped block set against the frame wall in the positive 3 direction also in Step 3.

6. Note that each base angled block has exactly one matching angled loading block. In a symmetric loading configuration where both angled blocks have the same angle of inclination, the shorter block will always be angled loading block (DIR 2). First insert angled loading block (DIR 2) on the matching base angled block, so that it is flush against the base pressure sensor block (DIR 1) and flush against the adjoining pressure sensor block (DIR 3). Next, insert the angled loading block (DIR 3) on the matching base angled block, so that it too is flush against the base pressure sensor block (DIR 1) and flush against the adjoining pressure sensor block (DIR 2).

7. If steps 1-6 were completed correctly, the assembled triaxial compression apparatus should look similar to the plan view depicted in Figure 3-5. No powder should be able to egress the die cavity. If the blocks have been satisfactorily aligned, the displacement sensors should be attached via an adhesive (e.g. super glue) to measure the motion in the positive 2 direction of angled loading block (DIR 3) and the motion in the positive 3 direction of pressure sensor block (DIR 2).

8. Spray a thin and even coating of vinyl spray in the die cavity to provide a seal to prevent granular material from escaping. Wait several minutes until the spray dries completely before continuing to the next step.

9. Liberally coat the vinyl pouch inside the die cavity with Teflon spray. This will help to minimize friction between the compacted powder and the vinyl coating/block boundary. Once the teflon has dried, pluviate the granular material at a constant height. The rate at which the granular material is rained into the sieve can be

controlled by adjusting the diameter of the pluviation funnel. If this step is performed with great care, the initial density should be precisely repeatable.

10. Once the die cavity has overflowed with the granular material, level top surface of granular material with scraper so it is even with the top faces of the angled loading blocks. Do not compress the powder in the cavity since this will change the initial relative density achieved via pluviation. If the granular material is ferromagnetic, a non-metallic scraping device is desirable. Thoroughly clean the area of any excess powder so that the top loading block can sit flush against the top faces of the angled loading blocks.

11. Coat the bottom of the top loading block with Teflon powder to minimize friction on the surface of the granular material and any contacting loading blocks. Attach a displacement sensor to the top loading block via super glue such that the tip of the sensor rests normal to a stationary surface such as pressure sensor block (DIR 3). Gingerly, place top loading block over the die cavity so that the side of the tab is parallel to angled loading block (DIR 2) and angled loading block (DIR 1).

12. Load the upper surface of the top loading block following the directions of the particular loading system employed. Begin the KEITHLEY/LABTECH data acquisition system (Setup file: MK_TRIAX) when conducting the experiment.

13. During the test, monitor the pressure and displacement output to ensure the limits of the sensors are not exceeded, and to verify that an expected displacement ratio is achieved. After the test, take off the top loading block and remove the compacted specimen. Record final mass and dimensions on a data sheet.

14. Brush the apparatus clean, wipe with acetone, and store with a light coating of WD-40 to prevent rusting.

B.2 Torsion Ring Shear Test Procedure

The experimental procedure for the torsion ring shear test, and it involves the following steps:

1. Assemble the torsion ring shear system. Insert the upper annular platen to the upper grip, the lower annular platen to the turntable, and tighten all set screws with a torque wrench to 125 N-m. Attach the lower grip to the turntable and fasten all set screws with a torque wrench to 125 N-m. Grip the upper grip and lower grip in the upper and lower MTS hydraulic gripping system, respectively.

2. With the Instron load protect activated to a threshold of 100 lbf, touch the lower platen to the upper platen and record the position of this zero height point. Using this value as the LABTECH displacement offset allows the recorded displacements to correspond to the height of the specimen. Separate the two loading platens and disengage the load protection feature.

3. Liberally coat the inside of the outer confinement cylinder and the exterior of the inner confinement cylinder with Teflon spray. Note the inner confinement cylinder is a Torrington thrust washer.

4. Insert the three Torrington thrust bearings for the outer confinement cylinder, inner confinement cylinder, and center cap.

5. Insert the outer confinement cylinder. Insert the center cap and inner confinement cylinder. Insert as many Torrington thrust washers as necessary to achieve the sample height desired. Thrust washers located below the top of the knurled lower platen may be laterally wrapped in Teflon tape to minimize leakage of granular material at the base of the inner confinement ring.

6. Fill the annular die cavity with granular material and tampen the surface level.

7. Calibrate the axial force and torque loading system so that no force is imposed on the load measuring transducers. Set the load range, displacement range, torque range, and rotation range of the Instron testing machine so that the maximum expected values are at least two thirds of the ranges selected.

8. Calculate and record the normal force required to achieve the desired normal

stress. The cross-sectional area of the annular cavity is 1.031 in^2. Apply the desired normal stress using a single load ramp typically at a rate of 50 lbf/sec and activate the Keithley/LABTECH data acquisition system (Setup file: MK_TORQ)to begin recording the normal load, normal displacement, rotation, and torque at a sampling frequency of 5 Hz. (Use a double load ramp for overconsolidated torsion ring shear tests.)

9. After primary consolidation is completed, shear the specimen. Initially, shear the specimen at a relatively slow rate and increase the rate as desired. Different rates may be applied by employing a double rotation ramp with different rates of rotation.

10. After reaching the end of the waveform, stop the test apparatus. Remove the normal force from the specimen. Gingerly remove the torsion ring shear specimen by rotating along the failure plane. Do not pull the specimen perpendicularly to the failure surface, since it would damage the specimen. Photograph, SEM, sketch, or describe in writing the failure surface. The procedure is not applicable to cohesionless specimens.

11. Brush the apparatus clean, wipe with acetone, and store with a light coating of WD-40 to prevent rusting.

B.3 Uniaxial Strain Compression Test Procedure

The experimental procedure for the uniaxial strain system is relatively simple, and it involves the following steps:

1. Thoroughly clean all surfaces of apparatus with acetone.

2. Set the radial and lower pressure sensors flush with wall. Feed the instrumentation wires through the base and connect them to the Keithley AIM8 strain gauge bridge interface box.

3. Place powder containment cell on base and secure with set screws.

4. Liberally apply Teflon Powder Spray T-123 to inner die cavity.

5. Dry pluviate the powder into the cell to the desired initial relative density. (The initial relative density may be changed by altering the drop height or the funnel diameter.) Tampen surface with compression rod to ensure the top of the specimen is level.

6. Generously coat compression rod surface with Teflon Powder Spray T-123 and gingerly insert into cell until in full contact with top of specimen. Record the initial height of specimen on UCOMP data sheet.

7. Lift uniaxial strain apparatus into Instron loading frame.

8. Balance pressure sensor Wheatstone bridge, take base strain readings and start LABTECH computer data acquisition program. (Setup file: MK_UCOMP.) Enter initial offset values.

9. Set the waveform (typical DRAMP endpoint = 50,000 lbf at rate 10,000lbf/min; return to 0 lbf at rate 25,000lbf/min). Record optimized scale factors for load and displacement, and waveform on the data sheet. Also record waveform in data header file. When desired loading system endpoint is reached, reverse direction for unloading branch of experiment and reload if desired.

10. After load is taken to zero, remove the uniaxial constrained compression apparatus from the Instron loading frame and disassemble. The specimen generally needs to be forcibly extruded from the metal powder containment cell.

11. Immediately weigh specimen, and record dimensions on data sheet.

12. Brush the apparatus clean, wipe with acetone, and store with a light coating of WD-40 to prevent rusting.

B.4 Simple Compression Test Procedure

The experimental procedure for simple compression is well established (ASTM E9-89a), and it involves the following steps:

1. Clean the ends of the compression platen with acetone to remove all traces of grease and debris. If necessary, sand the extruded edges of the uniaxial strain compression specimen to obtain a level surface.

2. Measure the height and diameter of the uniaxial strain compression specimen with a micrometer. Calculate the average of at least three evenly spaced diameter and three height measurements. Calculate the average cross-sectional area of the specimen gage section.

3. Bearing surface friction can significantly affect test results. If contact friction between the specimen and compression platens is not minimized throughout the test, inhomogeneous deformation (e.g. barreling) will result. Cut four 30 mm square pieces of Teflon film. Friction has been successfully reduced by applying Dow Corning G-n lubricant between the Teflon sheets, and between the specimen bearing surface and Teflon sheet interface.

4. Mark the center of the compression platen; a 25.4 mm diameter circle in the center of the platen is recommended for alignment purposes. Place the specimen in the test fixture and carefully align the specimen to the fixture to ensure concentric loading. Also, check that the specimen loading/reaction surfaces mate evenly with the respective surfaces of the compression platens.

5. If desired, attach the extra short stroke linear potentiometer displacement sensor to measure the displacement locally between the compression platens and eliminate system compliance due to the load frame.

6. Set the load range and displacement range of the Instron testing machine so that the maximum expected ranges are at least two thirds of the ranges selected.

7. Set the machine to maintain a constant crosshead speed to obtain the desired average strain-rate from the start of loading to the end point of the test. The average strain-rate can be determined from a time-strain graph. Set the machine to strain

the specimen under a single ramp piston displacement control, using a constant displacement rate corresponding to an initial engineering strain rate of 0.001 s^{-1}. It should be noted that the use of machines with constant rate of crosshead movement does not ensure constant strain rate throughout the test. If desired, an automatic feedback control system has been implemented in LabView and is available.

8. After the specimen has been installed and aligned and the displacement measuring short stroke linear potentiometer installed, apply a 5 lbf preload, activate the LabView data acquisition system at a sampling frequency of 100 Hz, and initiate the test at the prescribed rate.

9. Monitor the stress-strain curve while the test is in progress and finish the single ramp displacement waveform once the specimen has failed.

10. Brush the apparatus clean, wipe with acetone, and store with a light coating of WD-40 to prevent rusting.

B.5 Ring Shear Friction Test Procedure

1. Replace the textured lower punch with the flat lower punch; otherwise the experimental procedure is identical to the Torsion Ring Shear Test Procedure.

Appendix C

Ring Shear Apparatus Technical Drawings

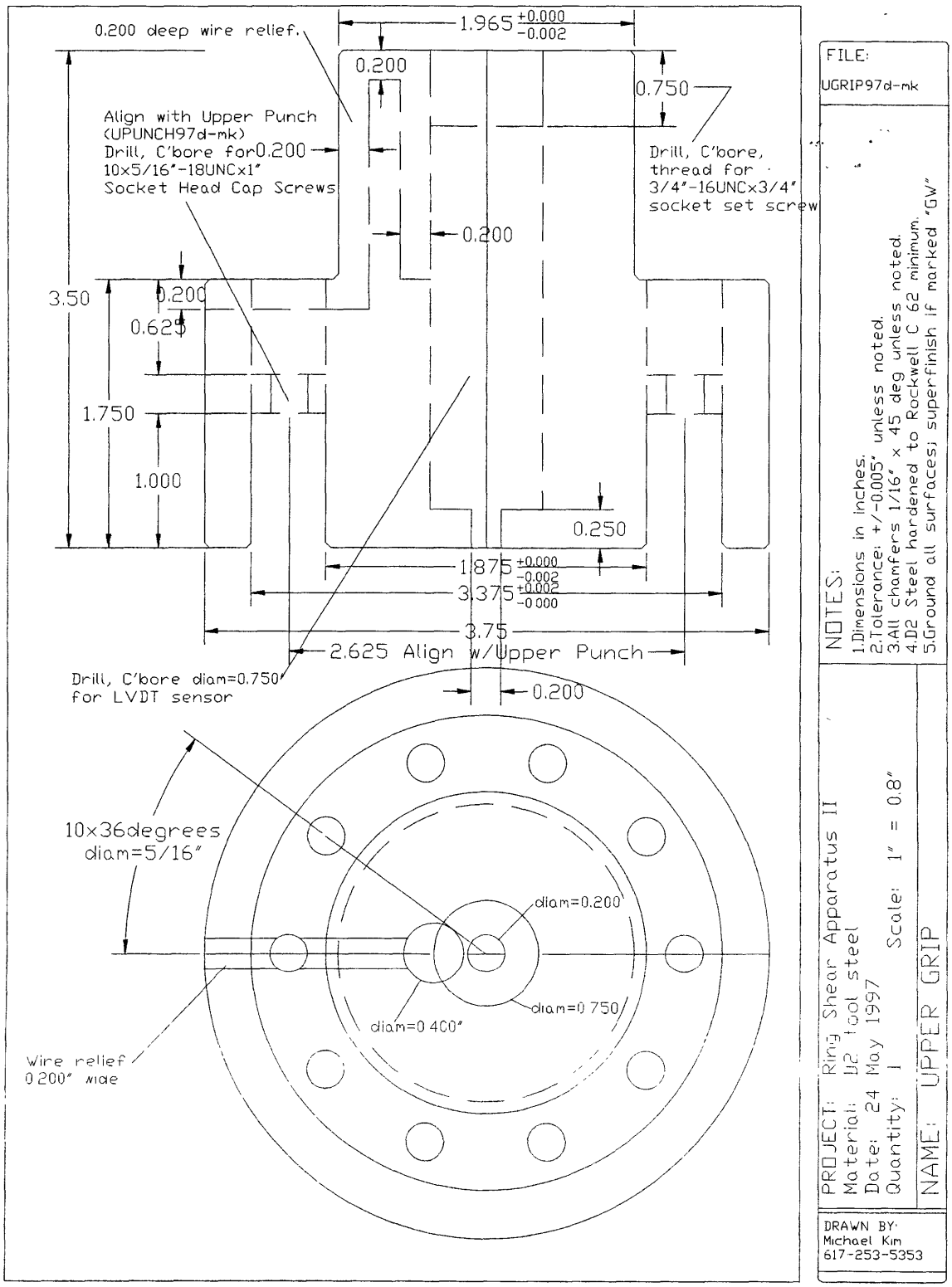

Figure C-1: Ring Shear Apparatus Upper Grip

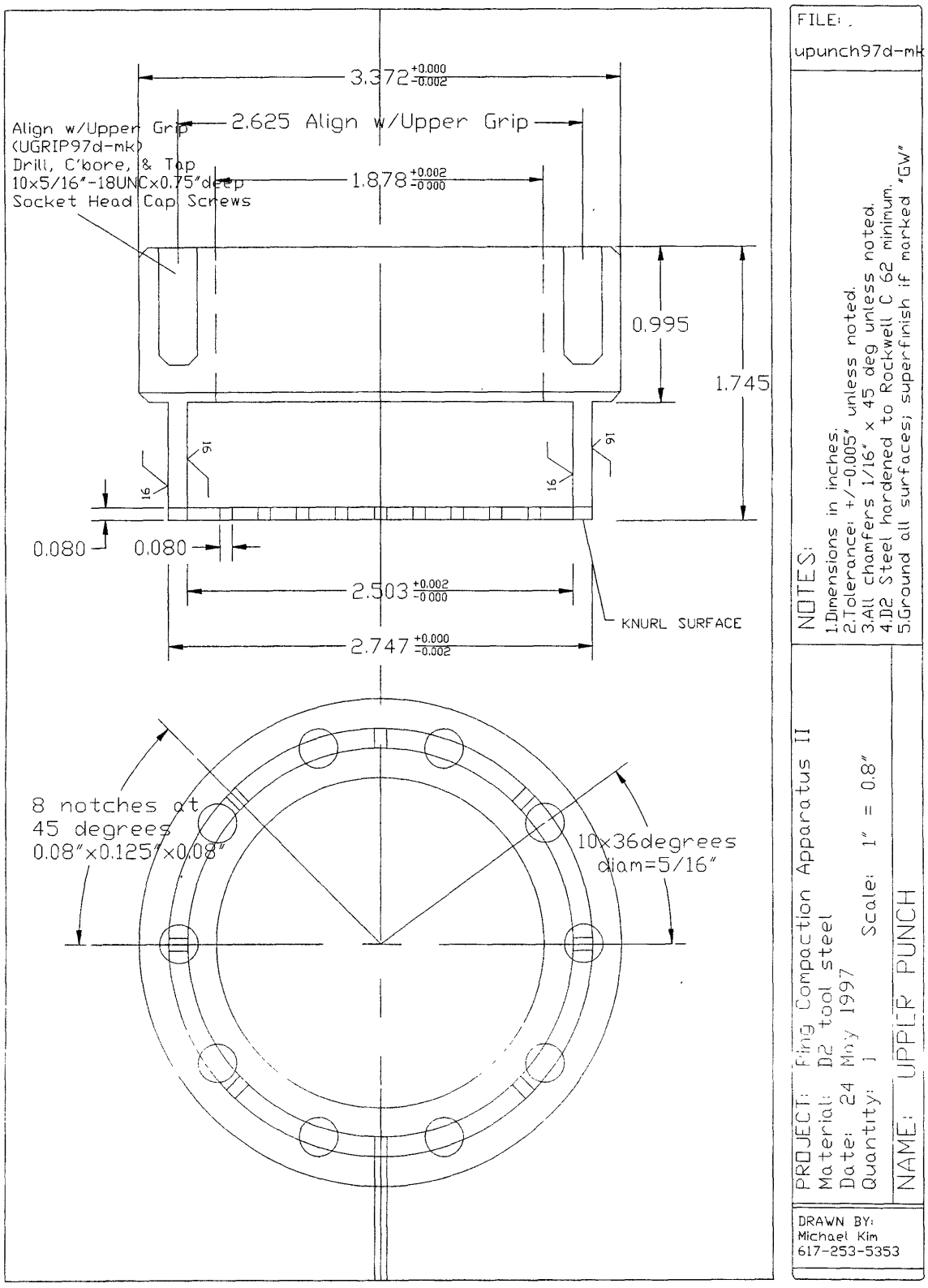

Figure C-2: Ring Shear Apparatus Upper Punch

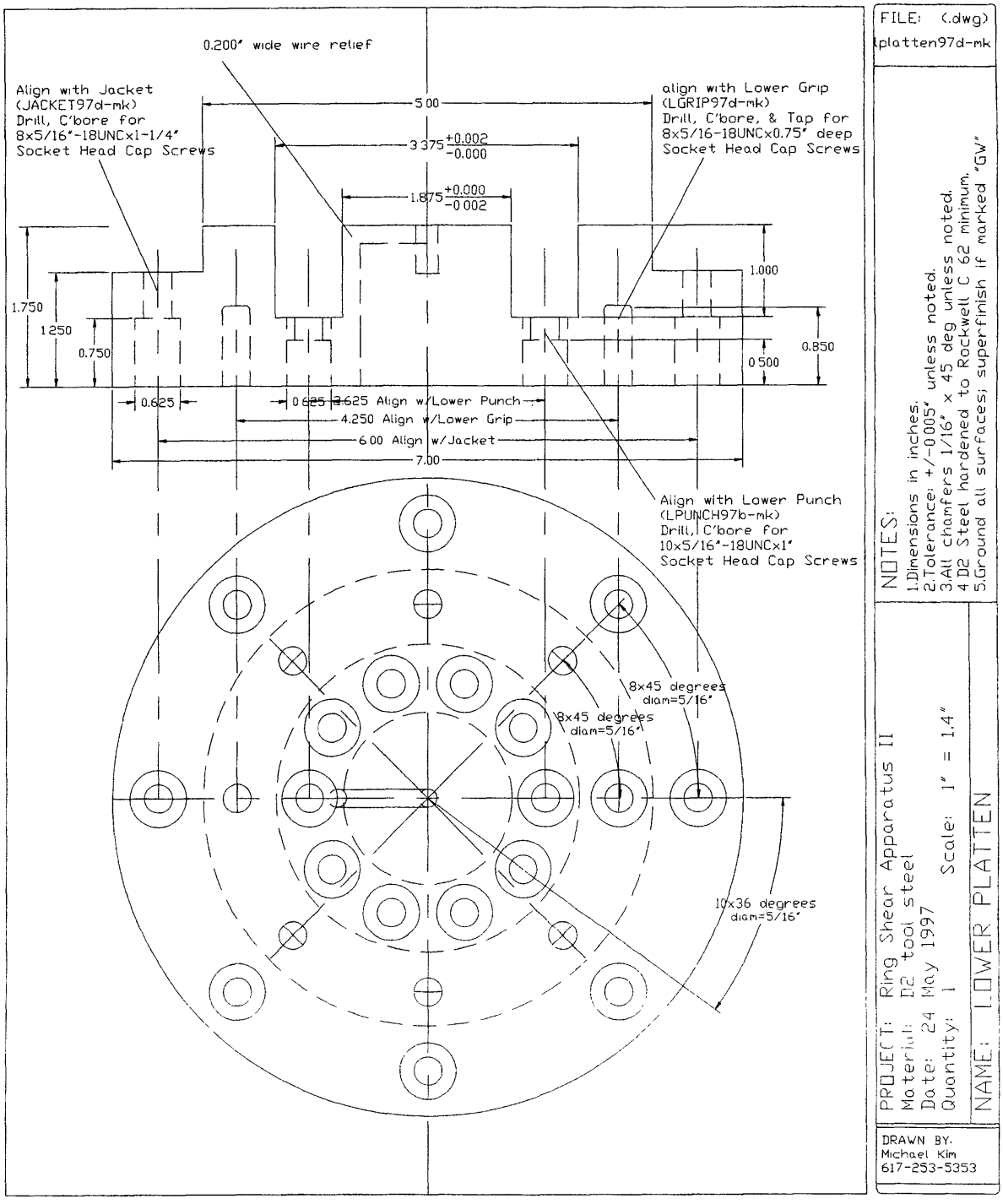

Figure C-3: Ring Shear Apparatus Lower Platen

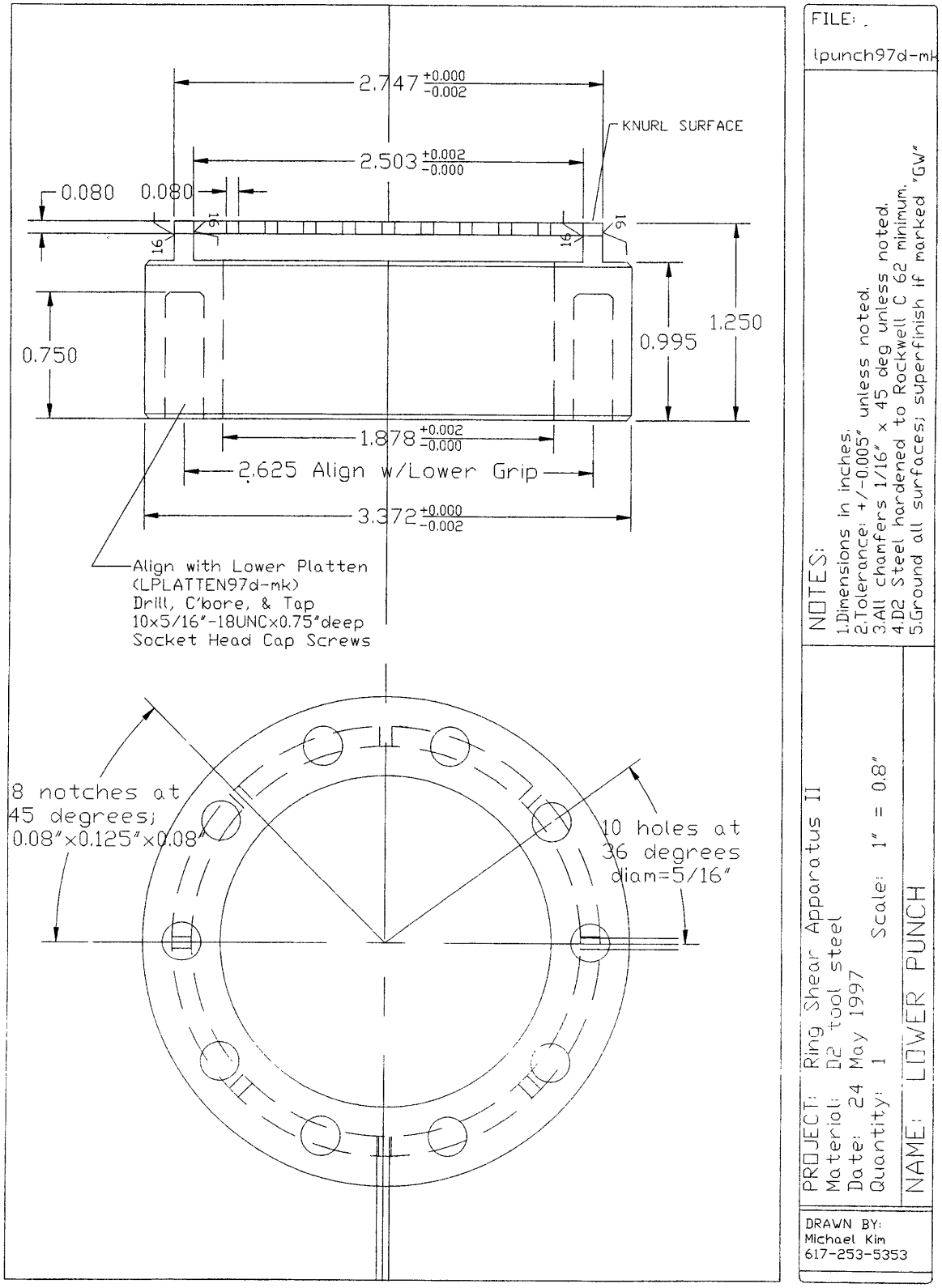

Figure C-4: Ring Shear Apparatus Lower Punch

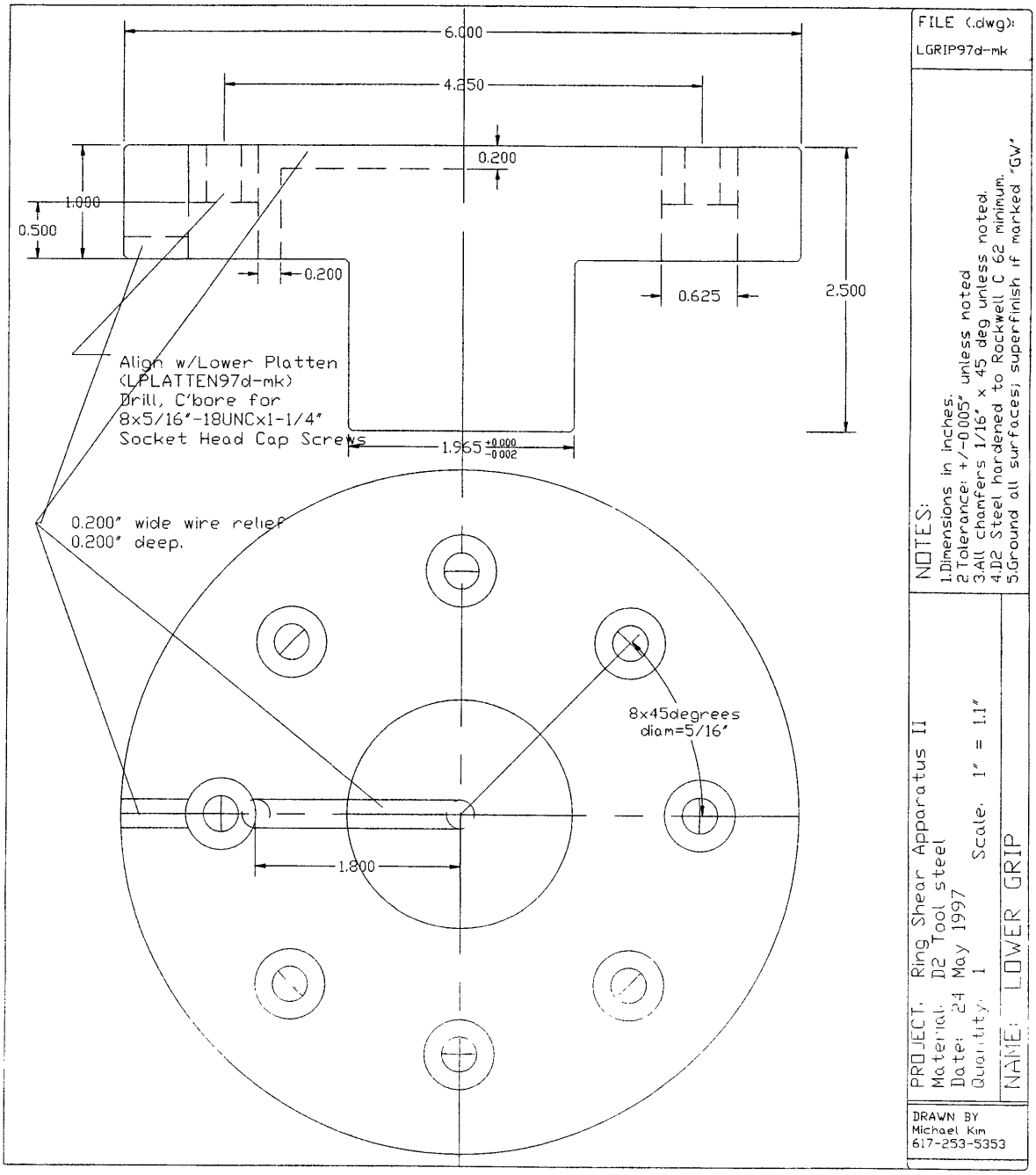

Figure C-5: Ring Shear Apparatus Lower Grip

Appendix D

Archiving Codes and Conventions

Figure D-1 shows the structure of the code used for classifying the individual experiments.

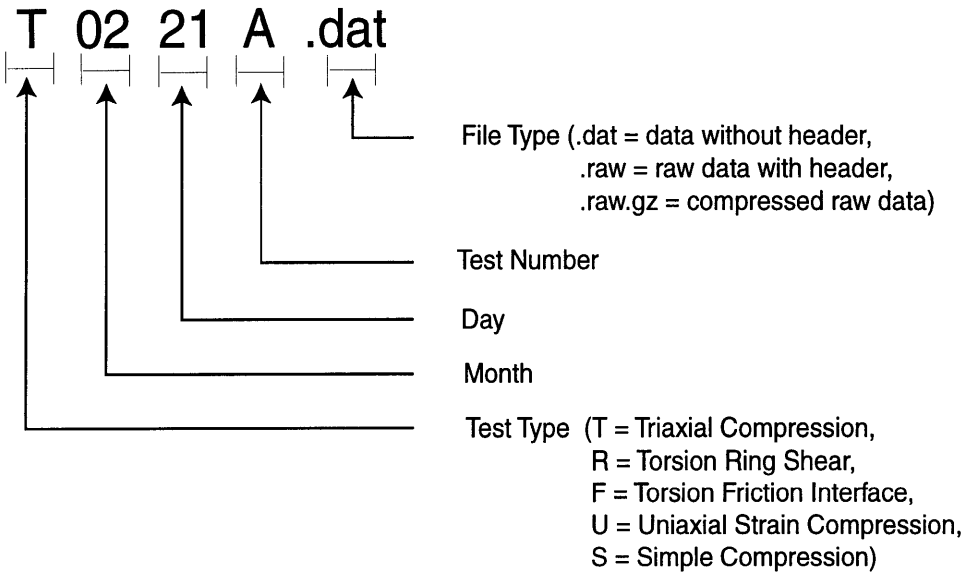

Figure D-1: Explanation of nomenclature.

Appendix E

Matlab Script Files

E.0.1 Triaxial Compression Test Script File

The following Matlab script file takes the triaxial compression LABTECH data .dat file and plots the following graph:

- Stress from Various Sensors versus Logarithmic Strain

```
%
% T  Triaxial Compression Testing data reduction
%
% The default material is MH-100 Iron Powder
%
% INPUT parameters which need to be updated for each test are:
% filename, final_heightx, final_heighty, final_heightz, SI_final_mass,
% sampling frequency, truncated filename, block configuration in
%
% OUTPUT  The following 1 graph is plotted:                              10
% Engineering Stress from Various Sensors versus Logarithmic Strain
%
% $Log:  T0221A.m,v$
% Revision 10  98/02/10  9:01:34  mikekim
%
%
name = 'T0221A.m'
```

```
% Clean up workspace
        clear all;
        close all;

% Load particular data
% Assumed format of .dat file:
% ttt(:,1) ~ column 1 is X-displacement  [0.001"]
% ttt(:,2) ~ column 2 is Y-displacement  [0.001"]
% ttt(:,3) ~ column 3 is Z-displacement  [0.001"]
% ttt(:,4) ~ column 4 is time  [sec]
% ttt(:,5) ~ column 5 is X-pressure  [psi]
% ttt(:,6) ~ column 6 is Y-pressure  [psi]
% ttt(:,7) ~ column 7 is Z-pressure  [psi]
        load t0221a.dat

% Rename particular data file to generic variable: ttt
        ttt = t0221a;

% t0221a.dat header info
% MH-100, Baldwin180kips,X45/Y45
% Sramp Posn 90kips@0.050in/min
% Sramp to 0kips@0.050in/min
% Date= 2-21-1998, TIME=16:43:55.08

% Determine size of ttt.dat file;
% [M,N] = size(ttt) returns the number of rows and columns, respectively:
        [M,N] = size(ttt)


%------------------
% CORRECTIONS
%------------------
% Offsets
        dispx_offset = ttt(1,1)
        dispy_offset = ttt(1,2)
```

```
        dispz_offset = ttt(1,3)
        time_offset = ttt(1,4)
        pressurex_offset = ttt(1,5)
        pressurey_offset = ttt(1,6)
        pressurez_offset = ttt(1,7)

% Subtract offsets from data                                          60
        ttt(:,1)=ttt(:,1)-dispx_offset;
        ttt(:,2)=ttt(:,2)-dispy_offset;
        ttt(:,3)=ttt(:,3)-dispz_offset;
        ttt(:,4)=ttt(:,4)-time_offset;
        ttt(:,5)=ttt(:,5)-pressurex_offset;
        ttt(:,6)=ttt(:,6)-pressurey_offset;
        ttt(:,7)=ttt(:,7)-pressurez_offset;


                                                                     70
%---------------
% AVERAGE
%---------------
% f = sampling frequency
        f=20;

% Initialize the sum# variables
     sum1=0; sum2=0; sum3=0; sum4=0; sum5=0; sum6=0; sum7=0; sum8=0; sum9=0;

% Store the average in ttt2(*,*)                                      80
     for I=0:f:(M-1),
       for J=1:f,
           sum1=sum1+ttt(I+J,1);
        sum2=sum2+ttt(I+J,2);
        sum3=sum3+ttt(I+J,3);
           sum4=sum4+ttt(I+J,4);
           sum5=sum5+ttt(I+J,5);
           sum6=sum6+ttt(I+J,6);
           sum7=sum7+ttt(I+J,7);
```

```
    end
      if I == 0
        ttt2(2,1)=sum1/f;
        ttt2(2,2)=sum2/f;
     ttt2(2,3)=sum3/f;
        ttt2(2,4)=sum4/f;
        ttt2(2,5)=sum5/f;
        ttt2(2,6)=sum6/f;
        ttt2(2,7)=sum7/f;
      else
     ttt2(I/f,1)=sum1/f;
     ttt2(I/f,2)=sum2/f;
     ttt2(I/f,3)=sum3/f;
     ttt2(I/f,4)=sum4/f;
     ttt2(I/f,5)=sum5/f;
     ttt2(I/f,6)=sum6/f;
     ttt2(I/f,7)=sum7/f;
      end
   sum1=0; sum2=0; sum3=0; sum4=0; sum5=0;
      sum6=0; sum7=0; sum8=0; sum9=0;
  end

% Initialize the first data point
    ttt2(1,1)=0;
    ttt2(1,2)=0;
    ttt2(1,3)=0;
    ttt2(1,4)=0;
    ttt2(1,5)=0;
    ttt2(1,6)=0;
    ttt2(1,7)=0;

      ttt2(:,1)=ttt2(:,1)/1000*25.4;
      ttt2(:,2)=ttt2(:,2)/1000*25.4;
      ttt2(:,3)=ttt2(:,3)/1000*25.4;
      ttt2(:,5)=ttt2(:,5)*4.448/.0254/.0254/1e6;
      ttt2(:,6)=ttt2(:,6)*4.448/.0254/.0254/1e6;
```

```
ttt2(:,7)=ttt2(:,7)*4.448/.0254/.0254/1e6;

% Save averaged data
save t0221a2.dat ttt2 -ascii -double -tabs
load t0221a2.dat;
ttt= t0221a2;
[M,N]=size(ttt);


%-----------------------
% INPUT PARAMETERS
%-----------------------
% Final compacted specimen heights, final_height# [0.001 in]:
final_heightx = (0.7870+0.7880+0.7900+0.7900)/4*25.4
final_heighty = (0.8030+0.8050+0.8070+0.8060)/4*25.4
final_heightz = (0.8020+0.8020+0.8020+0.8015)/4*25.4

% Final mass, final_mass [grams]:
final_mass = 53.14

% Density Fe, density [g/cm^3]:
density = 7.8

% Calculate current height, height(xyz) [in]:
heightx(M) = final_heightx;
heighty(M) = final_heighty;
heightz(M) = final_heightz;

for i = 1:M,
  heightx(i) = heightx(M)+ttt(M,1)-ttt(i,1);
  heighty(i) = heighty(M)+ttt(M,2)-ttt(i,2);
  heightz(i) = heightz(M)+ttt(M,3)-ttt(i,3);
end

% Calculate engineering strain, estrain(xyz) [mm/mm]:
estrainx = (ttt(:,1)/heightx(1));
```

```
estrainy = (ttt(:,2)/heighty(1));
estrainz = (ttt(:,3)/heightz(1));

% Calculate true strain, tstrain(xyz)  [mm/mm]:
tstrainx = abs(log(1-estrainx));
tstrainy = abs(log(1-estrainy));
tstrainz = abs(log(1-estrainz));

% Calculate current total volume, total_volume  [mm^3]:
total_volume = heightx.*heighty.*heightz;

% Calculate solid volume, solid_volume  [mm^3]:
solid_volume = final_mass/density*10*10*10

% Calculate current void volume, void_volume  [mm^3]:
void_volume = total_volume-solid_volume;

% Calculate void fraction, e=void_volume/solid_volume [mm^3/mm^3]:
e = void_volume./solid_volume;

% Calculate hydrostatic/mean pressure, mean_p  [psi]:
mean_p = (ttt(:,5)+ttt(:,6)+ttt(:,7))/3;

% Calculate effective shear stress, q  [psi]:
q = (1/6*((ttt(:,5)-ttt(:,6)).^2 ...
   +(ttt(:,6)-ttt(:,7)).^2 ...
+(ttt(:,7)-ttt(:,5)).^2)).^.5;


%--------------
% FIGURES
%--------------
% FIGURE 3-12:  STRESS FROM VARIOUS SENSORS
% versus LOGARITHMIC STRAIN
figure
plot(tstrainz*100,ttt(:,7),'bs:')
```

```
hold
plot(tstrainy*100,ttt(:,6),'wV:')
plot(tstrainx*100,ttt(:,5),'r^:')
legend('\sigma_{1}','\sigma_{2}','\sigma_{3}')
xlabel('LOGARITHMIC STRAIN  [%]  (Compression is Positive)')
ylabel('STRESS FROM VARIOUS SENSORS  [MPa]')
axis([0 50 0 250])
axis square
grid
```

E.0.2 Torsion Ring Shear Test Script File

The following Matlab script file takes the torsion ring shear LABTECH data .dat file and plots the following graphs:

- Shear Stress versus Sliding Distance
- Shear Stress versus Normal Stress

```
%
% R  Torsion Ring Shear Test Data Reduction
%
% The default material is MH-100 Iron Powder
%
% INPUT parameters which need to be updated for each test are:
% filename,
%
%
% OUTPUT  The following 1 graph is plotted:                    10
% Shear Stress versus Sliding Distance
% Shear Stress versus Normal Stress
%
% $Log:  R0829A.m,v$
% Revision 3  98/08/29  10:39:33  mikekim
%
%
name = 'R0829A.m'

% Clear workspace                                             20
        clear all;
        close all;

% Load data
        load R0829a2.dat  %25 MPa
        load R0829b2.dat  %50 MPa
        load R0829c2.dat  %75 MPa
```

```
%------------------------
% INPUT PARAMETERS
%------------------------
%% Geometry of Apparatus [in]
  Ro = 2.750/2
  Ri = 2.500/2
  Rm = (Ro+Ri)/2
  t = (Ro-Ri)

% Density Fe, density [g/cm^3]:
        density = 7.87

% Rename data files to more general filenames
        dat1=R0829a2;
        dat2=R0829b2;
        dat3=R0829c2;


%---------------
% OFFSETS
%---------------
% Subtract rotation offset
        dat1(:,5)=dat1(:,5)-dat1(1,5);
        dat2(:,5)=dat2(:,5)-dat2(1,5);
        dat3(:,5)=dat3(:,5)-dat3(1,5);

%--------------------
% CALCULATIONS
%--------------------
% Calculate projected area
        area = (Ro^2-Ri^2)*pi

% Axial Stress
        stress1 = dat1(:,3)/area/1000*6.98;
        stress2 = dat2(:,3)/area/1000*6.98;
```

```
stress3 = dat3(:,3)/area/1000*6.98;

% Shear stress [MPa]
shear1 = (3*dat1(:,6))/(2*pi*(Ro^3-Ri^3))/1000*6.98;
shear2 = (3*dat2(:,6))/(2*pi*(Ro^3-Ri^3))/1000*6.98;
shear3 = (3*dat3(:,6))/(2*pi*(Ro^3-Ri^3))/1000*6.98;

% Sliding distance [mm]
disp1=(dat1(:,5)*pi/180)*Rm*25.4;
disp2=(dat2(:,5)*pi/180)*Rm*25.4;
disp3=(dat3(:,5)*pi/180)*Rm*25.4;



%---------------
% FIGURES
%---------------
% FIGURE 3-24:  SHEAR STRESS
% versus SLIDING DISTANCE
figure
plot(disp1,shear1,'go:')
hold on
grid on
plot(disp2,shear2,'r^:')
plot(disp3,shear3,'bs:')
xlabel('SLIDING DISTANCE,  \delta  [mm]')
ylabel('AVERAGE SHEAR STRESS,  \tau  [MPa]')
axis([0 50 0 100])
axis square
legend('\sigma_{n}=25 MPa', '\sigma_{n}=50 MPa', ...
    '\sigma_{n}=75 MPa')
```

E.0.3 Torsion Interface Friction Test Script File

The following Matlab script file takes the torsion friction interface LABTECH data .dat file and plots the following graph:

- Shearing Resistance versus Sliding Distance

```
%
% F  Torsion Interface Friction Test Data Reduction
%
% The default material is MH-100 Iron Powder
%
% INPUT parameters which need to be updated for each test are:
% filename, normal stress
%
% OUTPUT  The following 1 graph is plotted:
% Shearing Resistance versus Sliding Distance                    10
%
% $Log:  F1027J.m,v$
% Revision 4  98/10/27  9:28:35  mikekim
%
%
name = 'F1027J.m'


% Clear workspace
        clear all;                                               20
        close all;

% Load data
        load F1027J.dat
        load F1027K.dat
        load F1027L.dat
        load F1027M.dat
        load F1027N.dat
        load F1027O.dat
```

```
                                                                    30
% Rename data files to more general filenames
        F1=F1027J;
        F2=F1027K;
        F3=F1027L;
        F4=F1027M;
        F5=F1027N;
        F6=F1027O;


%------------------------                                            40
% INPUT PARAMETERS
%------------------------
% Geometry of Apparatus [in]
        Ro = 2.750/2
        Ri = 2.500/2
        Rm = (Ro+Ri)/2
        t = (Ro-Ri)

% Calculate projected area
        area = (Ro^2-Ri^2)*pi                                       50

% Enter normal stress [MPa]
        n1=10000/area/1000*6.98
        n2=7500/area/1000*6.98
        n3=5000/area/1000*6.98
        n4=2500/area/1000*6.98
        n5=1250/area/1000*6.98
        n6=625/area/1000*6.98


                                                                    60
%--------------------
% CALCULATIONS
%--------------------
% Calculate sliding distance [mm]
        F1(:,1)=(F1(:,1)-F1(1,1))*pi/180*Rm*25.4;
```

```
F2(:,1)=(F2(:,1)-F2(1,1))*pi/180*Rm*25.4;
F3(:,1)=(F3(:,1)-F3(1,1))*pi/180*Rm*25.4;
F4(:,1)=(F4(:,1)-F4(1,1))*pi/180*Rm*25.4;
F5(:,1)=(F5(:,1)-F5(1,1))*pi/180*Rm*25.4;
F6(:,1)=(F6(:,1)-F6(1,1))*pi/180*Rm*25.4;                    70

% Calculate shear stress [MPa]
F1(:,2) = (3*F1(:,2))/(2*pi*(Ro^3-Ri^3))/1000*6.98;
F2(:,2) = (3*F2(:,2))/(2*pi*(Ro^3-Ri^3))/1000*6.98;
F3(:,2) = (3*F3(:,2))/(2*pi*(Ro^3-Ri^3))/1000*6.98;
F4(:,2) = (3*F4(:,2))/(2*pi*(Ro^3-Ri^3))/1000*6.98;
F5(:,2) = (3*F5(:,2))/(2*pi*(Ro^3-Ri^3))/1000*6.98;
F6(:,2) = (3*F6(:,2))/(2*pi*(Ro^3-Ri^3))/1000*6.98;

                                                             80
%---------------
% FIGURES
%---------------
% Figure 3-29: SHEARING RESISTANCE
% versus SLIDING DISTANCE
figure
plot(F1(:,1),F1(:,2),'x')
hold on
plot(F2(:,1),F2(:,2),'+')
plot(F3(:,1),F3(:,2),'*')                                    90
plot(F4(:,1),F4(:,2),'s')
plot(F5(:,1),F5(:,2),'d')
plot(F6(:,1),F6(:,2),'v')
grid on
axis square
xlabel('SLIDING DISTANCE  [mm]')
ylabel('SHEARING RESISTANCE  [MPa]')
text(3.1, 3.1, 'p = 68 MPa -> 4 MPa')
text(3.1, 5.1, 'p = 68 MPa -> 9 MPa')
text(3.1, 9,   'p = 68 MPa -> 17 MPa')                       100
text(3.1, 15,  'p = 68 MPa -> 34 MPa')
```

```
text(3.1, 21.2,'p = 68 MPa ->51 MPa')
text(3.1, 25.2,'p = 68 MPa')
axis([0 6 0 30])
```

E.0.4 Uniaxial Strain Test Script File

The following Matlab script file takes the uniaxial strain test LABTECH data .dat file, and plots the following graphs:

- Engineering Stress from Various Sensors versus Logarithmic Strain
- Engineering Stress versus Relative Density, η

```
%
% U  Uniaxial Constrained Compression Data Reduction.
%
% The default material is MH-100 Iron Powder.
%
% INPUT parameters which need to be updated for each test are:
% filename, diameter, final_height, SI_final_mass, coefficient of friction
%
% OUTPUT  The following 2 graphs are plotted:
% Engineering Stress from Various Sensors versus Logarithmic Strain
% Engineering Stress versus Relative Density
%
% $Log:  U0625E.m,v $
% Revision 7  98/06/26  20:43:50  mikekim
%
name = 'U0625E.m'

% Clean up workspace
        clear all;
        close all;

% Load particular data
% Assumed format of .dat file:
% uc(:,1) ~ column 1 is DISPLACEMENT via LINEAR POT  [in]
% uc(:,2) ~ column 2 is LOWER PRESSURE SENSOR  [psi]
% uc(:,3) ~ column 3 is RADIAL PRESSURE SENSOR [psi]
% uc(:,4) ~ column 4 is TIME  [sec]
% uc(:,5) ~ column 5 is INSTRON UPPER LOAD CELL [lbf]
```

```
% uc(:,6) ~ column 6 is INSTRON DISPLACEMENT [in]
% uc(:,7) ~ column 7 is CALCULATED UPPER PRESSURE [psi]
      load U0625e.dat

% U0625e.dat header info
% UCOMP,MH-100,Bi-Instron
% Load to 50kips@200lbf/sec
% unload to 0kips@500lbf/sec
% DATE: 6-25-1998. TIME: 17:23:09.85.

% Rename particular data file to generic variable: uc
      uc=U0625e;


%-----------------------------
% INPUT PARAMETERS
%-----------------------------
% Final compacted specimen height, final_height [mm]:
      final_height = (0.578+0.579)*25.4/2

% Final diameter [mm]:
      diameter = (1.002+1.0015)*25.4/2

% Final mass, final_mass [grams]:
      final_mass = 49.96

% Density Fe, density [g/cm^3]:
      density = 7.87

% Radius [mm]:
      radius = 0.5*diameter;

% Area, area [mm^2]:
      area = pi*radius^2

% Poisson's ratio
```

```
nu = 0.300


%------------------
% CORRECTIONS
%------------------
% Determine size of uc.dat file;
% [M,N] = size(uc) returns the number of rows and columns, respectively
    [M,N]=size(uc)

% Correct displacement for compliance:
% Since a small specimen is used and the stiffness of the specimen is very
% high at large stress levels, accurate determination of the vertical
% deformation is essential to accurately estimate the void ratio.
% A correction to the axial deformation of the specimen for the elastic
% compression of the loading apparatus is necessary to ensure this accuracy.
    uc(:,6)=uc(:,6)-(0.0024497397+9.7476869e-7*uc(:,5));

% Convert to data file to SI units:
    uc(:,1)=uc(:,1)*25.4;
    uc(:,2)=uc(:,2)*4.448/.0254/.0254/1e6;
    uc(:,3)=uc(:,3)*4.448/.0254/.0254/1e6;
    uc(:,5)=uc(:,5)*4.448/area;
    uc(:,6)=uc(:,6)*25.4;

% Offsets
    lower_pressure_offset=uc(1,2);
    radial_pressure_offset=uc(1,3);
    time_offset=uc(1,4);
    disp_offset=uc(1,6);

% Subtract offsets from data
    uc(:,2)=uc(:,2)-lower_pressure_offset;
    uc(:,3)=uc(:,3)-radial_pressure_offset;
    uc(:,4)=uc(:,4)-time_offset;
    uc(:,6)=uc(:,6)-disp_offset;
```

```
%--------------
% AVERAGE
%--------------
        f=25;

% Initialize the sum# variables
      sum1=0; sum2=0; sum3=0; sum4=0; sum5=0; sum6=0;
                                                                    110
% Store the average in ttt2(*,*)
      for I=0:f:(M-1),
       for J=1:f,
           sum1=sum1+uc(I+J,1);
        sum2=sum2+uc(I+J,2);
        sum3=sum3+uc(I+J,3);
           sum4=sum4+uc(I+J,4);
           sum5=sum5+uc(I+J,5);
           sum6=sum6+uc(I+J,6);
       end                                                          120
         if I == 0
           ttt2(2,1)=sum1/f;
           ttt2(2,2)=sum2/f;
        ttt2(2,3)=sum3/f;
           ttt2(2,4)=sum4/f;
           ttt2(2,5)=sum5/f;
           ttt2(2,6)=sum6/f;
         else
        ttt2(I/f,1)=sum1/f;
        ttt2(I/f,2)=sum2/f;                                         130
        ttt2(I/f,3)=sum3/f;
        ttt2(I/f,4)=sum4/f;
        ttt2(I/f,5)=sum5/f;
        ttt2(I/f,6)=sum6/f;
         end
       sum1=0; sum2=0; sum3=0; sum4=0; sum5=0; sum6=0;
```

```
    end

% Initialize the first data point
    ttt2(1,1)=0;                                                    140
    ttt2(1,2)=0;
    ttt2(1,3)=0;
    ttt2(1,4)=0;
    ttt2(1,5)=0;
    ttt2(1,6)=0;
    ttt2(1,7)=0;

% Save averaged data
        save U0625E2.dat ttt2 -ascii -double -tabs
        load U0625E2.dat;                                           150
        uc= U0625E2;
        [M,N]=size(uc);



%-----------------
% CALCULATE
%-----------------
% Initial height, initial_height [mm]:
        initial_height = final_height+max(uc(:,6))-0.010*25.4;      160

% Calculate engineering strain, estrain [mm/mm]:
        estrain = (uc(:,6)/initial_height);

% Calculate true strain, tstrain [mm/mm]:
        tstrain = abs(log(1-estrain));

% Calculate current height, height [mm]:
        height = initial_height-uc(:,6);
                                                                    170
% Calculate current total volume, total_volume  [mm^3]:
        total_volume = area*height;
```

```
% Calculate solid volume, solid_volume [mm^3]:
        solid_volume = (final_mass/density)*10*10*10;

% Calculate current void volume, void_volume [mm^3]:
        void_volume = total_volume-solid_volume;

% Calculate void fraction, e=void_volume/solid_volume [mm^3/mm^3]:
        e = void_volume/solid_volume;

% Calculate relative density:
        eta=1-(e./(1+e));

% Calculate hydrostatic/mean pressure, mean_p [MPa]:
        mean_p = (uc(:,2)+2*uc(:,3))/3;

% Calculate deviator stress, deviator [MPa]:
        deviator = abs(uc(:,2)-uc(:,3))/sqrt(3);


%---------------
% FIGURES
%---------------
% FIGURE 3-35: ENGINEERING STRESS from VARIOUS SENSORS
% versus LOGARITHMIC STRAIN
        figure
        plot(tstrain*100, uc(:,5),'r^:')
        hold
        plot(tstrain*100, uc(:,2),'wV:')
        plot(tstrain*100, uc(:,3),'bs:')
        xlabel('LOGARITHMIC AXIAL STRAIN  [%]')
        ylabel('ENGINEERING STRESS from VARIOUS SENSORS  [MPa]')
        grid
        axis([0 100 0 500])
        axis square
        legend('\sigma_{z,upper}','\sigma_{z,lower}','\sigma_{r}')
```

```
% FIGURE 3-36.  AXIAL ENGINEERING STRESS                              210
% versus RELATIVE DENSITY
      figure
      plot(eta, uc(:,2),'o:')
      xlabel('RELATIVE DENSITY, \eta  ')
      ylabel('AXIAL ENGINEERING STRESS [MPa]')
      grid
      axis([0.4 1 0 500])
      axis square

                                                                       220
```

E.0.5 Simple Compression Test Script File

The following Matlab script file takes the simple compression LabView data .dat file and plots the following graph:

- Engineering Stress versus. True Strain

```
%
% S  Simple Compression Testing data reduction
%
% The default material is MH-100 Iron Powder
%
% INPUT parameters which need to be updated for each test are:
% filename, heights, diameters
%
% OUTPUT  The following 1 graphs are plotted:
% Engineering Stress from Various Sensors versus Logarithmic Strain
%
% $Log:  S0625.m,v$
% Revision 1  98/06/26  10:46:34  mikekim
%
%
name = 'S0625.m'

% Clean up workspace
        clear all;
        close all;

% Load particular data
% Assumed format of .dat file:
% sc1(:,1) ~ column 1 is Displacement [in]
% sc1(:,2) ~ column 2 is Load  [lbf]
% sc1(:,3) ~ column 3 is Time  [sec]
        load S0625A.dat
        load S0625B.dat
        load S0625C.dat
```

```
load S0625D.dat
load S0625E.dat

% S0625A.dat header info:
% 6/28/98 21:37:50      ho=.818;do=1.000;m=49.80g
% S0625B.dat header info:
% 6/28/98 23:19:30      ho=.707;do=1.002;m=50.00g
% S0625C.dat header info:
% 6/29/98 0:02:14       ho=.643;do=1.002;m=50.03g
% S0625D.dat header info:
% 6/29/98 0:02:14       ho=.608;do=1.002;m=50.05g
% S0625E.dat
% 6/29/98 1:34:56       ho=.577;do=1.0035;m=49.96g

% Rename particular data file to generic variables:
    sc1=S0625A;
    sc2=S0625B;
    sc3=S0625C;
    sc4=S0625D;
    sc5=S0625E;

%------------------------
% INPUT PARAMETERS
%------------------------
% Heights
    h1 = .818
    h2 = .707
    h3 = .643
    h4 = .608
    h5 = .577

% Diameters
    d1 = 1.00
    d2 = 1.002
    d3 = 1.002
    d4 = 1.002
```

```
        d5 = 1.0035

%-------------
% OFFSETS
%-------------
        offset1=sc1(1,3);
        offset2=sc2(1,3);
        offset3=sc3(1,3);
        offset4=sc4(1,3);
        offset5=sc5(1,3);

%-----------------
% CALCULATIONS
%-----------------
% Engineering Strain
        e1=(sc1(:,3)-offset1)/h1;
        e2=(sc2(:,3)-offset2)/h2;
        e3=(sc3(:,3)-offset3)/h3;

% These two displacements recorded in thousandths of an inch
        e4=(sc4(:,3)-offset4)/1000/h4;
        e5=(sc5(:,3)-offset5)/1000/h5;

% Engineering Stress
        s1=sc1(:,2)/(pi*(d1/2)^2);
        s2=sc2(:,2)/(pi*(d2/2)^2);
        s3=sc3(:,2)/(pi*(d3/2)^2);
        s4=sc4(:,2)/(pi*(d4/2)^2);
        s5=sc5(:,2)/(pi*(d5/2)^2);

% True Strain
        t1=abs(log(1-e1));
        t2=abs(log(1-e2));
        t3=abs(log(1-e3));
        t4=abs(log(1-e4));
        t5=abs(log(1-e5));
```

```
%-------------
% FIGURE
%-------------
% FIGURE 3-43:  ENGINEERING STRESS
% versus TRUE STRAIN
        figure
        plot(t5*100,s5/1e3*7,'p')                                          110
        hold
        plot(t4*100,s4/1e3*7,'d')
        plot(t3*100,s3/1e3*7,'^')
        plot(t2*100,s2/1e3*7,'s')
        plot(t1*100,s1/1e3*7,'o')
        xlabel('TRUE STRAIN  [%]')
        ylabel('ENGINEERING STRESS  [MPa]')
        grid
        axis([0 15 0 250])
        axis square                                                        120
        legend('\eta=85.0%','\eta=81.3%', ...
             '\eta=76.6%','\eta=69.6%','\eta=60.4%')hs of an inch
```

Bibliography

[1] American Society for Metals *Metals Handbook.* American Society for Metals, Ohio, 1984.

[2] Anand, L. Constitutive Equations for Rate-Independent, Isotropic Elastic-Plastic Solids Exhibiting Pressure-Sensitive Yielding and Plastic Dialatancy. *ASME Journal of Applied Mechanics*, 47:439–441, 1980.

[3] Anand, L. Plane Deformations of Ideal Granular Materials. *J. Mech. Phys. Solids.*, 31:105–122, 1983.

[4] Lubliner, J. *Plasticity Theory.* 1990. Macmillan Publishing Company, New York.

[5] Malvern, L. *Introduction to the Mechanics of a Continuous Medium.* 1969. Prentice-Hall, Inc., New Jersey.

[6] Gurson, A.L. and McCabe, T.J. Experimental Determination of Yield Functions for Compaction of Blended Metal Powders. *Proceedings, MPIF/APMI World Congress on Powder Metallurgy and Particular Materials*, June 21-26, 1992, San Francisco, CA, U.S.A. Metal Powder Industries Federation.

[7] Brown, S. and Abou-Chedid, G. Yield Behavior of Metal Powder Assemblages. *J. Mech. Phys. Solids*, 42:383–399, 1994.

[8] Brown, S. and Abou-Chedid, G. Evaluation of Yield Functions Due to Powder Cohesion. *Proc. MPIF/APMI International Conference on Powder Metallurgy and Particulate Materials*, 16-19 May, Nashville, Tennessee, U.S.A. Metal Powder Industries Federation, 1993.

[9] Brown, S. and Abou-Chedid, G. Appropriate Yield Functions for Metal Powder Compaction. *Scripta Metallurgica*, 28:11-16, 1993.

[10] Akisanya, A.R., Cocks, A.C.F., and Fleck, N.A. The Yield Behaviour of Metal Powders *Int. J. Mech. Sci.*, 39(12):1315–1324, 1997.

[11] Kuhn, H.A. and Downey, C.L. Deformation Characteristics and Plasticity Theory of Sintered Powder Materials. *Int. J. Powder Metall.*, 7(1):15–25, 1971.

[12] Green, R.J. A Plasticity Theory for Porous Solids *Int. J. Mech. Sci.*, 14:215–224, 1972.

[13] Shima, S. and Oyane, M. Plasticity Theory for Porous Metals. *Int. J. Mech. Sci.*, 18:285–291, 1976.

[14] Gurson, A.L. Continuum Theory of Ductile Rupture by Void Nucleation and Growth: Part I–Yield Criteria and Flow Rules for Porous Ductile Media. *J. Eng. Mater. Technol.*, 99:2–15, 1977.

[15] Doraivelu, S.M., Gegel, H.L., Gunasekera, J.S., Malas, J.C., and Morgan, J.T. A New Yield Function for Compressible P/M Materials. *Int. J. Mech. Sci.*, 26(9/10):527-535, 1984.

[16] Haghi, M. and Anand, L. A Constitutive Model for Isotropic, Porous, Elasto-Viscoplastic Metals. *Mechanics of Materials*, 13:37–53, 1992.

[17] Zavaliangos, A and Anand, L. Thermo-Elasto-Viscoplasticity of Isotropic Porous Metals. *J. Mech. Phys. Solids*, 41:1087–1118, 1993.

[18] Drucker, D.C. and Prager, W. Soil Mechanics and Plastic Analysis or LImit Design. *Q. Appl. Math.*, 10:157-165, 1952.

[19] DiMaggio, F.L. and Sandler, I.S. Material Model for Granular Soils *Proceedings of the ASCE*, 97:935–950, 1971.

[20] Heckel, R.W. Density-Pressure Relationships in Powder Compaction. *Trans. Met. Soc. AIME*, 221:671–675, 1961.

[21] Heckel, R.W. An Analysis of Powder Compaction Phenomena. *Trans. Mat. Soc. AIME*, 221:1001–1008, 1961.

[22] Kostelnick, M.C., Kludt, F.H., and Beddow, J.K. The Initial Stage of Compaction of Metal Powders in a Die. *Int. J. Powder Metall.*, 4(4):19–28, 1968.

[23] Hewitt, R.L., Wallace, W., and deMalherbe, M.C. The Effects of Strain-Hardening in Powder Compaction. *Powder Metall.*, 16:88–106, 1973.

[24] James, P.J. Particle Deformation During Cold Isostatic Pressing of Metal Powders. *Powder Metall.*, 4:199–204, 1977.

[25] Fleck, N.A., Kuhn, L.T., and McMeeking, R.M. Yielding of Metal Powder Bonded by Isolated Contacts. *J. Mech. Phys. Solids*, 40(5):1139–1162, 1992.

[26] Koczak, M.J. and Lawley, A. The Effect of Particle Size and Shape on the Mechanical Properties of Sintered Iron Compacts. *Powder Metall. Int.*, 4(4):186–191, 1972.

[27] Yamamuro, J.A. and Lade, P.V. Drained Sand Behavior in Axisymmetric Tests at High Pressures *J. Geotech. Engrg.*, ASCE, 122(2):109–119, 1996.

[28] Pestana-Nascimento, J.M. *A Unified Constitutive Model for Clays and Sands.* Ph.D. dissertation, M.I.T., 1994.

[29] Hausner, H.H. Friction Conditions in a Mass of Metal Powder *Int. J. of Powder Metall.*, 3(4):7–13, 1967.

[30] Anand, L. Elastic Moduli of Gray and Ductile Cast Irons. *Scripta Metallurgica*, 16:173–177, 1982.

[31] Ashby, M.F. and Jones, D.R.H. *Engineering Materials I: An Introduction to their Properties and Applications*, page 35. 1989. Pergamon Press, Oxford.

[32] Brown, S.B. and Weber, G.A. A Constitutive Model for the Compaction of Metal Powders. *Scripta Metallurgica et Materialia*, 28:11–16, 1993.

[33] Brown, S.B. and Weber, G.A. A Constitutive Model for the Compaction of Metal Powders. *Modern Developments in POwder Metallurgy*, 18-21:465–476, 1988.

[34] Abou-Chedid, G. *Experimental Yield Surface Studies for the Compaction of Metal Powder.* Ph.D. dissertation, M.I.T., 1988.

[35] Shima, S. and Mimura, K. Densification Behavior of Ceramic Powder. *Int. J. Mech. Sci.*, 28(1):53-59, 1986.

[36] Ashby, M.F. *Background Reading: Hot Isostatic Pressing and Sintering.* 1990. Internal Report, Cambridge University Engineering Department, Cambridge.

[37] Schofield, A.N. and Wroth, C.P. *Critical State Soil Mechanics.* 1968. McGraw-Hill, New York.

[38] Hvorslev, M.J. A Ring Shearing Apparatus for Determination of the Shearing Resistance and Plastic Flow of Soils. *Proceedings ICSMFE*, 2:125–129, 1936.

[39] Hvorslev, M.J. and Kaufman, R.I. Torsion Shear Apparatus and Testing Procedures. *Waterways Experiment Station Bulletin No. 38*, 76 pages, 1951.

[40] Marone, C. Laboratory-Derived Friction Laws and THeir Application to Seismic Faulting. *Annu. Rev. Earth Planet. Sci.*, 26:643-696, 1998.

[41] La Gatta, D.P. Residual Strength of Clays and Clay-Shales by Rotation Shear Tests. *Harvard Soil Mechanics Series No. 86.* 1970. Cambridge, Massachusetts.

[42] Bishop, A.W., Green, G.E., Garga, V.K., Andresen, A., and Brown, J.D. A New Ring Shear Apparatus and Its Application tothe Measurement of Residual Strength. *Geotechnique*, 21(4):273–328, 1971.

[43] Anand, L. A Constitutive Model for Friction in Forming. *Annals of CIRP*, 42:361–366, 1993.

[44] Anand, L. A Constitutive Model for Interface Friction. *Computational Mechanics*, 12(4):197–213, 1993.

[45] Roark, R.J. and Young, W.C. *Roark's Formula's for Stress and Strain.* 1989. McGraw-Hill, New York.

[46] Bishop, A.W. Test Requirements for Measuring the Coefficient of Earth Pressure at Rest. *Proceedings of the Brussels Conference on Earth Pressure Problems*, 1:2–14, 1958.

[47] Brown, S.B. An Internal Constitutive Model for the Hot Working of Metals. Ph.D. dissertation, M.I.T., 1987.